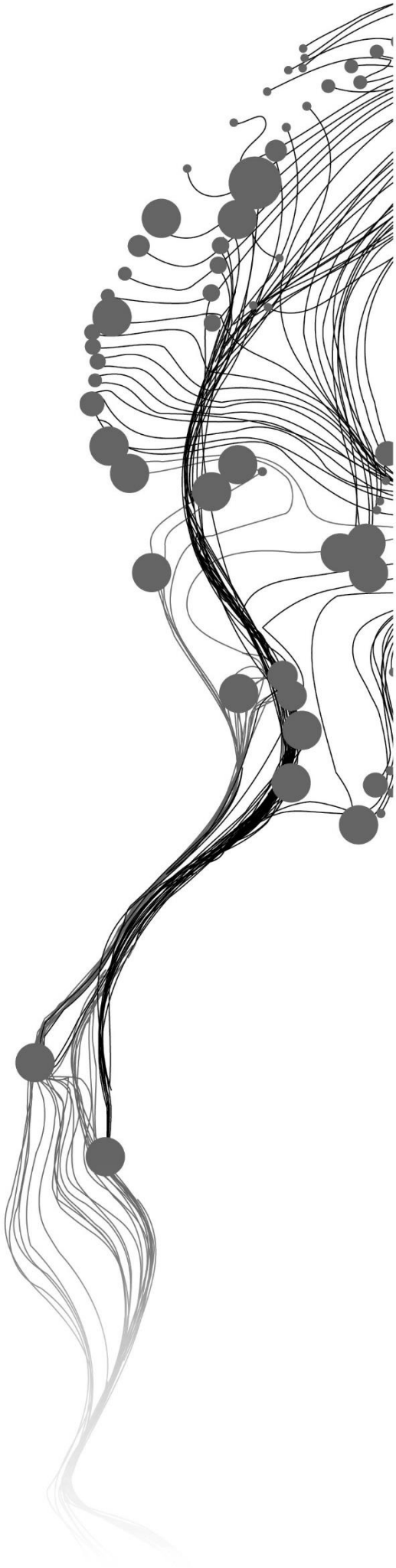

# BAYESIAN APPROACH ON HYPERSPECTRAL UNMIXING OF SANDSTONE ROCK USING HAPKE'S MODEL

MUHAMAD NASIR LUKMAN

Enschede, The Netherlands, June 2024

Thesis submitted to the Faculty of Geo-Information Science and Earth Observation of the University of Twente in partial fulfilment of the requirements for the degree of Master of Science in Geo-information Science and Earth Observation.
Specialization: Applied Remote Sensing for Earth Science

SUPERVISORS:
Dr. F.J.A. Van Ruitenbeek
Dr. J.C. Afonso

THESIS ASSESSMENT BOARD:
Dr. H.M.A. van der Werff (Chair)
Dr. Saeid Asadzadeh (External Examiner, GFZ Postdam)

# ABSTRACT

Spectroscopic measurements have long been utilized to analyse the electromagnetic absorption patterns of minerals, aiding in the identification and quantification of mineral abundance. An important challenge in this field is the occurrence of mixed pixels, where multiple minerals are captured as one pixel. Spectral unmixing techniques aim to resolve this by decomposing the mixed pixel spectra into their individual mineral components.

This research evaluates hyperspectral unmixing techniques for identifying and quantifying mineral compositions in sandstone core samples, focusing on the use of the Hapke Model to address the non-linearity of particulate surface spectra and Bayesian Spectral Unmixing (BSU) to model the uncertainty related to spectral unmixing using the Markov-Chain Monte Carlo (MCMC) method. We also examine the impact of additional spectral processing methods—first derivative, hull removal, and normalization—on the accuracy of spectral unmixing. Furthermore, the BSU method is compared to the Fully Constrained Least-Square (FCLS) method to evaluate its effectiveness.

The study began with experiments using computer-generated mixtures and mineral powder mixtures, followed by spectral unmixing on the core sample. Our results indicate that the simplified Hapke Model significantly enhances the accuracy of spectral unmixing compared to the Linear Mixing Model (LMM). The BSU method provides more detailed information on the variability and uncertainty of mineral abundances, outperforming FCLS in scenarios with complex mineral mixtures. Additionally, spectral processing methods, such as normalization, were shown to reduce spectral variability and improve unmixing results.

In a broader perspective, the findings from this research suggest that the BSU approach, coupled with appropriate mixture model and spectral processing methods, offers a promising opportunity for hyperspectral unmixing in geological applications. This has significant implications for improving and quantifying the accuracy of mineral composition estimates in sandstone cores. Future research should focus on refining uncertainty modelling and optimizing computational efficiency to further enhance the applicability of BSU in real-world scenarios.

# ACKNOWLEDGEMENTS

My mother often tells me that she always prays for me to be surrounded by good and kind people wherever I am in this world. I thank God, the Most Gracious and the Most Merciful, for answering her prayer. My study at ITC has been nothing but a wonderful experience, surrounded by great and kind people. I am deeply thankful for my supervisors, Dr. Frank van Ruitenbeek and Dr. Juan Carlos Afonso, for their time, patience, and guidance throughout my learning process, and for supporting me when I was stuck. I really enjoy and learn so much from our discussion sessions.

I am also grateful to the other professors in ARS for their critical input and encouragement, notably Wim H. Bakker and Dr. Arjan H. Dijkstra, who assisted me in the laboratory, and Bruno Virgilio Portelo, who has been a very helpful procedural advisor.

I am also grateful for all the new friends I made at ITC and thankful for the support, help, and fun memories we shared together. I am fortunate to have had such wonderful classmates. A big shoutout and gratitude to Amy, who has been so kind and helped me immensely throughout the years, and especially in the final days of my thesis, and also to Sachi, Mahasen, Shanan, and Jonbosco, who have been supportive and fun friends throughout the ups and downs of our studies.

I also extend my thanks to the new Indonesian friends I made in the Netherlands, with whom I've shared much laughter: Clava, Andy, Rifqi, Ghaly, Wibi, Salsa, Sry, and Mas Ganda. You guys are acknowledged! And also, a special shoutout for Mas Adhitya for helping me working with Dask.

I thank my family for the support and love that they give me. And of course, I am grateful to the LPDP scholarship, which made my study possible. I did not even dream before of being able to have these very valuable experiences.

Lastly, I sincerely hope that everyone who has helped me in any way has a great and happy life. And in the unlikely event that a new student reads this in the future, I want to give a friendly reminder: while our studies are important, we are so much more than what we write in our thesis. The price for perfection is infinite, so be wise with your priority.

Enschede,

2024

# TABLE OF CONTENT

# LIST OF FIGURES

# LIST OF TABLES

# LIST OF EQUATIONS

# LIST OF ABREVIATIONS

| | |
|---|---|
| CK | : Calcite-Kaolinite sample code |
| QK | : Quartz-Kaolinite sample code |
| CM | : Calcite-Muscovite sample code |
| CKM | : Calcite-Kaolinite-Muscovite sample code |
| CKMQ | : Calcite-Kaolinite-Muscovite-Quartz sample code |
| BSU | : Bayesian Spectral Unmixing |
| FCLS | : Fully Constrained Least-Square |
| H1 | : Hapke Model 1 - Isotropic scattering assumption |
| H2 | : Hapke Model 2 - Anisotropic scattering assumption |
| LMM | : Linear Mixture Model |
| SSA | : Single-Scattering Albedo |
| MCMC | : Markov Chain Monte Carlo |
| MH | : Metropolis-Hastings |
| RMSE | : Root Mean Square Error |
| QEMSCAN | : Quantitative Evaluation of Materials by Scanning Electron Microscopy |
| SEM | : Scanning Electron Microscopy |
| SWIR | : Shortwave Infrared |
| VNIR | : Visible-Near Infrared |
| IFOV | : Immediate Field of View |
| ROI | : Region of Interest |

# 1. INTRODUCTION

## 1.1. Background

Spectroscopic measurements have been used for decades to study the electromagnetic absorption patterns of a mineral and are employed to identify, and to some extent, quantify mineral abundance (Clark et al., 2003). Seminal works by Hunt (1977) and Clark et al. (1990) have been instrumental in identifying the absorption features of minerals in the visible near-infrared (VNIR) and shortwave infrared (SWIR) regions. Building on this foundational work and advancements in hyperspectral sensor technology in recent decades, considerable research has been conducted on the methodologies and applications of hyperspectral imaging for geological studies. Asadzadeh & de Souza Filho (2016) provide a comprehensive review of the various hyperspectral imaging methodologies used in geological remote sensing.

One of the main challenges of hyperspectral imaging for mineral identification and quantification is the unavoidable occurrence of mixed pixels. A mixed pixel is a condition where two or more objects, in this case, minerals, are captured as one pixel by the camera (Keshava & Mustard, 2002).

Hyperspectral unmixing, or more generally *spectral unmixing*, refers to methods that decomposes a mixed pixel spectrum into a set of pure constituent spectra, referred to as *endmembers,* along with their respective fractional *abundances* (Bioucas-Dias et al., 2012). Spectral unmixing therefore belongs to a class of inverse problems commonly referred to as parameter estimation problems (Aster et al., 2013; Keshava & Mustard, 2002). The aim of this type of inverse problem is to identify specific parameters that define a model of the reality based on observed data. To solve the inverse problem, we first need to be able to predict observations as functions of model parameters. This is commonly done via a theoretical or empirical model. The process of computing observations as functions of model parameters is referred to as the *forward* or *direct problem* (Aster et al., 2013). In the context of this work, the forward problem is the analytical model that describes how the spectra of different mineral endmembers mix, commonly referred to as the *mixture model* (Heylen et al., 2014; Keshava & Mustard, 2002).

Mixture models can be categorized as either linear or non-linear. A mixture is considered linear when the incident light interacts with only a single endmember before being reflected to the sensor. In this sense, the mixing process does not occur at the surface because the light reflected from the surface is distinct and separate. Instead, the mixing occurs within the sensor due to the instrument's limitations (Bioucas-Dias et al., 2012). *Linear Mixing Models* (LMM) describe this type of mixture, where the mixed spectra can be modelled by the dot product of the endmember spectra and their respective abundances (Keshava & Mustard, 2002). In other words, the mixed spectrum is a linear combination of the spectra of the endmembers weighted by their respective abundances. This model is valid for flat surfaces with clearly separated endmembers, or often referred to as *checkboard-type* surfaces (Heylen et al., 2014).

However, mineral mixtures have long been documented to have a non-linear behaviour (Nash & Conel, 1974). In this context, the mixing phenomenon happens at the surface due to a physical interaction between the light and multiple endmembers, where the incident light interacts with multiple endmembers before reaching the sensor (Bioucas-Dias et al., 2012; Mustard & Pieters, 1989). This mixing process is typical for particulate surfaces, where the endmembers are randomly distributed in close proximity to each other, also referred to as *intimate mixtures* (Heylen et al., 2014). A popular approach to model this complex

interactions between light and particulate surface is through the elaborate and semi-empirical model developed by Hapke (1981), known as the *Hapke Model* (see Section 3.1.2).

Some additional spectral processing methods such as *hull-removal*, *first derivative*, and *normalization* of the spectra also widely used as a processing step before spectral unmixing (Ducasse et al., 2020; J. Zhang et al., 2005; Zhao & Zhao, 2019). Additional processing steps are shown to reduce the spectral variability and the non-linearity effect and can enhance shallow features of the spectra (Ducasse et al., 2020; Rinnan et al., 2009).

Given a model (or function) that describes the mixing process, spectral unmixing involves the inverse process of the model. This is typically achieved by solving a constrained optimization problem to minimize the residual between the observed mixed spectrum and the modelled spectrum (Bioucas-Dias et al., 2012). This type of optimization approach applied to spectral unmixing results in a single best fitting estimate. *Fully Constrained Least-Square* spectral unmixing, or just FLCS for short, is one example of such methods (Heinz et al., 2003).

Another approach to spectral unmixing is the Bayesian approach, (Dobigeon et al., 2008; Figliuzzi et al., 2016; Lapotre et al., 2017). Unlike the optimization method that focus on obtaining a single best-fitting estimate, the Bayesian approach aims to describes the complete state of knowledge about the problem which includes the uncertainty of the prediction. Bayesian (or probabilistic formulations) are based on the idea of recasting the inverse problem in the form of a statistical inference problem (see e.g. Aster et al. (2012); Gregory (2005)). The interest therefore changes from answering questions like "what is the abundance of endmember X?" to "what do we know about endmember X?". Such a state of knowledge is best represented by probability distributions which provide comprehensive information about the variability and uncertainty of the estimates. This detailed information helps identify potential biases and areas where the model may be problematic, guiding improvements for future predictions. In this report, this Bayesian approach on spectral unmixing will be referred *as Bayesian Spectral Unmixing* (BSU) and it will employ *Markov-Chain Monte Carlo* (MCMC) methods to approximate the full probability distribution of the mineral abundances. (see Section 3.5)

## 1.2. Problem Statement

Most studies that explore the Hapke Model for mineral mixtures have been conducted in the context of studying extraterrestrial surfaces, which mostly consist of mafic minerals (Harris & M. Grindrod, 2018; Lapotre et al., 2017; Mustard & Pieters, 1989). The application of this model to mixtures of quartz, clay, mica, and carbonate minerals has not yet been reported, despite their common occurrence in natural sandstones. Among other factors, mineral composition can significantly influence the porosity of sandstones. For example, clay and carbonate content in sandstones commonly act as a matrix and cement, respectively, which reduce porosity (Al-Kharra'a et al., 2023; Cui et al., 2017). A good estimate of the mineralogy of sandstones may be a useful way to estimate its porosity.

Some studies have explored elaborate formulation of Hapke Model using Bayesian approach to estimate mineral abundances and other physical quantities of the surface (Howari et al., 2018; Lapotre et al., 2017; Pilorget & Fernando, 2021). However, no studies have been reported the application of Bayesian Spectral Unmixing in core scanning application. This research aims to test the Bayesian approach to spectral unmixing in the context of hyperspectral core scanning, albeit with a simpler assumption for the Hapke Model.

In this research, different simplified assumptions of the Hapke Model will be tested and compared to the assumption of the LMM in the context of quartz-clay-mica-carbonate mixtures. The Bayesian approach to unmixing will be tested and compared with FCLS to evaluate the added value of this approach. The influence of additional spectral processing steps before unmixing (hull-removal, first derivative, and normalization) will also be evaluated. Finally, the application of this method will be tested for spectral unmixing of a core sample of sandstone to quantify its mineral composition.

## 1.3. Research Objectives and Research Questions

The primary objective of this research is to develop and evaluate a hyperspectral unmixing strategy for hyperspectral images of sandstone core samples, along with an assessment of the associated uncertainties. This main objective is further divided into 3 sub-objectives, each with its corresponding research questions (RQ):

1. Create computer-generated mixtures of calcite, quartz, muscovite, and kaolinite and test the performance of BSU proposed in this research under a simple and ideal case.
    a. How effective is the BSU approach used in this study at modelling the uncertainty of the unmixing process for the computer-generated mixture under different noise variance? (RQ 1.a)
    b. How does the performance of BSU compare to FCLS spectral unmixing in term of prediction errors? (RQ 1.b)

2. Create powder mixtures of calcite, quartz, muscovite, and kaolinite and test the mixture model and the performance of BSU under a more complex, real physical mineral mixture.
    a. Which mixture model proposed in this study can best reconstruct the observed mineral mixture spectra? (RQ 2.a)
    b. How effective is BSU approach used in this study at modelling the uncertainty of the unmixing process of the powder mixtures? (RQ 2.b)
    c. How does the performance of BSU compare to FCLS spectral unmixing in term of prediction errors? (RQ 2.c)
    d. How do different spectral processing steps (hull removal, first derivative, and normalization) affect the unmixing results? (RQ 2.d)

3. Apply BSU to unmix hyperspectral image of sandstone core sample.
    a. How well can insights from the previous steps be generalized into the real rock sample? (RQ 3.a)
    b. What are the strengths and limitations of the BSU approach relative to the FCLS method in terms of accuracy, computational efficiency, and uncertainty modelling? (RQ 3.b)

## 1.4. Thesis Structure

After the general introduction in this first chapter, the second chapter will describe the sample preparation and data acquisition for the computer-generated samples, powder mixture samples, and core sample. The third chapter will discuss the methods used in this research, starting with an elaborate description of the mixture models and spectral unmixing approaches used, followed by a description and justification of each stage of the research. The fourth and fifth chapters will elaborate on the results and discussion of the research, respectively. In the sixth chapter, the limitations, reflections, and outlook of this research will be briefly discussed. Finally, this report will be concluded in the seventh chapter with the conclusions.

# 2. SAMPLE PREPARATION AND DATA ACQUISITION

Three sets of samples were prepared for this study. The first set was a computer-generated mixture of endmembers spectra from the USGS spectral library. The second set was a mixture of pure mineral powders. The third sample set was a real rock sample from a drill core.

## 2.1. Computer-Generated Mixture

Pure endmember spectra of calcite, kaolinite, muscovite, and quartz from the USGS Spectral Library (Kokaly et al., 2017) were collected to create artificial mixtures. Figure 1 presents the selected endmember spectra in the range of $350\ nm$ to $2500\ nm$.

Calcite spectrum is characterized by $CO_3$ absorption feature, with the most diagnostic one in $2340\ nm$. Kaolinite's most distinctive features are its duplet around $\sim 1400\ nm$ and $\sim 2200\ nm$. Muscovite diagnostic features are related to the Al-OH bonds with the most prominent feature around ~2200 nm (Pontual et al., 2008). Quartz is not spectrally active in this wavelength range (Laukamp et al., 2021) hence it does not show any absorption feature in its spectra.

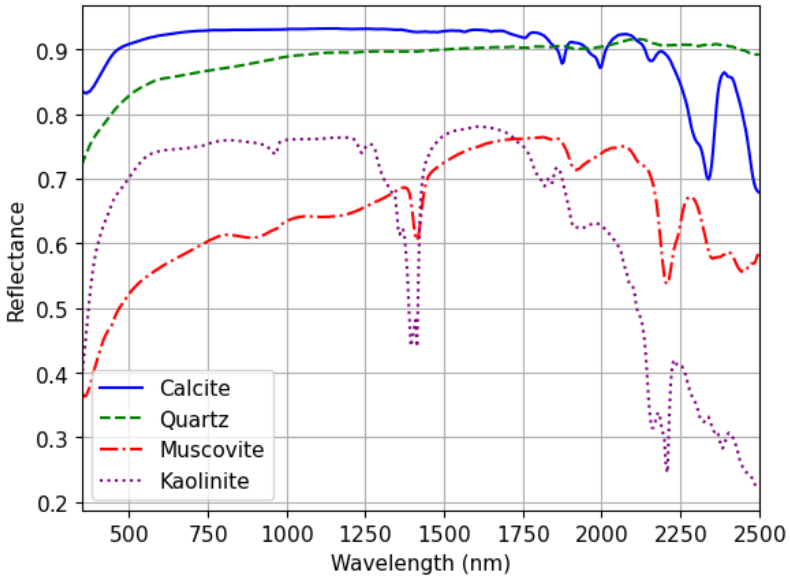


**Figure 1.** Selected endmember spectra from USGS Spectral Library

Artificial binary, ternary, and quaternary mixtures were randomly generated from the selected pure spectra following LMM with added gaussian noise (mean of $0$ and variance from $0$ up to $2.5 \times 10^{-3}$), while respecting the non-negativity and sum-to-one constraint. The abundance values of each randomly generated spectrum were also stored for the accuracy assessment of the unmixing test.

## 2.2. Powder Mixture

### 2.2.1. Powder Mixture Preparation

Four types of laboratory grade pure mineral powders—calcite, kaolinite, muscovite, and quartz—were used to create the mineral mixtures. These minerals were chosen because they resemble the mineral

composition of the diagenetic quartz sandstone sample chosen for the natural rock study. The exact crystal size information of calcite and kaolinite powder is not available, but it was in a very fine powder. Quartz and Muscovite were in bigger crystal size in the range of $0.5 - 0.8\ mm$, these two minerals were further processed to reduce it crystal size into a fine powder.

Muscovite and quartz mineral powder was crushed into finer particles using a ball mill for $10$ minutes at $250\ rpm$ and then sieved for an additional $10$ minutes with $100$ amplitudes vibrations to separate the mineral by its particle sizes. Particles smaller than $68\ \mu m$ were collected to generate mixtures specified in Table 1.

**Table 1.** Volume fraction of powder mixture samples.

| Volume Fractions | | | | |
|---|---|---|---|---|
| Sample | Calcite | Kaolinite | Muscovite | Quartz |
| CK1 | 0.10 | 0.90 | 0 | 0 |
| CK2 | 0.30 | 0.70 | 0 | 0 |
| CK3 | 0.69 | 0.31 | 0 | 0 |
| CK4 | 0.89 | 0.11 | 0 | 0 |
| QK1 | 0 | 0.10 | 0 | 0.90 |
| QK2 | 0 | 0.30 | 0 | 0.70 |
| QK3 | 0 | 0.70 | 0 | 0.30 |
| QK4 | 0 | 0.90 | 0 | 0.10 |
| CM1 | 0.11 | 0 | 0.89 | 0 |
| CM2 | 0.31 | 0 | 0.69 | 0 |
| CM3 | 0.71 | 0 | 0.29 | 0 |
| CM4 | 0.90 | 0 | 0.10 | 0 |
| CKM1 | 0.35 | 0.36 | 0.29 | 0 |
| CKM2 | 0.11 | 0.46 | 0.42 | 0 |
| CKM3 | 0.44 | 0.45 | 0.11 | 0 |
| CKM4 | 0.45 | 0.12 | 0.43 | 0 |
| CKMQ1 | 0.25 | 0.26 | 0.24 | 0.26 |
| CKMQ2 | 0.30 | 0.31 | 0.28 | 0.11 |
| CKMQ3 | 0.10 | 0.11 | 0.09 | 0.70 |
| CKMQ4 | 0.20 | 0.20 | 0.19 | 0.40 |

Twenty different mixtures were prepared, each with specific volume proportions to simulate various natural combinations of minerals. The proportions of the minerals were varied from small to large. Each sample was coded by the combination of the first letter of each mineral present in the mixture, followed by an arbitrary number for differentiation. Density data from Mindat (2024) were used to calculate these proportions. The densities used were $2.71\ g/cm^3$ for calcite, $2.68\ g/cm^3$ for kaolinite, $2.83\ g/cm^3$ for muscovite, and $2.65\ g/cm^3$ for quartz. Mineral fractions for each mixture specified in Table 1 were put inside a centrifuge tube with five $2\ mm$ glass beads and shaken for $5$ minutes to get a homogenous mixture of the powders. The addition of glass beads was intended to improve the consistency of the mixture by reducing the clumping of the minerals and the proportions of minerals sticking at the centrifuge tube. Each mixture, weighing $0.8\ g$, was then evenly spread onto a flat glass surface and gently pressed to achieve a thickness of approximately $1.5\ mm$. The resulting powder mixtures from which the spectral measurements were acquired are presented in Figure 2.

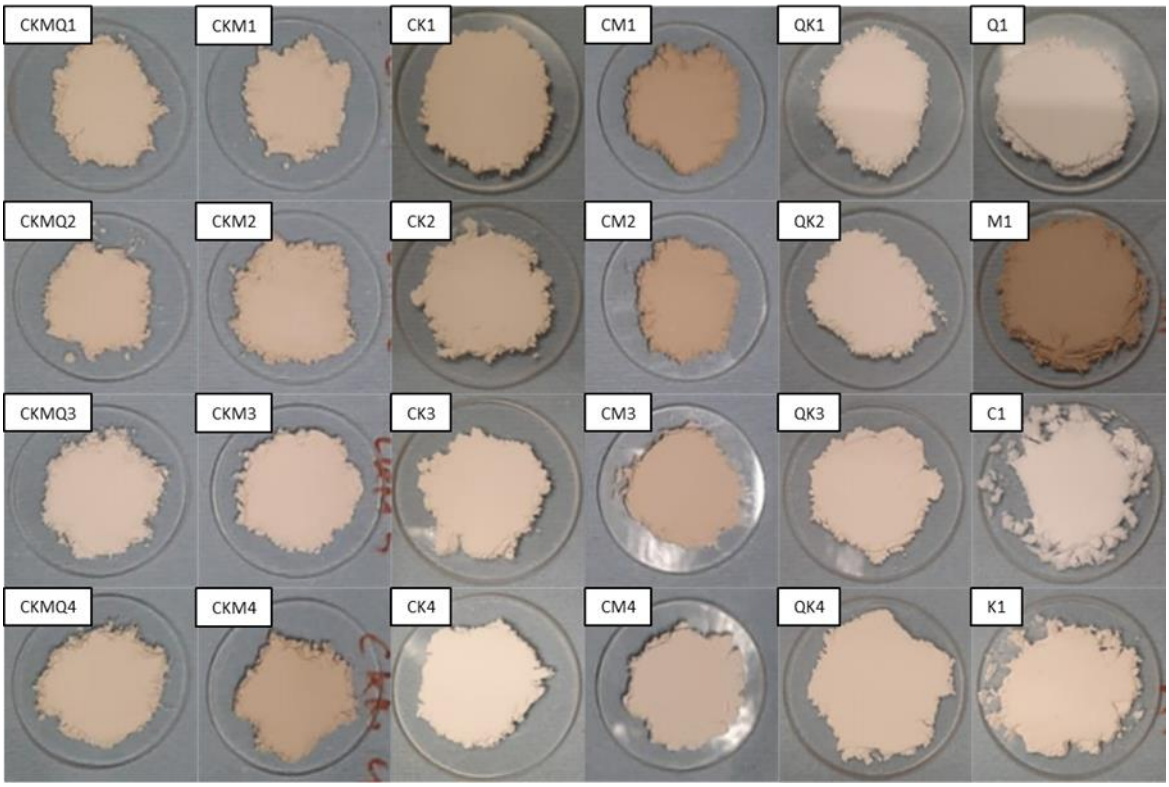


**Figure 2.** Results of powder mixture samples preparation.

### 2.2.2. Powder Mixture Data Acquisition and Preprocessing

The reflectance spectra of the powder mixtures were measured using an ASD Fieldspec 3 instrument equipped with bare optics. The instrument covers the VNIR range from $350\ nm$ to the SWIR range at $2500\ nm$ with $3$ to $10\ nm$ spectral resolutions. The laboratory setup of the ASD is illustrated in Figure 3.

The critical aspect of the setup is the angle between the incoming light from the light source and the outgoing light reflected from the sample into the ASD sensor. Following the assumption discussed later in Section 3.1.2, this angle, referred to as the phase angle, must exceed $15°$. In this setup, the illumination angle $(i)$ was set as $45°$ from the zenith, and the angle between the sample and the sensor $(e)$ was set as $0°$ from the zenith.

There are some technicalities related to data acquisition that are important to mention here for the replicability of the research. First, the light source and the ASD instrument stabilized for 30 minutes before measurements were taken to ensure consistent performance.

Second, each measurement with the ASD instrument involved capturing ten repeated measurements, from which the mean value was automatically calculated. Furthermore, measurements were taken from ten different spots on the surface of each sample to account for potential variability. The mean of these ten measurements was used for subsequent analysis.

Third, a white reference measurement was performed before each sample measurement to convert radiance measurements into reflectance values. Additionally, splice correction was applied to align data accurately across the three main detectors of the ASD instrument, correcting for any displacement that might occur. Spectral subsetting was then applied, where spectra above $2450\ nm$ were discarded due to high noise level. Given that the main absorption features of the minerals are above $2000\ nm$, we focused on the spectral range of $2000 - 2450\ nm$ for further analysis.

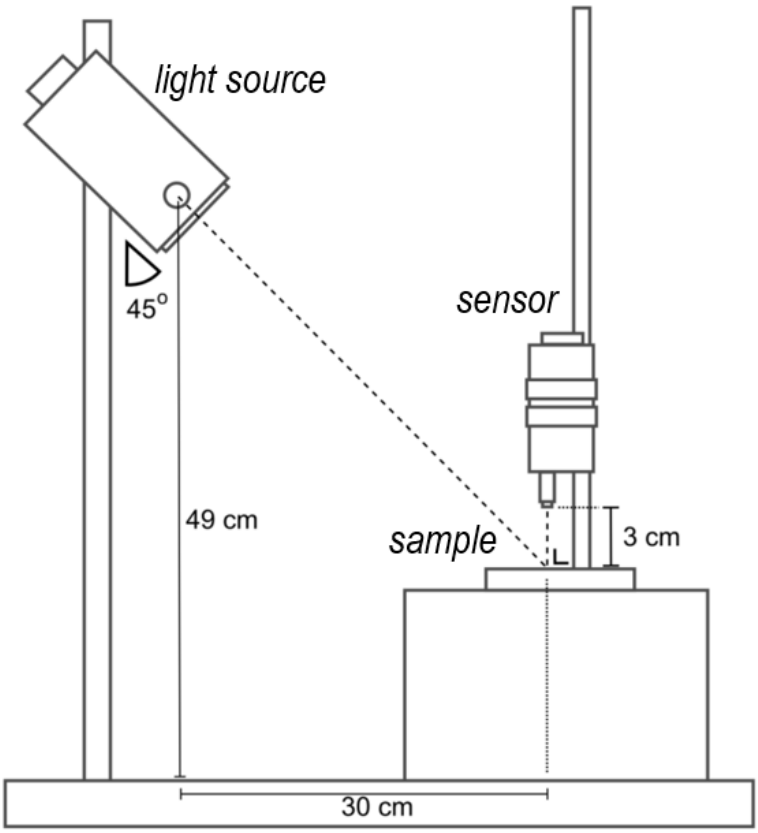


**Figure 3.** ASD Fieldspec setup for spectral measurements.

## 2.3. Core Sample

### 2.3.1. Core Sample Preparation

A rock sample from offshore drill hole cores in the Southern North Sea Basin was chosen for this investigation. The core interval intersects the upper and lower Slochteren Formation and was identified as quartz arenite with significant illite-muscovite and carbonate mineral content (W. Liu et al., 2023).

QEMSCAN analysis results of these rocks were reported in confidential reports by SGS Canada Inc. and provided by Wintershall Noordzee B.V. QEMSCAN is an acronym for Quantitative Evaluation of Materials by Scanning Electron Microscopy. This system utilizes a scanning electron microscope (SEM) to image the sample with a $10\ \mu m$ pixel size and assign a mineral name to every pixel using both back scattered electron signal intensity as well as an Energy Dispersive Spectra signal (EDS) at each measurement point (SGS, 2013).

However, this study did not utilize the image data directly; instead, it employed the derived bulk mineralogy of the whole rock, represented as area percentages. This data was later used to evaluate the result of hyperspectral unmixing conducted in this study.

The rock samples used in this study are cut core samples (Figure 4), with hyperspectral image acquisition carried out on the same side used for the QEMSCAN analysis.

**Figure 4.** Quartz arenite sandstone core sample used for this study.

#### 2.3.2. Core Sample Data Acquisition and Preprocessing

The hyperspectral image of the core was captured by the SWIR Specim Hyperspectral Camera, mounted on lab-stage in the ITC Spectroscopy Laboratory. The image covers a wavelength range from $1000\ nm$ to $2000\ nm$, with a spectral resolution of $12\ nm$ and a pixel size of $256\ nm$. Only one illumination source was used during image acquisition, positioned at a $45°$ angle from the zenith. The angle between the sample and the camera was maintained at $0°$.

After image acquisition, white and dark reference correction was performed using *Hyppy* software (Bakker, 2024). The upper $50\%$ of the brightest pixels were utilized for white reference. Afterwards, spectral subsetting was applied to the data. Using the same logic as with the powder mixtures, we select the wavelength range of $2000 - 2450\ nm$. Then, Spectral smoothing was executed using the *Hyppy* "Fast Mean $1 + 5 + 1$ neighbourhood" filter to reduce the noise. Finally, the image's background was masked in ENVI by manual delineation of the Region of Interest (ROI).

The full QEMSCAN results of the core sample are shown in Table 2. For simplicity, we focused on the abundance values of quartz (which may include opal, cristobalite, and chert), muscovite+illite+illite-smectite+Fe-illite, and calcite+dolomite+Fe-dolomite+siderite+Fe oxides. These three mineral groups will be referred to as the quartz group, muscovite-illite group, and carbonate group, respectively.

As explained in Section 2.1, here we also expect the quartz spectra to be generally featureless. For carbonate minerals, we expect the main absorption feature of $CO_3$ to be the main distinctive absorption feature of the mineral group. There are small variances in the wavelength of the main $CO_3$ absorption feature in different carbonate mineral species. For instance, it is typically found at $2340 - 2345\ nm$ for calcite, $2320 - 2350\ nm$ for siderite, and $2328 - 2340\ nm$ for dolomite (Pontual et al., 2008). Due to the subtle differences, grouping these minerals together is preferred. For muscovite and illite, both minerals have very similar spectra with the main absorption feature related to Al-OH bond in $2180 - 2228\ nm$. The primary difference is the occurrence of water absorption feature in illite at $1912\ nm$. Since the selected wavelength range was in $2000 - 2450\ nm$, illite and muscovite is practically indistinguishable. Although it is possible to extend the wavelength range to start from $1900\ nm$ to distinguish illite from muscovite, we chose to start at $2000\ nm$ because the water absorption feature in natural surfaces, like rock samples, often shows high variability, potentially obscuring the unmixing results.

Together, these three mineral groups comprise 99.593% of the areal composition of the core sample. For ground truth comparison used in this study, the normalized values of the mineral groups were used, which are 69.086% for the quartz group, 14.140% for the muscovite-illite group, and 16.772% for the carbonate group.

**Table 2.** QEMSCAN results for core sample used in this study. Mineral that is blocked with the same colour is grouped together for simplification.

| Mineral Name | Area Percentage | Mineral Name | Area Percentage |
|---|---|---|---|
| *Quartz* | 68.805% | *Pyrite* | 0.001% |
| *K Feldspar* | 0.091% | *Barite* | 0.013% |
| *Plagioclase* | 0.028% | *Anhydrite* | 0.000% |
| *Chlorite* | 0.127% | *Halite* | 0.000% |
| *Muscovite* | 3.974% | *Rutile & Ti Silicates* | 0.071% |
| *Illite & Illite-smectite* | 9.999% | *Ilmenite* | 0.003% |
| *Fe-Illite & Illite-smectite* | 0.110% | *Apatite* | 0.022% |
| *Calcite* | 1.079% | *Tourmaline* | 0.004% |
| *Dolomite* | 11.784% | *Zircon* | 0.003% |
| *Fe-Dolomite* | 2.289% | *Biotite* | 0.023% |
| *Siderite & Fe Oxides* | 1.553% | *Kaolinite* | 0.019% |

# 3. METHODOLOGY

As mentioned in the previous section, three sample sets were prepared for this study. The first set was a computer-generated mixtures of endmember spectra to test the general performance of BSU and FCLS in a relatively simple setup. The second set was a mixture of pure mineral powders, precisely measured to mimic ideal conditions, which were then used to test the mixing model and the performance of the unmixing algorithm for real mixtures. The last sample set consisted of actual rock sample from the drill hole core, allowing for testing of the mixing model and the unmixing performance with more practical significance.

This chapter begins with a description of the different mixing models and unmixing approaches relevant for this study. At the end of the chapter, the different stages of the study will be elaborated, including detailed descriptions of the approaches and goals in every stage.

In the following sections, all mathematical statements will be presented in italic font. Lower-case notation $(i, o, \dots)$ denotes scalars, bold lower-case notation $(\boldsymbol{r},\ \boldsymbol{w}, \dots)$ represent vectors, and a bold upper-case notation represents matrices $(\boldsymbol{E}, \boldsymbol{X}, \dots)$. Subscripts $(\boldsymbol{E_r}, \boldsymbol{E_w}, \dots)$ will be utilized to specify different forms or stages of the variable as necessary; their meaning will be evident from the context. For the Hapke Model formulation, the notation will closely mirror the original formulation introduced by Hapke (1981). In Bayesian formulations, probability distributions will be denoted by upper-case cursive Latin letters, followed by their parameters in parentheses ($\mathcal{D}(\cdot), \mathcal{N}(\cdot), \dots$), and parameters that are related to a specific distribution will be denoted by Greek letters ($\mu, \sigma, \dots$).

## 3.1. Mixture Model

Mixture models are used in spectral unmixing to describe how the spectral signals of individual endmembers mixed to create the observed spectral signal (Keshava & Mustard, 2002). Essentially, these models explain how the light reflected from various endmember mixes, based on the proportions of each endmember present in the surface. Three different mixture models are considered in this study. The first model is the linear mixture model or LMM which assumes that the light rays interact only with a single endmember before being scattered into the sensors (Keshava & Mustard, 2002). The remaining two models (hereafter denoted as H1 and H2) are non-linear and include complex interactions between light and multiple endmembers at the surface before the light is scattered into the sensors, as described by the Hapke Model (Hapke, 1981). Model H1 assumes isotropic scattering, whereas model H2 allows for anisotropic scattering. Details on all these models will be elaborated in the next sections.

### 3.1.1. Linear Mixture Model (LMM)

Since electromagnetic radiation follows the superposition principle (Freegarde, 2012), the LMM describes the reflectance spectra of a mixture $\boldsymbol{y_r}$ as a linear combination of the reflectance spectra of pure endmembers $\boldsymbol{E_r}$ weighted by their fractional abundance $\boldsymbol{a}$, alongside small addition errors $\boldsymbol{n}$.

$$\boldsymbol{y_r} = \boldsymbol{E_r a} + \boldsymbol{n} \tag{1}$$

Where $\boldsymbol{y_r}$ and $\boldsymbol{n}$ are vectors of dimension $j$ (number of spectral bands), $\boldsymbol{E_r}$ is a 2-dimensional matrix of size $j$ by $k$ (number of endmembers), and $\boldsymbol{a}$ is a vector of dimension $k$. This model is strictly applicable for *areal mixtures* (also referred to as *macroscopic* and/or *checkboard mixtures*) where the surface area captured by a detector's immediate field of view (IFOV) consists of several distinctly separated patches, each composed of a pure endmember (Hapke, 2012). A fundamental assumption underlying LMM is that

incident light rays only interact with a single endmember on the surface before being reflected and captured by the sensor (Bioucas-Dias et al., 2012).

### 3.1.2. Hapke Model

Geological surfaces often exhibit complexity beyond the assumptions of LMM. Rocks' surfaces often comprise an intimate mixture of mineral where the mineral particles are randomly distributed in close contact with each other (Heylen et al., 2014). In this case, a multiple scattering effect occurs where a single light ray interacts with multiple endmembers before being reflected to the sensor (Mustard & Pieters, 1989). During each interaction, the light might be absorbed and scattered multiple times, breaking the reflectance's linearity assumption.

There are several ways to deal with this non-linearity. One possibility is to derive another physical measure that describes the relationship between light and individual particles on surfaces. *Single-Scattering Albedo* (SSA) is defined as the ratio of energy scattered by a particle to the total extinction (scattering + absorption) of energy by the particle (Hapke, 1981). This definition implies that SSA primarily depends on the properties of the first particle the light encounters. SSA effectively isolate the influence of scattering by individual particles because it models the scattering and absorption processes at a single-particle level. Therefore, the mixed SSA spectra can be approximated linearly as the combination of the pure SSA spectra of its endmembers and its corresponding fractional areal abundance.(Heylen et al., 2014)

Based on this definition, we can substitute the reflectance term in observed and endmember data in Eq. (1) by its corresponding SSA and linearized the intimate mixture problem with:

$$\boldsymbol{y_w} = \boldsymbol{E_w a} + \boldsymbol{n} \tag{2}$$

Where $\boldsymbol{y_w}$ and $\boldsymbol{E_w}$ are the mixture spectra vector and endmember matrix in the SSA domain, respectively. Note that here, $\boldsymbol{a}$ refers to the mean cross-sectional area of the endmembers. Assuming a similar grain size distribution for the endmembers, $\boldsymbol{a}$ becomes equal to the volumetric fractions of the endmembers (Heylen et al., 2014).

To derive SSA from reflectance data is not trivial, as the interaction between light and particles in a complex mixture requires information about the viewing geometry of the light source and the detector relative to the zenith and other variables related to the surface's physical and scattering behaviour (Hapke, 1981).

Building upon radiative transfer theory, Hapke (1981) derived a semi-empirical model of *bidirectional reflectance*. Bidirectional reflectance is defined as the ratio of the amount of radiation reflected in a specific direction to the amount of radiation incident from a particular direction (Heylen et al., 2014). The Hapke model links bidirectional reflectance ($\boldsymbol{r}$) and SSA ($\boldsymbol{w}$) according to:

$$\boldsymbol{r}(\mu_0, \mu, g) = \frac{\boldsymbol{w}}{4\pi} \frac{\mu_0}{\mu_0 + \mu} \{[1 + B(g)]P(g) + H(\boldsymbol{w}, \mu_0)H(\boldsymbol{w}, \mu) - 1\} \tag{3}$$

Where $\mu_0$ is the cosine of incoming radiation ($i$), $\mu$ is the cosine of outgoing radiation ($e$) and $g$ is the phase angle between $i$ and $e$ (Figure 5). These three variables are related to viewing geometry of the data acquisition relative to the zenith. $B(g), P(g)$ and $H(\cdot)$ are a *backscattering function*, a *particle phase function*, and the *Chandrasekhar function*, respectively. In this equation, the behaviour of the single particle scattering is defined by $P(g)$, and the behaviour of the multiple scattering is approximated by $H(\cdot)$.

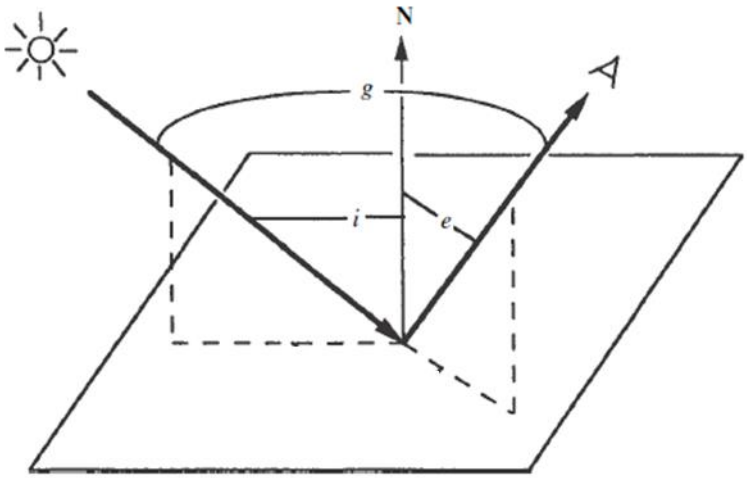


**Figure 5.** Schematic diagram of bidirectional reflectance with incoming radiation angle $(i)$, outgoing radiation angle $(e)$, and phase angle $(g)$. Modified from Hapke (2012).

The backscattering function, which describes the so-called opposition surge effect, is observed to peak at a low phase angle and decays exponentially to near zero when $g = 90°$ (Mustard & Pieters, 1989). According to previous studies, this effect is negligible for $g > 15°$-$20°$ (Hapke, 1981; Mustard & Pieters, 1989). In this study, the phase angle is set to $45°$, making it safe to assume:

$$B(g) = 0 \tag{4}$$

In the context of hyperspectral imaging, we are interested in the *relative bidirectional reflectance* **(Γ)** which defined as the ratio of $\boldsymbol{r}$ of the surface of interest relative to the $\boldsymbol{r}$ of perfectly reflective panel**.** Using assumption in Eq. (4) and definition of $\boldsymbol{r}$ in Eq. (3), this relationship can be expressed as:

$$\boldsymbol{\Gamma}(\mu_0, \mu, g) = \boldsymbol{w}\ \frac{P(g) + H(\boldsymbol{w}, \mu_0)H(\boldsymbol{w}, \mu) - 1}{H(1, \mu_0)H(1, \mu)} \tag{5}$$

This formulation depends only on the Chandrasekhar's and phase functions. Hapke (1981, 2012) discussed in detail various approximations of these functions for solving relative bidirectional reflectance in different scenarios.

The phase function approximation can be expressed by the *two-term Legendre polynomial* described by Hapke (1981):

$$P(g) = 1 + b\ cos(g) + c\ (1.5\ cos^2(g) - 0.5) \tag{6}$$

This approximation is also used in other studies, mostly in applications to lunar and Martian surfaces (e.g. Harris & Grindrod, 2018; Howari et al., 2018; D. Liu et al., 2015; Lucey, 1998; Mustard & Pieters, 1989; Sklute et al., 2015). In this approximation, $b$ and $c$ are wavelength-dependent constants describing the surface's scattering behaviour. When the scattering behaviour is isotropic (i.e. same in all directions), $b = c = 0$, and $P(g) = 1$.

The Chandrasekhar's function describes the multiple scattering behaviour of particles and involves an integral that is not solvable analytically. Hapke (1981) provides an analytical approximation with up to $4\%$ error:

$$H(\boldsymbol{w}, x) = \frac{1 + 2x}{1 + 2x\sqrt{1 - \boldsymbol{w}}} \tag{7}$$

Where $x$ represent either $\mu_0$ or $\mu$. This approximation was further tested by Mustard & Pieters (1989) and reported up to $6\%$ errors in very high albedo materials. Hapke (2012) later provided a more accurate approximation with less than $1\%$ error for all values:

$$H(\boldsymbol{w}, x) = \left\{1 - wx\left[r_0 + \left(\frac{1 - 2r_0 x}{2}\right)\log\left(\frac{1 + x}{x}\right)\right]\right\}^{-1} \tag{8}$$

Where $r_0 = (1 - \gamma)/(1 + \gamma)$ and $\gamma = (1 - w)^{1/2}$.

This study explored two different assumptions of the Hapke Model, denoted as H1 and H2, to evaluate their practicality and accuracy in describing the data. The detailed assumptions of each model are described in the following sections.

#### 3.1.2.1. H1: Isotropic Scattering

This model assumes isotopic scattering behaviour of the surface therefore $P(g) = 1$. For the Chandrasekhar's function, despite its lower accuracy compared to Eq. (8), the use of Eq. (7) is preferred here since it allows to obtain analytical solutions of Eq. (5), which can be written as:

$$\boldsymbol{w} = 1 - \left(\frac{\sqrt{(\mu_0 + \mu)^2\boldsymbol{\Gamma}^2 + (1 + 4\mu\mu_0\boldsymbol{\Gamma})(1 - \boldsymbol{\Gamma})} - (\mu_0 + \mu)\boldsymbol{\Gamma}}{(1 + 4\mu\mu_0\boldsymbol{\Gamma})}\right)^2 \tag{9}$$

This is the only analytical solution for SSA within the framework of Hapke's Model. Therefore, it is widely used in many spectral unmixing applications (Ducasse et al., 2020; Heylen et al., 2014).

#### 3.1.2.2. H2: Anisotropic Scattering with Fixed Constant Derived from Previous Study

Mustard & Pieters (1989) derived an empirical value for $b$ and $c$ for olivine, magnetite, and hematite samples using Hapke's Model with the phase function approximated by two-term Legendre polynomial in Eq. (6). The mean of the constants, which are $b = -0.4$ and $c = 0.25$, have been used in subsequent studies for similar minerals (Lucey, 1998) and to estimate mineral abundances of extraterrestrial surfaces with similar mineralogy (Harris & M. Grindrod, 2018; D. Liu et al., 2015). These constants also produced useful results for spectral unmixing of salts (Howari et al., 2018), and gypsums & clay samples (Robertson et al., 2016), which can be regards as a completely different group of minerals compared to the one used by Mustard & Pieters (1989).

In H2 Model, Eq. (5) was solved using the phase function specified in Eq. (6) with fixed constants $b = -0.4$ and $c = 0.25$. Additionally, a more accurate approximation of Chandrasekhar's function, as described in Eq. (8), was utilized. Since this model does not have analytical solutions for $\boldsymbol{w}$, a least square optimization approach was used to derive $\boldsymbol{w}$ from Eq. (5).

### 3.2. Spectral Processing Methods

Three different addition spectral processing methods are considered in the study which are hull removal, first derivative, and normalization. Spectra processing methods are usually employed to reduce variability

of the spectra (Rinnan et al., 2009), and in some cases shows improvement in unmixing results (Ducasse et al., 2020; Zhao & Zhao, 2019).

Hull removal involves in fitting and removing convex hull to the spectral data which aims to correct the continuum effects and highlight absorption features (Van Der Meer, 2000). The removal is done by division as suggested by Clark & Roush (1984).

First derivative processing calculated the derivative of the spectral data. By focusing on the rate of change in reflectance, this method can effectively separate closely spaced spectral features and remove the baseline effect of the spectra (Rinnan et al., 2009).

Normalization is a process used to adjust the values in a dataset to a common scale. In this research, the normalization method used is based on the Euclidean norm. This process involves scaling each spectral vector into a unit vector of length one. This scaling preserves the shape of the spectral vector by maintaining the relative proportions of the vector components, affecting only the magnitude (Rinnan et al., 2009).

### 3.3. Endmember Extraction

For actual rock samples, pure endmember spectra are typically not available. In this research, the pure endmember spectra were approximated using the *N-FINDR* algorithm introduced by Winter (1999). The implementation of this algorithm requires the number of endmembers to be known *a priori*. In the core sample used in the research, the actual number of endmembers is known based on QEMSCAN results.

The N-FINDR algorithm assumes that the pure endmember pixel exists in the image. In the case when it does not exist, the acquired spectra will be the least contaminated pure endmember spectra; as such, this algorithm will not work well in a homogeneously mixed surface.

N-FINDR works by exploiting the geometric nature of hyperspectral data (Winter & E., 1999). The algorithm first reduces the dimensionality of the data to be one less than the number of endmembers through orthogonal subspace projection such as *Principal Component Analysis* (PCA) or *Maximum Noise Fraction* (MNF). In this projected space, every pixel can be represented as a single data point. Assuming that every pixel is a mixture of the endmembers, the vertex of a convex geometry that encloses all the points can be classified as pure pixels (Figure 6).

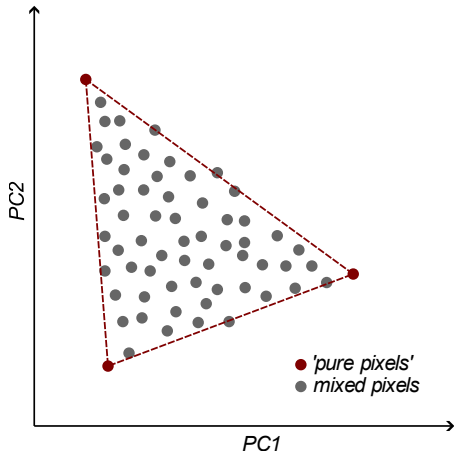


**Figure 6.** Schematic illustration showing how the purest spectra forms the vertex of convex geometry that encloses all other pixels in projected subspace.

This convex geometry is, by definition, a set of data points with the largest volume. The N-FINDR algorithm tries to find these data points by iteratively calculating the volume of a random set of samples. The implementation of the N-FINDR algorithm that was used in this study is the one under the *Python* library called *PySptools* (Therein, 2018). Since this algorithm is sensitive to brightness differences, the spectra are normalized first before applying the algorithm.

### 3.4. Fully Constrained Least-Square (FCLS) Spectral Unmixing

Assuming known endmembers spectra, the abundance value in Eq. (1) and Eq. (2) can be solved using an optimization method by minimizing the square error while enforcing the non-negativity and sum-to-one constraints:

$$\min_{\boldsymbol{a}} ||\boldsymbol{y} - \boldsymbol{E}\boldsymbol{a}||_2^2 \quad subject\ to: \ (\ a_i \geq 0\ )\ and\ (\sum_{i=1}^{n} a_i = 1) \tag{10}$$

This problem is known as FCLS spectral unmixing (Heinz et al., 2003), which is arguably the most popular spectral unmixing approach. The result of the FCLS algorithm is a single value estimate of endmember abundances, which minimizes the squared residual as shown in Eq. (10). The solution proposed by Heinz et al. (2003) is used in this research, with an implementation in *Python* environment using *PySptools* (Therein, 2018).

In scenarios when endmember spectra are unknown, the endmember spectra need to be derived first before the spectral unmixing is performed. For this purpose, methods such as N-FINDR are commonly utilized.

### 3.5. Bayesian Spectral Unmixing (BSU)

In contrast to the deterministic FCLS approach, which results in a single estimate of the abundances, BSU assumes that the abundances are unknown random variables characterized by probability distributions. As with other Bayesian approaches, the goal of the BSU method is to obtain estimates of these probability distributions, known as the *posterior distributions* (Aster et al., 2013). The latter represent the most general solution to the inverse problem and encodes everything we know about the parameters of interest given *prior* assumptions on their plausible values, assumptions on our forward model and observed data. This type of probabilistic approach offers a natural and general platform for assessing and/or modelling uncertainties (Gregory, 2005; Robert & Casella, 2010). In summary, BSU is developed within the general Bayesian framework by looking at the probabilistic relationship between the model parameters (abundance and the variance of the error in this case) and the observed data through the mixing model.

Following Bayes' Theorem, the conditional probability distribution of a model parameter ($m$) given observation ($y$) and a *prior probability* of model parameter can be expressed as:

$$p(m|y) = \frac{p(y|m)p(m)}{p(y)} \tag{11}$$

Where $p(m|y)$ denotes the *posterior probability* of the model parameter $m$ given the observed data. $p(y|m)$ denotes the probability of observing the data $y$ given a particular model parameter $m$; when a particular value of $y$ is considered, this probability function becomes a function of $m$ and is referred to as the *likelihood function* $L(m)$. The probability function $p(m)$ denotes the probability assigned to the model parameter $m$ before observing the data $y$; it is referred to as the *prior probability* of $m$.

The term $p(y)$ denotes the probability of observing the data $y$ regardless of any model parameter, which is also called *marginal likelihood* or *evidence*. $p(y)$ serves as a normalization factor to ensure the *posterior probability* integrates to one over all possible model parameters. In parameter estimation problems, an explicit consideration of $p(y)$ is not necessary, as it only acts as a normalization constant without affecting the shape of the *posterior distributions* (Aster et al., 2013). With these considerations, Eq. (11) is often rewritten as:

$$p(m|y) \propto L(m)p(m) \tag{12}$$

Where $\propto$ denotes proportionality and we have introduced $L(m) = p(y|m)$. In many cases of practical importance, analytical solutions to Eq. (12) are not feasible, and the only way to obtain estimates of it is via MCMC methods (Gregory, 2005). This method is implemented in this research to approximate the posterior distribution of the model parameters by generating a set of random samples that tends to converge toward the high-probability region of the posterior distribution. In the case of spectral unmixing performed in this study, the model parameters of interest are mineral abundances $\boldsymbol{a}$ and error variance $\sigma^2$. In the next section we will provide a high-level summary of MCMC algorithm that is employed in this research, followed by the description of all the main terms in Eq. (12) and the sampling methods.

#### 3.5.1. Summary of The MCMC method

In BSU, we aim to estimate the abundances of the endmembers and their associated uncertainties by analysing the full posterior distribution in Eq. (12). The full posterior distribution combines the likelihood function, which represent the probability of observing the data given a set of model parameters (i.e. mineral abundances and model variance), and the prior probability, which reflects our initial state of knowledge of the model parameters before observing the data. Detailed discussion of the likelihood and prior are presented in Section 3.5.2 and Section 3.5.3. In this section we will discuss the high-level summary of the methods.

We approximate Eq. (12) using a MCMC algorithm. Specifically, this research employs a variation of the Metropolis-Hastings (MH) algorithm (Hastings, 1970; Metropolis et al., 1953). The MH algorithm works by creating a MCMC chain that approximates the true posterior is created by accepting or rejecting proposed random samples at each iteration using a selection criterion: the Metropolis criterion (see Section 3.5.5). By selectively accepting proposed samples according to their probabilities, the MCMC algorithm constructs a chain with an equilibrium distribution equal to the posterior distribution (i.e. it replicates the *true posterior*). After sufficient number of iterations, the density of the MCMC chain will approximate the true posterior distribution of the model parameters.

#### 3.5.2. Likelihood Function

The likelihood function is a fundamental ingredient of Bayesian inference for assessing how well a given set of model parameters explains observed data. It measures the probability of the observed data given specific model parameter values within a statistical model. Following common practice, we assume that the errors ($\boldsymbol{n}$) in the mixture model Eq. (1) and Eq. (2) come from measurement (e.g. instrument noise) and modelling uncertainties that follow normal distributions and are independent and identically distributed[1]. With these assumptions, the likelihood function can be expressed as:

[1] In practice these assumptions are hard to test and validate but at this stage of analysis it is necessary to make as it makes the problem more tractable and allow us to continue and make progress with the analysis.

$$p(\boldsymbol{y}|\boldsymbol{E}\cdot\boldsymbol{a},\sigma^2) = L(\boldsymbol{E}\cdot\boldsymbol{a},\sigma^2) = L(\boldsymbol{a},\sigma^2)$$
$$= \frac{1}{(2\pi\sigma^2)^{n/2}} \exp\left(-\frac{1}{2\sigma^2}\,||\boldsymbol{y}-\boldsymbol{E}\cdot\boldsymbol{a}||_2^2\right) \quad (13)$$

Note that in this likelihood function, $||\boldsymbol{y}-\boldsymbol{E}\cdot\boldsymbol{a}||_2^2$ represent the residual of the modelled spectra and the observed data. The lower the residual term, the better the modelled spectra fit the observed data and the higher the likelihood of the model. The likelihood function thus integrates our theoretical model ($\boldsymbol{E}\cdot\boldsymbol{a}$), the data ($y$) and the model variance ($\sigma^2$) into a single function. The variance is commonly considered a constant, but in this research, we will also consider it as a model parameter and seek estimates of its posterior probability. A higher variance will result in the broader uncertainty and vice versa.

The endmember matrix $\boldsymbol{E}$ is considered known and constant, either as a result of an endmember extraction algorithm, independent measurement, or spectral libraries. The values of $\boldsymbol{a}$ and $\sigma^2$ are treated as free parameters that are partly controlled by their prior probability, as discussed below.

#### 3.5.3. Prior Probability

Bayesian models require a formulation of prior information about the model parameters. For our problem, the main model parameters are the abundances of the mineral phases in the mixture. As with any compositional data, the mineral abundances need to be non-negative and sum-to-one. The Dirichlet distribution $\mathcal{D}(\boldsymbol{a})$, also known as the multivariate beta distribution, satisfy these conditions (Ng et al., 2011) and it is therefore chosen as the prior probability distribution for the abundance parameters. The probability density function of a Dirichlet distribution can be written as:

$$p(\boldsymbol{a}|\boldsymbol{\alpha}) = \frac{\Gamma\left(\sum_{i=1}^{K}\alpha_i\right)}{\prod_{i=1}^{K}\Gamma(\alpha_i)} \prod_{i=1}^{K} {a_i}^{\alpha_i-1} \quad (14)$$

Where $\{a_i\}_{i=1}^{1=K}$ belongs to $K-1$ simplex, i.e. non-negative and sum-to-one, and $\Gamma(\cdot)$ is the gamma function. The Dirichlet distribution has one hyperparameter $\boldsymbol{\alpha}$ which describes the spread and centrality of the distribution in the simplex. To describe the lack of strong prior knowledge on the abundance parameter, $\boldsymbol{\alpha}$ is commonly fixed with a value of one, such as $\{\alpha_{1,}\alpha_{2,},\dots,\alpha_{K,}\} = \{1,1,\dots,1\}$. This means that the prior probability of abundance for each mineral is uniform on the simplex or equally likely for every value as long as it is non-negative, and the sum equals one.

For three parameters, the Dirichlet distribution can be visualized with a ternary diagram. The influence of $\boldsymbol{\alpha}$ in three parameters case is shown in Figure 7. In the case of a uniform Dirichlet distribution, the probability for any point outside the triangle is $0$ and the probability of any point inside the triangle is a constant.

The variance parameter is non-negative by definition, and for this case, the value is expected to be small or near zero. Following the recommendation of Gelman (2006) for such a requirement, the Half-Cauchy distribution $\mathcal{HC}(\varphi,\tau)$ is chosen for this parameter. The probability density function of the Half-Cauchy distribution is described as:

$$p(\sigma^2|\varphi,\tau) = \frac{2}{\pi\tau\left(1+\left(\frac{\sigma^2-\varphi}{\tau}\right)^2\right)} \quad (15)$$

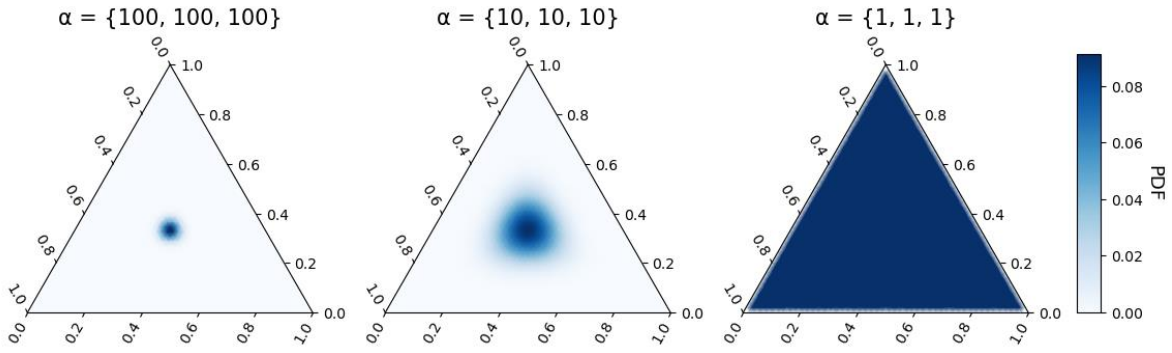


**Figure 7.** Illustrations for three parameters Dirichlet distributions with different value of $\boldsymbol{\alpha}$. The right most illustration where $\boldsymbol{\alpha} = \{1,1,1\}$ is uniform Dirichlet which is used as prior probability distribution for abundance in this study.

In this case, $\sigma^2$ depends on the location hyperparameter ($\varphi$) and scale hyperparameter ($\tau$) which influence the peak, and the spread of the Half Cauchy distribution as illustrated in Figure 8. In this research we will generally assume that $\varphi$ is a constant based on our understanding of the uncertainty, and let $\tau$ as a free parameter following a Jeffrey uninformative *hyperprior* defined by:

$$p(\tau) = \frac{1}{\tau} \tag{16}$$

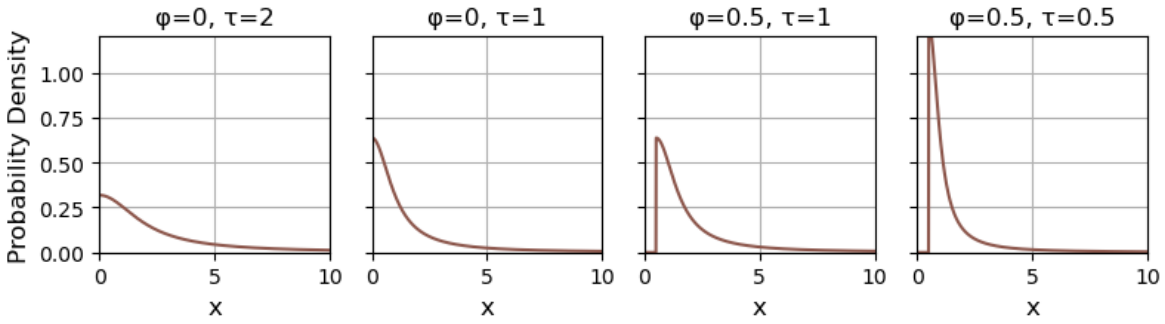


**Figure 8.** Illustrations for the influence of different values of $\varphi$ and $\tau$ for Half Cauchy distributions.

### 3.5.4. Posterior

By substituting the likelihood function and prior probability into the posterior in Eq. (12), and assuming independence between $\boldsymbol{a}$ and $\sigma^2$, the posterior becomes:

$$p(\boldsymbol{a}, \sigma^2|\boldsymbol{y}) \propto L(\boldsymbol{a}, \sigma^2) p(\boldsymbol{a}|\boldsymbol{\alpha})\, p(\sigma^2|\varphi, \tau)\, p(\tau) \tag{17}$$

With $\boldsymbol{E}$, $\boldsymbol{\alpha}$, and $\varphi$ assumed constant, as described in previous sections. The Figure 9 below illustrates the hierarchical relationships among the variables in Eq. (17). For numerical stability, the calculations for Eq. (17) will be performed in the natural logarithm domain.

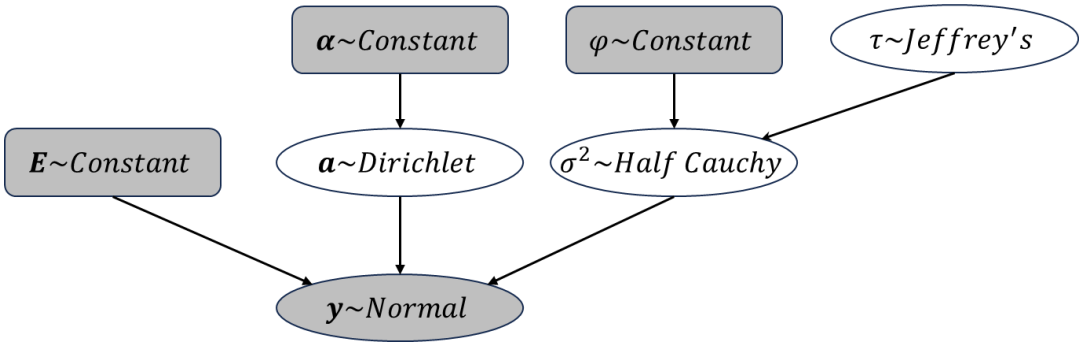


**Figure 9.** Directed Graph illustrating the hierarchical relationship between parameters in posterior described in (17)

#### 3.5.5. Sampling Strategy

To be able to evaluate the full posterior probability of the model parameters from Eq. (17), MCMC sampling strategy is implemented to sample a series of random values for $\boldsymbol{a}, \sigma^2$, and $\tau$ in a manner that ensures convergence toward the actual probability distribution. In MCMC sampling chains, the probability of a random model parameter $\theta_r$ to be accepted as a sample only depends on previously accepted random samples $\theta_{r-1}$ by evaluating the proposed random samples $\theta_{prop}$.

The sampling method that is employed in this research is a variation of the MH algorithm (Hastings, 1970; Metropolis et al., 1953). The parameters are sampled one at a time where in each iteration there is a 50% probability of updating any given parameter, meaning that each parameter has an equal chance of being selected for an update.

At every iteration, a random sample from the model parameters $\theta_{prop}$. is proposed following a proposal distribution $(q)$. This proposal distribution is a probability distribution that defines the probability of proposing a new random sample given the previously accepted sample. The proposed move $\theta_{prop}$ will be accepted as the current sample in the chain $\theta_r$, or get rejected based on the Metropolis acceptance criterion (Aster et al., 2013), sets as:

$$\theta_r \begin{cases} \theta_{prop} & , \ \alpha(\theta_{r-1}, \theta_{prop}) \geq u \\ \theta_{r-1} & , \ \alpha(\theta_{r-1}, \theta_{prop}) < u \end{cases} \tag{18}$$

Here $u \sim \mathcal{U}(0,1)$ is a random number between 0 and 1, and $\alpha(\theta_{r-1}, \theta_{prop}) = \min(1, R)$ is the *acceptance probability* where:

$$R = \frac{p(\theta_{prop}|y)}{p(\theta_{r-1}|y)} \frac{q(\theta_{r-1}|\theta_{prop})}{q(\theta_{prop}|\theta_{r-1})} \tag{19}$$

As the posterior is calculated in logarithm scale, log of $R$ and $u$ will be used instead.

The proposal distribution therefore plays an important role in the efficiency of the sampling process. If the spread of the proposal distribution is too wide, the random samples might explore the whole parameter space quickly, but many proposed samples will be rejected since they fall in low-probability region of the posterior distribution. If the spread is too narrow, a high number of proposed samples might be accepted, but the chain could be too slow to reach the high-probability area. Therefore, it is essential to tune the spread of the proposal distribution to explore the parameter space efficiently without rejecting too many samples. In this research, we used acceptance ratio as a proxy for sampling efficiency.

Whenever possible, we aim to tune the acceptance ratio be around $25\%$ to $50\%$ (Gregory, 2005; Robert & Casella, 2010)

#### 3.5.5.1. Sampling for $\boldsymbol{a}$

Since abundance is strictly bounded by non-negativity and sum-to-one constraints, a proposal distribution that can sensibly sample this parameter is also a Dirichlet distribution, which is the same as its prior probability distribution.

$$\boldsymbol{a}_{prop} \sim \mathcal{D}(\mathrm{t}_1(\boldsymbol{a}_r + \varepsilon)) \tag{20}$$

Note that in (20), $\mathrm{t}_1(\boldsymbol{a}_r + \varepsilon)$ is used as $\boldsymbol{a}$, instead of $\{1,1,\dots 1\}$ as in the prior probability distribution. Here $\mathrm{t}_1$ is a constant representing the spread of the proposal distribution and $\varepsilon$ is a small value that prevents division by zero in (14) in case some of the endmember abundance is absent from the mixture. This setup makes the proposal distribution to be always cantered around the previous sample with spread defined by $\mathrm{t}_1$. Figure 10 illustrate the influence of $\mathbf{a}$ and $\mathrm{t}_1$ to the Dirichlet proposal distribution shape.

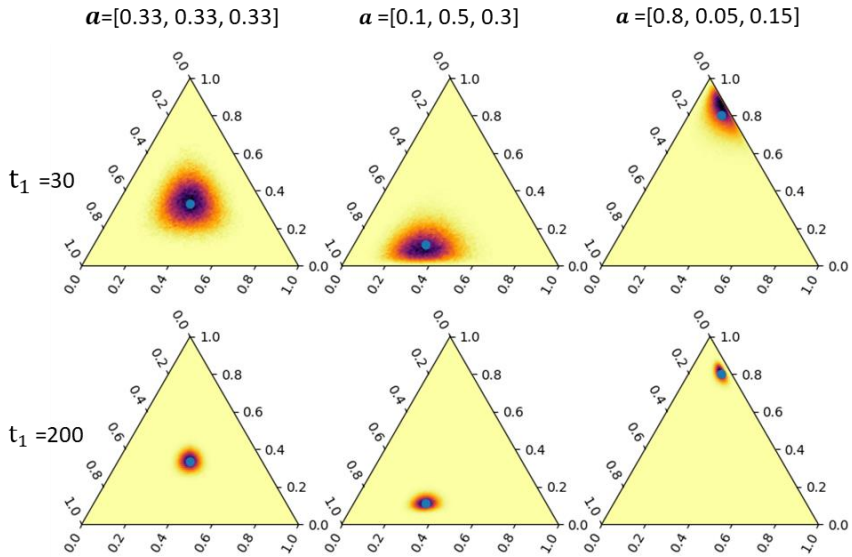


**Figure 10.** Three parameters' illustrations for the influence of $\boldsymbol{a}$ and $t_1$ for the shape of Dirichlet distributions used a proposal distribution.

To calculate acceptance ratio for $\boldsymbol{a}$, we derive $R$ from (19). In logarithm form, it defined as:

$$\log R = \log p(\boldsymbol{a}_{prop}, \sigma^2_{r-1}|\boldsymbol{y}) - \log p(\boldsymbol{a}_{r-1}, \sigma^2_{r-1}|\boldsymbol{y}) + \log q_1(\boldsymbol{a}_{r-1}|\boldsymbol{a}_{prop}) - \log q_1(\boldsymbol{a}_{prop}|\boldsymbol{a}_{r-1}) \tag{21}$$

Here, $\log p(\boldsymbol{a}_{prop}, \sigma^2_{r-1}|\boldsymbol{y})$ and $\log p(\boldsymbol{a}_{r-1}, \sigma^2_{r-1}|\boldsymbol{y})$ represent the log posterior probabilities of the proposed and previously accepted values of $\boldsymbol{a}$, respectively, as defined by Eq. (17). The term $\log q_1(\boldsymbol{a}_{r-1}|\boldsymbol{a}_{prop})$ and $\log q_1(\boldsymbol{a}_{prop}|\boldsymbol{a}_{r-1})$ correspond to the log probability density function of the proposed value of $\boldsymbol{a}$ given the previously accepted value and vice versa, which in the case of Dirichlet distribution, can be computed using Eq. (14).

#### 3.5.5.2. Sampling for $\sigma^2$ and $\tau$

In accordance with the hierarchical structure outlined in Section 3.5.4, the initial step involves proposing a random value for $\tau_{prop}$. This proposed sample is generated from a normal distribution, with the mean set to the last accepted value of $\tau_{r-1}$ and a standard deviation of $t_2$. Given that $\tau$ is expected to be close to zero, this method may often propose negative values, potentially reducing the efficiency of the sampling process. To address this issue, the logarithm of $\tau_{prop}$ is sampled first using the log of $\tau_{r-1}$ as the mean. For $u = \log \tau_{prop}$, we have:

$$u \sim \mathcal{N}(\log \tau_{\boldsymbol{r-1}}, t_2) \tag{22}$$

The actual value of $\tau_{prop}$ can be obtained afterwards by the inverse transformation of $u$, where $\tau_{prop} = e^u$. Using this value, the sample for $\sigma^2_{prop}$ then can be proposed directly from the Half Cauchy distribution:

$$\sigma^2_{prop} \sim \mathcal{HC}(0, \tau_{prop}) \tag{23}$$

This transformation of model parameters requires additional Jacobian terms in the acceptance ratio to accommodate the change in parameter space (Gelman et al., 2013). The Jacobian term $(J)$ in this case can be described as:

$$J = \left| \frac{d}{du} e^u \right| = e^u \tag{24}$$

This Jacobian term needs to be added for the proposed sample and previously accepted sample in calculation of the acceptance ratio. In logarithm form $R$ from (19) then can be described as:

$$\log R = \log p(\boldsymbol{a}_{r-1}, \sigma^2_{prop} | \boldsymbol{y}) - \log p(\boldsymbol{a}_{r-1}, \sigma^2_{r-1} | \boldsymbol{y}) + \log q_2(\tau_{r-1} | \tau_{prop}) - \log q_2(\tau_{prop} | \tau_{r-1}) + \log \tau_{prop} - \log \tau_{r-1} \tag{25}$$

Where $\log q_2(\tau_{r-1} | \tau_{prop})$ and $\log q_2(\tau_{prop} | \tau_{r-1})$ correspond to the log probability density function of the proposed value of $\tau$ given the previously accepted value and vice versa. Since the proposal distribution in symmetrical, then $\log q_2(\tau_{r-1} | \tau_{prop}) - \log q_2(\tau_{prop} | \tau_{r-1}) = 0$.

#### 3.5.5.3. MCMC sample post-processing

Since MCMC chains are initiated with a random point (usually with low probability) in parameter space, it takes *n* iterations until the high probability region of the posterior is found by the sampler. To get a reliable estimate of the posterior distribution, these samples need to be discarded from the chain. This initial period of sampling, before the chain starts sampling the true posterior, is called the *burn-in* period.

There exist different metrics and approaches to estimate burn-in periods, but the simplest, and arguably the most effective, is visually inspecting the trace plots of the sampling chains. Trace plots are diagnostic tools in MCMC, where the sampling chains are plotted against the iteration number. The burn-in period can be identified in the trace plots by looking at the point where the samples start to become stationary (i.e. sample values fluctuating around a stable mean). Figure 11 shows an example of a trace plot of a single model parameter and its burn-in period threshold.

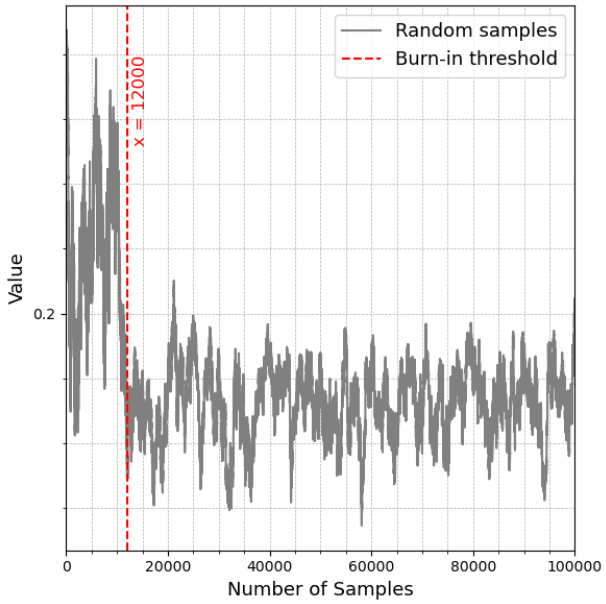


**Figure 11.** Example of trace plot of a single MCMC chains and how it can be used to identify the burn-in periods. In this example, the *burn-in* threshold can be identified at $x = 12000$.

The expected value for the model parameter can be estimated by taking a statistical measure of central tendency (mean, median, or mode) of the *marginal posterior distribution* or the subset of the posterior distribution for a given model parameter. When the marginal posterior distribution is approximately Gaussian, the mean, median, and mode will essentially be the same. Unless stated otherwise, the median value is used in this thesis as the measure of the expected value. The confidence interval of the estimation is defined as the range between the $5^{th}$ percentile to the $95^{th}$ percentile.

### 3.6. Accuracy Assessment

Two types of accuracy measure are used in the study. For spectral unmixing accuracy, the abundance values obtained from the spectral unmixing are compared with the actual abundance values. RMSE will be used to measure the accuracy and in the report will be referred to as *Prediction Error*

$$Prediction\ Error = \sqrt{\sum_{i=1}^{n} \frac{(\hat{a}_n - a_n)^2}{n}} \times 100\% \tag{26}$$

Where $n$ is the number of endmembers, $\hat{a}_n$ is the spectral unmixing abundance estimation of endmember $n$ and $a_n$ is the actual abundance values of endmember $n$.

Other accuracy measurement is the measure of fit between the modelled spectra and the actual observed spectra which referred as the reconstruction error:

$$Reconstruction\ Error = \frac{\sqrt{\sum_{i=1}^{n} \frac{(\hat{y}_i - y_i)^2}{n}}}{\max(\boldsymbol{y}) - \min(\boldsymbol{y})} \times 100\% \tag{27}$$

Where $\hat{\boldsymbol{y}}$ is the modelled/reconstructed spectra and $\boldsymbol{y}$ is the observed mixed spectra. This is essentially a Root Mean Square Error (RMSE) divided by the data range, allowing an objective comparison of errors

between two datasets irrespective of their range. Note that the result of a BSU analysis is not a single estimate, but a multi-dimensional probability function. In order to apply Eq. (26) and Eq. (27) to this case, an expectation value needs to be assigned first. Unless indicated otherwise, we will use the median of the posterior distributions.

Reconstruction Error also used as the measure to compare the performance between mixture models. Following the mixture model described in Eq. (1) and Eq. (2), mixed spectra can be modelled or reconstructed if the pure endmember spectra and their fractional abundance are known. This operation is often referred to as a forward operation as opposed to the unmixing problem, which is an inverse operation. In this study, we refer to the forward operation as *spectral reconstruction*. We used spectral reconstruction to compare the performance between two mixture models. Since all variables in Eq. (1) and Eq. (2) are known, the reconstructed spectra ($\hat{\boldsymbol{y}} = \boldsymbol{Ea} + \boldsymbol{n}$) can be compared to the actual measured mixed spectra $(\boldsymbol{y})$ for both the reflectance and the SSA spectra. The difference between the measured and the reconstructed spectra is referred to as the reconstruction error which is defined by:

### 3.7. Research Stages

Before applying BSU to real samples, an initial analysis was conducted on a simpler, synthetic dataset to gain a better understanding of the problems and to evaluate the performance of the methods. Given that BSU on hyperspectral image is computationally expensive, these preliminary experiments were necessary to refine the unmixing approach and optimize resource usage. The research was structured in the following stages:

The first stage involved creating computer-generated mixtures of known compositions, specifically of calcite, quartz, muscovite, and kaolinite spectra from USGS Spectral Library. The objective of this stage was to validate the implementation of BSU and understand its behaviour in a controlled environment. The results were evaluated by comparing the estimated abundances and variance values against the known inputs. This stage aimed to ensure that BSU provides accurate results. The results were also compared with those obtained using FCLS.

The second stage focused on unmixing real powder mixtures, for testing in a more complex and realistic scenario. Actual powder mixtures of calcite, quartz, muscovite, and kaolinite were used. Different assumptions on mixture models were first tested to determine the most suitable mixture model for representing the mineral mixtures. The performance of BSU was evaluated in this condition and also compared with FCLS. Additionally, the influence of different spectral processing techniques on the unmixing results was examined. This stage aimed to refine the BSU methodology and assess its robustness and accuracy in more complex conditions, providing insights into the practical challenges in unmixing of real physical datasets.

Building upon the understanding gained from these experiments, the final stage involved in applying the refined unmixing strategy with BSU in a core sample. The results were compared to those from FLCS to highlight the strengths and limitations of BSU practical applications.

# 4. RESULTS

## 4.1. Computer-Generated Mixtures

For the first experiment, a mixed spectrum composed of $10\%$ calcite, $30\%$ quartz, $40\%$ muscovite, and $20\%$ kaolinite was generated using the endmember spectra from the USGS Spectral Library (Figure 1) and the LMM (as explained in the Section 5.2.2, the choice of LMM, H1 or H2 is immaterial in this case as all options produce similar results). The resultant mixed spectrum was then contaminated by Gaussian noise characterized by a mean of $0$ and varying variance $(\sigma^2)$ as shown in Figure 12.

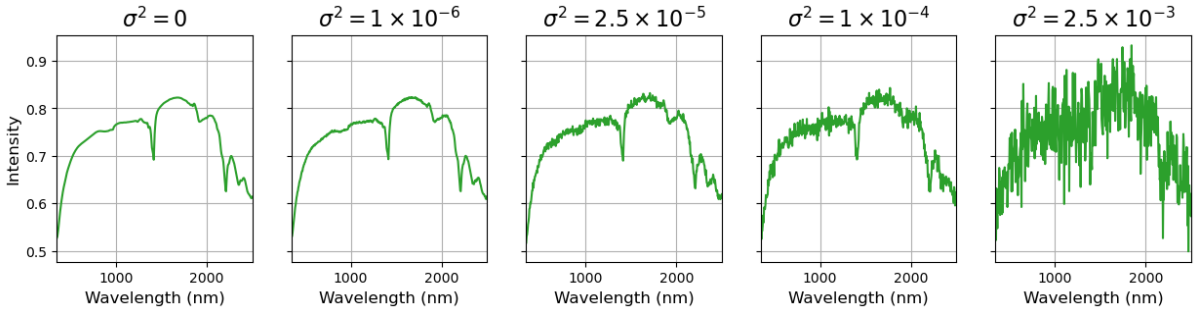


**Figure 12.** Computer-generated mixtures of $10\%$ calcite, $30\%$ quartz, $40\%$ muscovite, and $20\%$ kaolinite contaminated by Gaussian noise with different $\sigma^2$

Provided the mixed spectra carries enough information content, a correct implementation of the BSU algorithm should be able to retrieve the full posterior distribution of all model parameters, including that of the added variance (i.e. the data noise). We will use the spectra contaminated with the most extreme Gaussian noise $(\sigma^2 = 2.5 \times 10^{-3})$ as an example to illustrate the procedure of BSU and its key difference with FCLS.

As stated in Section 3.5.5, to ensure the efficiency of the BSU algorithm, step sizes $(t_1, t_2)$ need to be tuned heuristically. In this case we obtain the step size of $t_1, = 1{,}000$ and $t_2 = 0.1$ resulting in acceptance ratio of abundance $\boldsymbol{a} = 46.7\%$ and $\sigma^2 = 5.66\%$.

After tuning the step size, the next step is to remove the burn-in samples. Figure 13 displays the trace plots of the BSU results for all model parameters. The top row of the figure shows that the random sample for $\boldsymbol{a}$ and $\sigma^2$ initially start from arbitrary values and eventually settle into a stationary phase, oscillating around a single mean. These initial random samples before the chain becomes stationary is what referred to as burn-in samples (see Section 3.5.5.3). In this case we set the burn-in threshold as $n = 5{,}000$, indicating that the first $5{,}000$ random samples were discarded. The bottom row of the Figure 13 shows the sampling chain after the burn in samples is removed. This steps of tuning the step size and removing the burn in period need to be done in BSU to acquire a representative random sample of the posterior. To keep the report concise, we will no longer include trace plots for subsequent BSU results.

One of the key advantages of BSU is that the full posterior distribution provides a comprehensive understanding of the uncertainties and correlations between model parameters. However, the full posterior distribution of the model parameters is complex to visualize as it exists in a high-dimensional parameter space. To address this, corner plots containing joint distributions and marginal distributions are typically used to visualize the results (Figure 14). This plot provides a visualization of the marginal posterior distribution of each model parameter and its corelations between other model parameters.

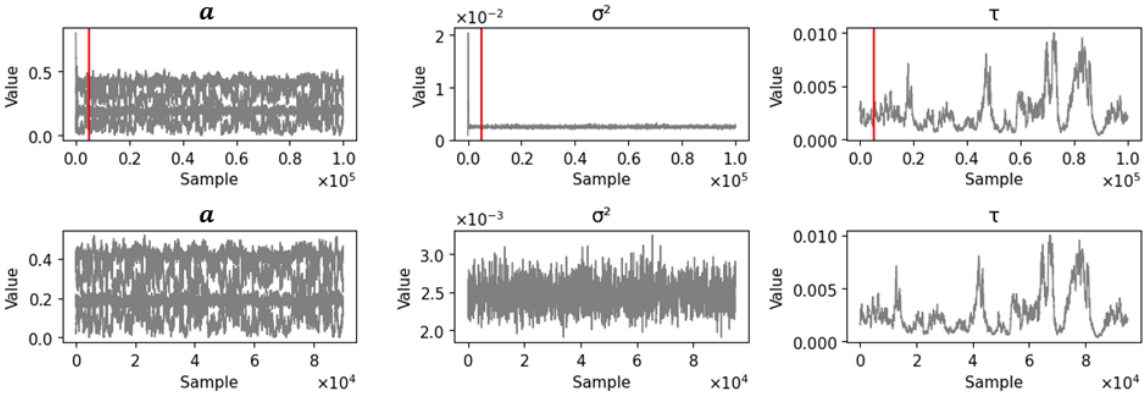


**Figure 13.** Trace plot illustrating the sampling chains of BSU for the sample with noise level of $\sigma^2 = 2.5 \times 10^{-3}$ (Figure 12 right) before burn-in removal (top row) and after $n = 5000$ burn-in removal (bottom row)

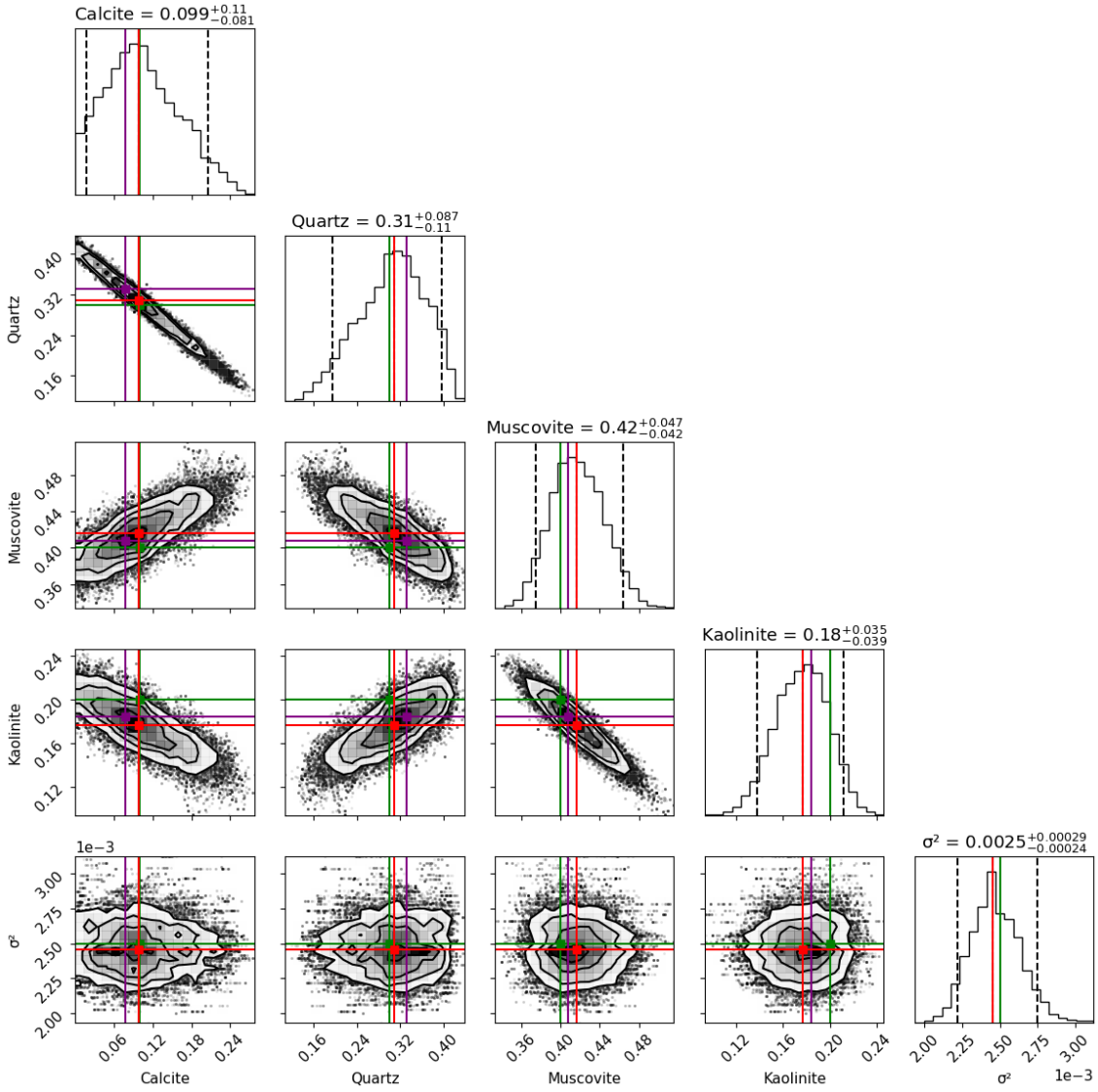


**Figure 14.** Corner plot of model parameters for the sample with noise level of $\sigma^2 = 2.5 \times 10^{-3}$ (Figure 12 right). The red line represents the expected value of BSU result (median). Dashed lines in the histogram plots represent the 90% confidence intervals. Green lines represent the true values. Purple lines represent FCLS results (for comparison). Result for $\tau$ is not shown for clarity and because it is not a model parameter of interest.

In Figure 14, the plot displays one-dimensional histograms along the diagonal which represent the marginal posterior distributions of each model parameter. The off-diagonal plots show the density plots of pairwise correlations between model parameters. This allows us to observe not only the uncertainty associated with each parameter, but also how changes in one parameter might affect another.

In this case, we can observe that calcite-quartz, quartz-muscovite, muscovite-kaolinite, and calcite-kaolinite exhibit strong negative correlations. This means that an increase in one parameter is accompanied by the decrease in the other. On the other hand, calcite-muscovite and quartz-kaolinite show positive correlations, indicating that an increase in one parameter is accompanied by an increase in the other.

As expected, given the simple setup, the single-value prediction from FCLS and the expected values (median) from BSU are in good agreement with the true values. Importantly, BSU was also able to retrieve the variance value with a good precision.

Figure 15 illustrates further how FCLS differs from BSU in modelling the observed mixed spectrum. In this example of spectra with high Gaussian noise, FCLS attempts to fit a single spectrum that minimizes the overall error the data. On the other hand, BSU models the observed spectrum by a distribution of spectra that is likely to be the true spectrum under the given noise, which in Figure 15 is represented by the range of 5$^{th}$ and 95$^{th}$ percentile of the distribution (90% confidence interval). This distribution of spectra is directly related to the distribution of abundance parameter shown in Figure 14.

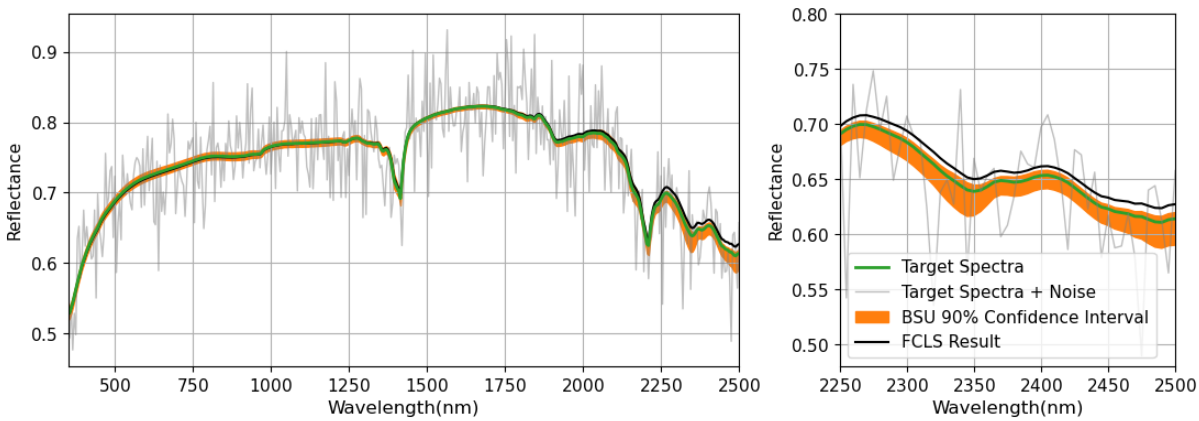


**Figure 15.** Modelled spectra obtained from the unmixing results of FCLS and BSU of computer-generated sample contaminated with gaussian noise of $\sigma^2 = 2.5 \times 10^{-3}$ (Figure 12 right).

In a practical application, we are interested in the accuracy of the mineral abundance obtained by the spectral unmixing. In this research, we are measuring this accuracy in terms of RMSE of the predicted abundance and the real abundance value, which is referred to as the prediction error (see Section 3.6). With reference to the 5 set of spectra shown in Figure 12, the prediction errors of BSU and FCLS are presented in Table 3. While the prediction errors of BSU is generally smaller than those of FCLS, the difference is small and both approaches show robustness even under the influence of extreme Gaussian noise.

To further evaluate the algorithm, $100$ additional computer-generated mixtures were created. This time using a more reasonable gaussian noise of $2.5 \times 10^{-5}$. Each mixture was unmixed using BSU and FCLS. The distribution of the prediction errors is shown in Figure 16. The mean prediction errors for BSU and FCLS are $0.415\%$ and $0.512\%$, respectively. These results indicates that our implementation of the BSU explained in Section 3.6 is correct.

**Table 3.** Comparison of prediction error between FCLS and BSU for five spectra presented in Figure 12.

| Prediction Error (%) | | | | | |
|---|---|---|---|---|---|
| *Unmixing Method* | *Gaussian Noise Variance ($\sigma^2$)* | | | | |
| | 0 | $1 \times 10^{-6}$ | $2.5 \times 10^{-5}$ | $1 \times 10^{-4}$ | $2.5 \times 10^{-3}$ |
| FCLS | 0.027 | 0.168 | 0.068 | 1.234 | 2.091 |
| BSU | 0.001 | 0.142 | 0.048 | 1.245 | 1.467 |

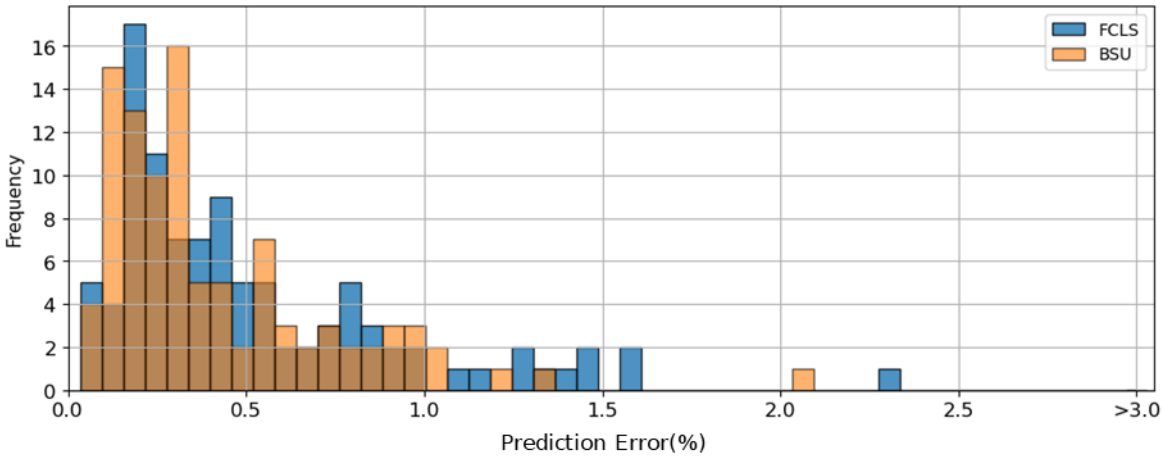


**Figure 16.** Prediction Error histograms of FCLS and BSU from 100 computer-generated samples.

The computations were performed on the ITC Geospatial Computing Platform (Girgin, 2021) equipped with 72 vCPUs (Intel x86-64), 768 GB RAM, and an NVIDIA RTX A4000 GPU. The process utilized only a single thread. For 100 spectra, the computation time was 0.08 seconds for FCLS and 276.95 seconds for BSU.

## 4.2. Powder Mixtures Result

With the powder mixture data, we can assess how well the mixture models reconstruct measurements and how effectively BSU identifies the modal composition of real mixtures. The spectra measurement results of all powder samples are included in Appendix 1. Additionally, the influence of different spectral processing methods was also explored.

### 4.2.1. Spectral Reconstruction of Mixture Models

In analysing the powder mixtures, all variables in Eq. (1) and Eq. (2) were known, allowing a test for the ability of the mixing model to describe the data. This section reconstructs and compares the mixed spectra using three mixture models: the linear mixture model (LMM), and linearized mixture model using Hapke Model with the assumption of isotropic scattering (H1), and anisotropic scattering (H2) (See Section 3.1 for detail description of the mixture model). Eq. (1) were used for LMM, and the operation is straightforward. For H1 and H2 reflectance data should be converted first to SSA before Eq. (2) was used for reconstruction. The endmember spectra used for reconstruction are shown in Figure 17.

From Figure 17, we can visually observe that the SSA spectra obtained with the Hapke Model (both H1 and H2) tends to compress the spectra towards higher values (i.e. closer to one) due to the non-linear nature of the Hapke Model. As a result, the spectra of calcite and quartz have similar SSA along the

considered wavelength range. Additionally, the difference in assumptions between H1 and H2 does not result in significantly different SSA spectra.

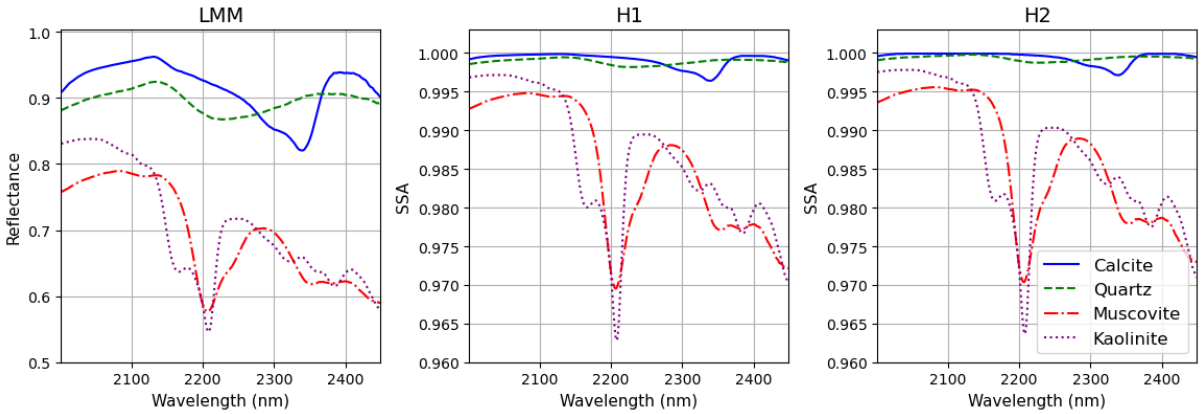


**Figure 17.** Endmember spectra used for spectral reconstruction using LMM, H1 and H2 mixture models. Note the different y-axis for reflectance spectra and SSA spectra.

To measure the performance of each mixing model, we are using reconstruction error which are defined as relative RMSE of the modelled spectra and the observed spectra (see Section 3.6). Table 4 lists the reconstruction error for each powder mixture. The reconstruction error of LMM is 10.17%, for H1 is 1.80%, and for H2 is 1.81%. Overall, both H1 and H2 have significantly smaller reconstruction error compared to LMM. The reconstruction results of LMM, H1, and H2 mixture models for CM sample series are shown in Figure 18 (See Appendix 2 for the reconstruction of the whole samples).

**Table 4.** Reconstruction Error of each sample of using the three different mixture models.

| ***Average Reconstruction Error (%)*** | | | |
|---|---|---|---|
| ***Sample*** | ***LMM*** | ***H1*** | ***H2*** |
| CK1 | 3.27 | 0.53 | 0.57 |
| CK2 | 8.15 | 0.89 | 1.2 |
| CK3 | 15.52 | 1.22 | 0.97 |
| CK4 | 12.67 | 1.1 | 0.8 |
| QK1 | 13.08 | 2.71 | 2.21 |
| QK2 | 17.69 | 4.88 | 4.35 |
| QK3 | 8.72 | 1.73 | 1.52 |
| QK4 | 2.12 | 3.66 | 3.8 |
| CM1 | 5.76 | 2.53 | 2.41 |
| CM2 | 9.75 | 1.56 | 1.57 |
| CM3 | 12.24 | 2.13 | 2.78 |
| CM4 | 8.94 | 0.86 | 1.27 |
| CKM1 | 10.36 | 1.87 | 1.92 |
| CKM2 | 4.39 | 1.46 | 1.46 |
| CKM3 | 12.12 | 1.1 | 1.23 |
| CKM4 | 12.44 | 1.56 | 1.72 |
| CKMQ1 | 11.23 | 1.18 | 1.59 |
| CKMQ2 | 12.29 | 2.06 | 1.74 |
| CKMQ3 | 12.17 | 1.11 | 0.72 |
| CKMQ4 | 10.44 | 1.93 | 2.48 |
| Average | **10.17** | **1.80** | **1.81** |

Additionally, we also tested the influence of different spectral processing methods on the reconstruction of the observed spectra. The results of these tests are summarized in Table 5. Across all three mixture models, each spectral processing method consistently reduced the reconstruction error, with the first derivative method showing the most significant improvement.

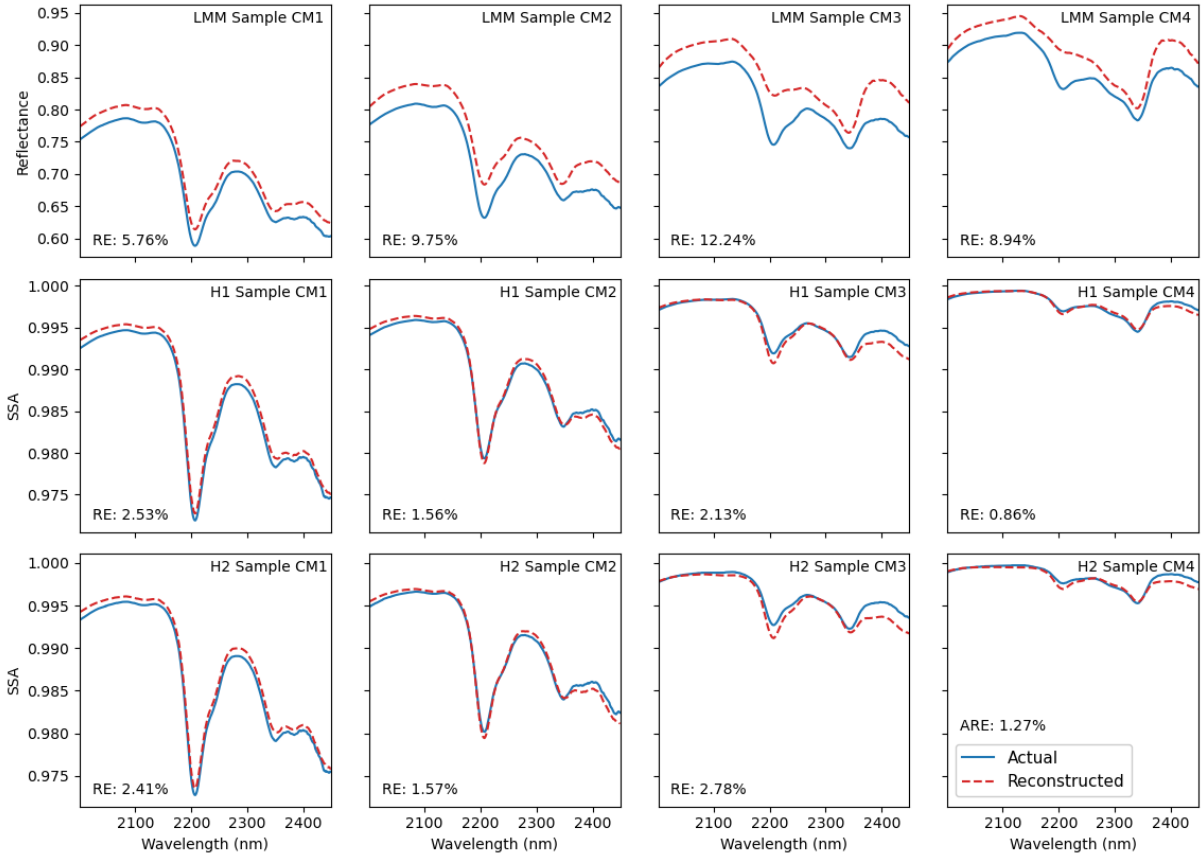


**Figure 18.** Comparison between actual spectra and reconstructed spectra of CM sample series with LMM (top row), H1 (middle row), and H2 (bottom row). CM 1 consist of 11% calcite and 89% muscovite, CM 2 consist of 31% calcite and 69% muscovite, CM3 consist of 71% calcite and 29% muscovite, and CM4 consist of 90% calcite and 10% muscovite.

**Table 5.** Influence of spectral processing method for spectra reconstruction of the powder mixtures with each mixture model.

| | **Reconstruction Error (%)** | | | |
|---|---|---|---|---|
| *Mixture Model* | *No Additional Processing* | *Hull Removal* | *First Derivative* | *Normalization* |
| LMM | 10.17 | 5.13 | 3.35 | 4.32 |
| H1 | 1.80 | 1.34 | 0.81 | 1.32 |
| H2 | 1.81 | 1.31 | 0.84 | 1.34 |

#### 4.2.2. Spectral Unmixing of Powder Mixtures

The H1 mixture model was chosen for the spectral unmixing of the powder mixtures, as it demonstrated a high accuracy in terms of reconstruction error and faster computation time. For a better performance of the BSU, we will include information about the expected value related to the uncertainty in its prior probability. Using the same H1 model, Mustard & Pieters (1989) reported errors of up to 6% for high albedo materials. In the spectra reconstruction test conducted for H1 in this study, we also observe a high

reconstruction error up to 4.88% (Table 4). As we are not yet explicitly considering any other source of uncertainty, we will use a conservative estimate of 6% for this study, which for our data translates to $\varphi = 5 \times 10^{-6}$ for our prior probability. The step sizes $t_1 = 1{,}000$ and $t_2 = 1$ were selected heuristically, resulting in acceptance ratios of $46.85\%$ for $\boldsymbol{a}$ and $6.68\%$ for $\sigma^2$.

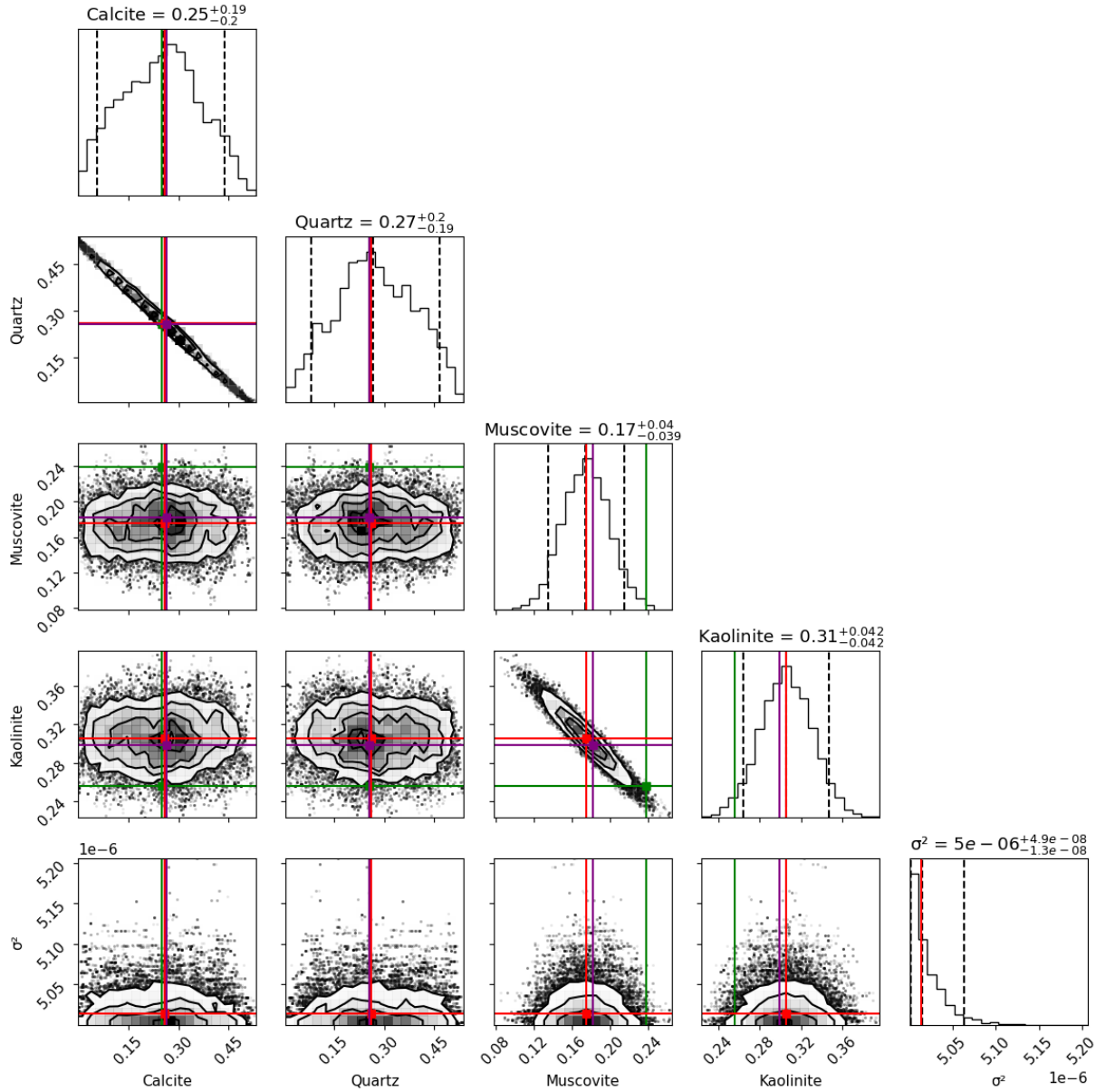


**Figure 19.** Corner plot for the posterior distribution of sample CKMQ 1. The red line represents the expected value of BSU result (median) with the stripped lines in histograms represent its 90% confidence interval, green line represents the actual values, and purple line represent FCLS results for comparison.

The resulting posterior distribution for sample CKMQ 1 is presented in Figure 19, with its corresponding modelled spectra shown in Figure 20. CKMQ 1 sample was chosen as an example because it contains all four minerals, and its posterior distribution is representative of all other samples with four minerals. The prediction error of this sample is $4.04\%$. We get generally good estimates of quartz and calcite, with their true values within the $90\%$ confidence interval of the posterior. In contrast, the 'true' value of muscovite and kaolinite lie outside the $90\%$ confidence interval of the posterior, but still within the range of the

possible values. The same observation can be made for all other samples, which are summarized in Table 6. We will discuss further about this observation in Section 5.2.2.

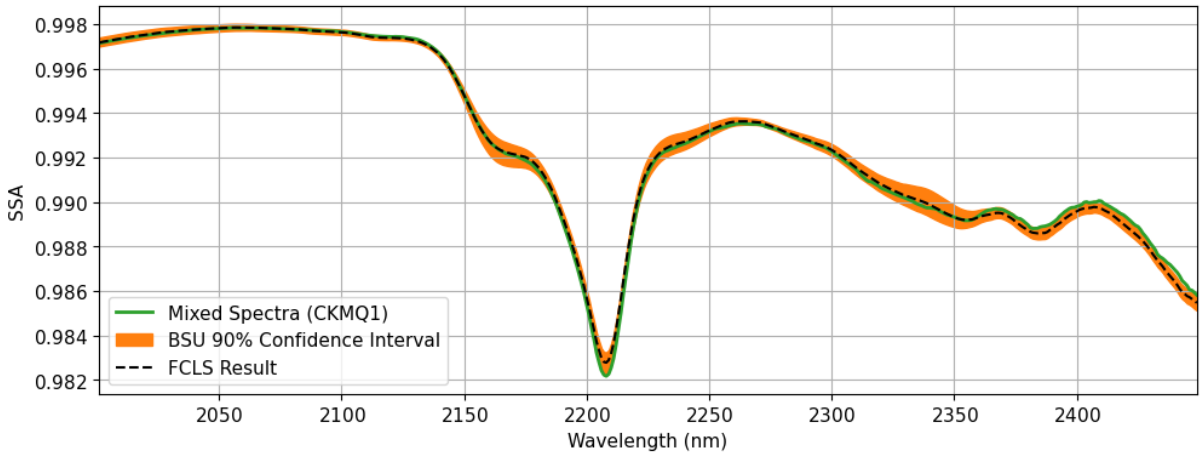


**Figure 20**. Modelled spectra obtained from the unmixing results of FCLS and BSU sample CKMQ 1.

**Table 6.** BSU results for all powder mixture samples. P50 represent the median or the expected value of the BSU estimate, and P95-P5 represent the 90% confidence interval of the estimate. Green font mean that BSU result is higher than the actual value; red font means the result is lower than the actual value. The average prediction error of all samples is 4.13%.

| Sample | Calcite | | | Quartz | | | Muscovite | | | Kaolinite | | | Prediction |
|---|---|---|---|---|---|---|---|---|---|---|---|---|---|
| | *Actual* | *P50* | *P95-P5* | *Actual* | *P50* | *P95-P5* | *Actual* | *P50* | *P95-P5* | *Actual* | *P50* | *P95-P5* | **Error** |
| *CK1* | 0.10 | 0.05 | 0.09 | 0.00 | 0.06 | 0.09 | 0.00 | 0.02 | 0.04 | 0.90 | 0.88 | 0.05 | **4.09** |
| *CK2* | 0.30 | 0.20 | 0.24 | 0.00 | 0.11 | 0.25 | 0.00 | 0.01 | 0.04 | 0.70 | 0.67 | 0.05 | **7.29** |
| *CK3* | 0.69 | 0.59 | 0.22 | 0.00 | 0.08 | 0.22 | 0.00 | 0.02 | 0.04 | 0.31 | 0.31 | 0.05 | **6.27** |
| *CK4* | 0.89 | 0.81 | 0.20 | 0.00 | 0.06 | 0.20 | 0.00 | 0.02 | 0.05 | 0.11 | 0.11 | 0.06 | **4.86** |
| *QK1* | 0.00 | 0.08 | 0.21 | 0.90 | 0.76 | 0.22 | 0.00 | 0.01 | 0.04 | 0.10 | 0.15 | 0.05 | **8.11** |
| *QK2* | 0.00 | 0.07 | 0.25 | 0.70 | 0.52 | 0.26 | 0.00 | 0.01 | 0.04 | 0.30 | 0.39 | 0.05 | **10.56** |
| *QK3* | 0.00 | 0.09 | 0.21 | 0.30 | 0.17 | 0.21 | 0.00 | 0.01 | 0.04 | 0.70 | 0.72 | 0.04 | **7.92** |
| *QK4* | 0.00 | 0.08 | 0.15 | 0.10 | 0.10 | 0.16 | 0.00 | 0.01 | 0.03 | 0.90 | 0.81 | 0.04 | **5.81** |
| *CM1* | 0.11 | 0.03 | 0.06 | 0.00 | 0.03 | 0.06 | 0.89 | 0.92 | 0.05 | 0.00 | 0.02 | 0.05 | **4.28** |
| *CM2* | 0.31 | 0.23 | 0.22 | 0.00 | 0.08 | 0.22 | 0.69 | 0.67 | 0.05 | 0.00 | 0.02 | 0.05 | **5.54** |
| *CM3* | 0.71 | 0.69 | 0.18 | 0.00 | 0.06 | 0.18 | 0.29 | 0.24 | 0.05 | 0.00 | 0.01 | 0.04 | **4.05** |
| *CM4* | 0.90 | 0.86 | 0.17 | 0.00 | 0.05 | 0.17 | 0.10 | 0.07 | 0.05 | 0.00 | 0.02 | 0.05 | **3.51** |
| *CKM1* | 0.35 | 0.24 | 0.24 | 0.00 | 0.10 | 0.25 | 0.29 | 0.16 | 0.08 | 0.36 | 0.50 | 0.08 | **12.09** |
| *CKM2* | 0.11 | 0.06 | 0.09 | 0.00 | 0.05 | 0.09 | 0.42 | 0.32 | 0.08 | 0.46 | 0.57 | 0.08 | **8.25** |
| *CKM3* | 0.44 | 0.32 | 0.30 | 0.00 | 0.12 | 0.30 | 0.11 | 0.08 | 0.08 | 0.45 | 0.48 | 0.08 | **9.04** |
| *CKM4* | 0.45 | 0.38 | 0.21 | 0.00 | 0.08 | 0.21 | 0.43 | 0.38 | 0.08 | 0.12 | 0.17 | 0.08 | **6.38** |
| *CKMQ1* | 0.25 | 0.26 | 0.38 | 0.26 | 0.26 | 0.39 | 0.24 | 0.18 | 0.08 | 0.26 | 0.31 | 0.08 | **4.04** |
| *CKMQ2* | 0.30 | 0.24 | 0.26 | 0.11 | 0.14 | 0.26 | 0.28 | 0.22 | 0.08 | 0.31 | 0.40 | 0.08 | **6.38** |
| *CKMQ3* | 0.10 | 0.11 | 0.28 | 0.70 | 0.68 | 0.28 | 0.09 | 0.07 | 0.08 | 0.11 | 0.14 | 0.08 | **2.60** |
| *CKMQ4* | 0.20 | 0.20 | 0.34 | 0.40 | 0.44 | 0.34 | 0.19 | 0.12 | 0.08 | 0.20 | 0.24 | 0.09 | **4.23** |
| ***Average*** | **0.31** | **0.28** | **0.22** | **0.17** | **0.20** | **0.22** | **0.20** | **0.18** | **0.06** | **0.31** | **0.35** | **0.06** | **6.26** |

It is also interesting to observe that the negative correlation between calcite and quartz, as well as between muscovite and kaolinite, seen in Figure 19, is also reflected in Table 6. This trade-off indicates that the underestimation of one mineral tends to be compensated by the overestimation of the other.

Despite the fact that the uncertainty modelling is still preliminary, the average prediction error of BSU (~6%) is significantly better than that from FCLS (>9%). A comparison between both methods in terms of prediction errors for each mineral is summarized in Figure 21.

For muscovite and kaolinite, both methods show the same general trend of slightly overestimating kaolinite and underestimating muscovite. However, FCLS perform much worse than BSU in calcite and quartz. FCLS often severely overestimate the abundance of quartz and calcite when the minerals are absent from the mixtures.

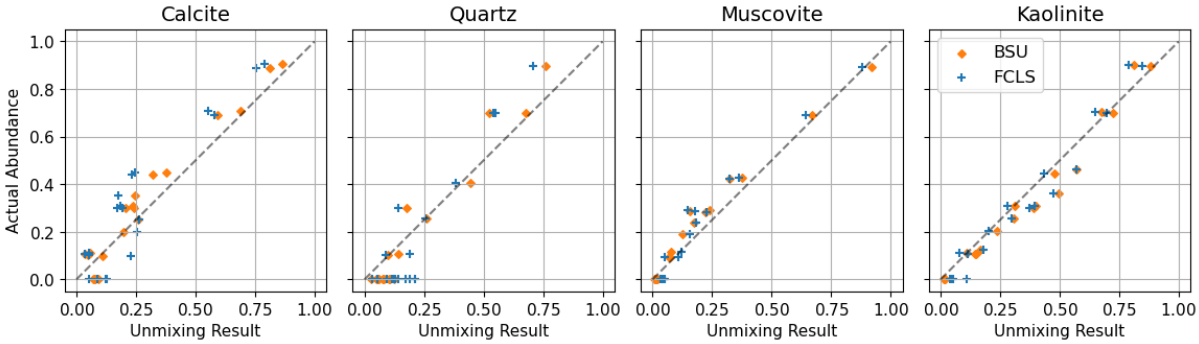


**Figure 21.** Comparison between BSU and FCLS results for every mineral. Each data points represents the prediction error of a single mixture powder sample. The closer the point to the diagonal line, the smaller the prediction error.

### 4.2.3. Effects of Different Spectral Processing Methods

The impact of hull removal, first derivative, and normalization on the results of BSU was evaluated. Figure 23 illustrates the effect of each spectral processing method on the endmember SSA spectra.

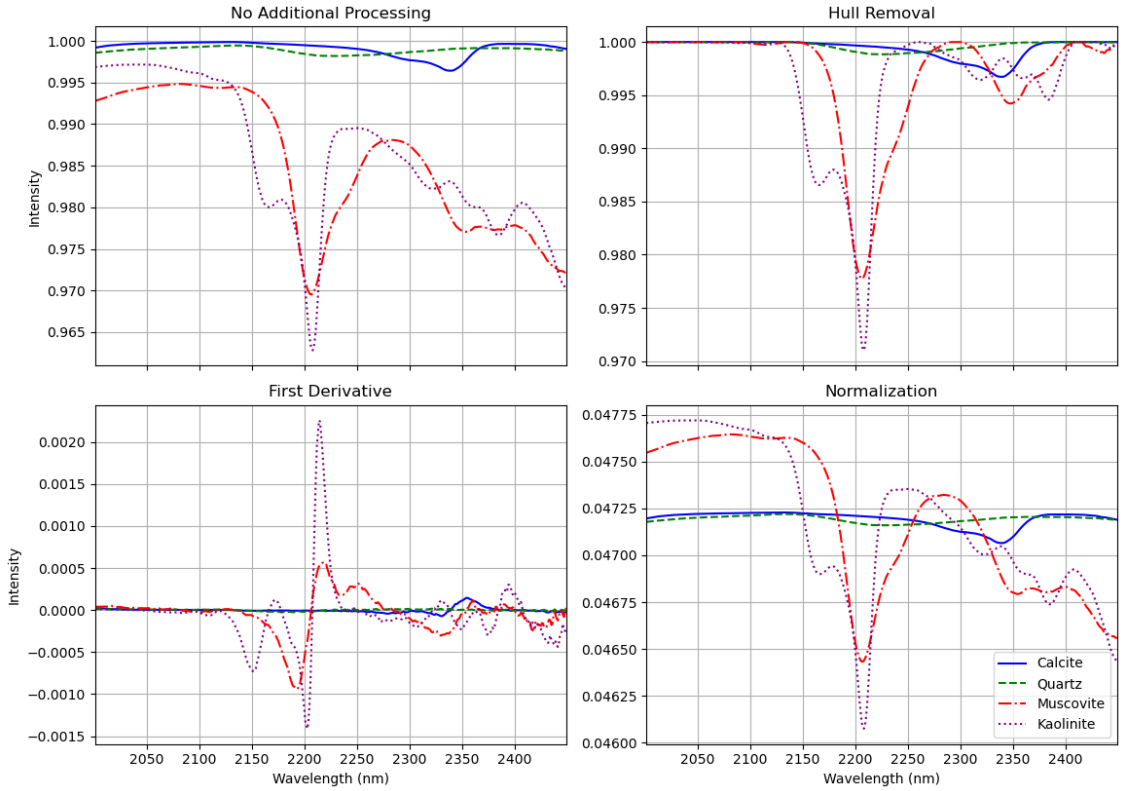


**Figure 22.** Different spectra processing results for endmember spectra

Table 7 summarizes the effects of these three spectral processing techniques on the average prediction error. Additional results from BSU using different spectral processing methods are provided in Appendix 3. Previously, these spectral processing were tested in spectral reconstruction and the results were reported in Table 5. It is interesting that while the first derivative showed the best performance in spectral

reconstruction, normalization demonstrates better results in this BSU analysis. This observation will be further discussed in Section 5.

**Table 7.** Summary table for the effect of the spectra processing to the accuracy of BSU represented by average prediction error.

| Average Prediction Error (%) | | | |
|---|---|---|---|
| *No Processing* | *Hull Removal* | *First Derivative* | *Normalization* |
| 6.26 | 6.84 | 10.84 | 6.05 |

For a fair comparison between the modelled spectra, all three processed spectra are transformed back to its original SSA spectra and compared with the actual SSA spectra in Figure 23. The same CKMQ 1 sample used for this example.

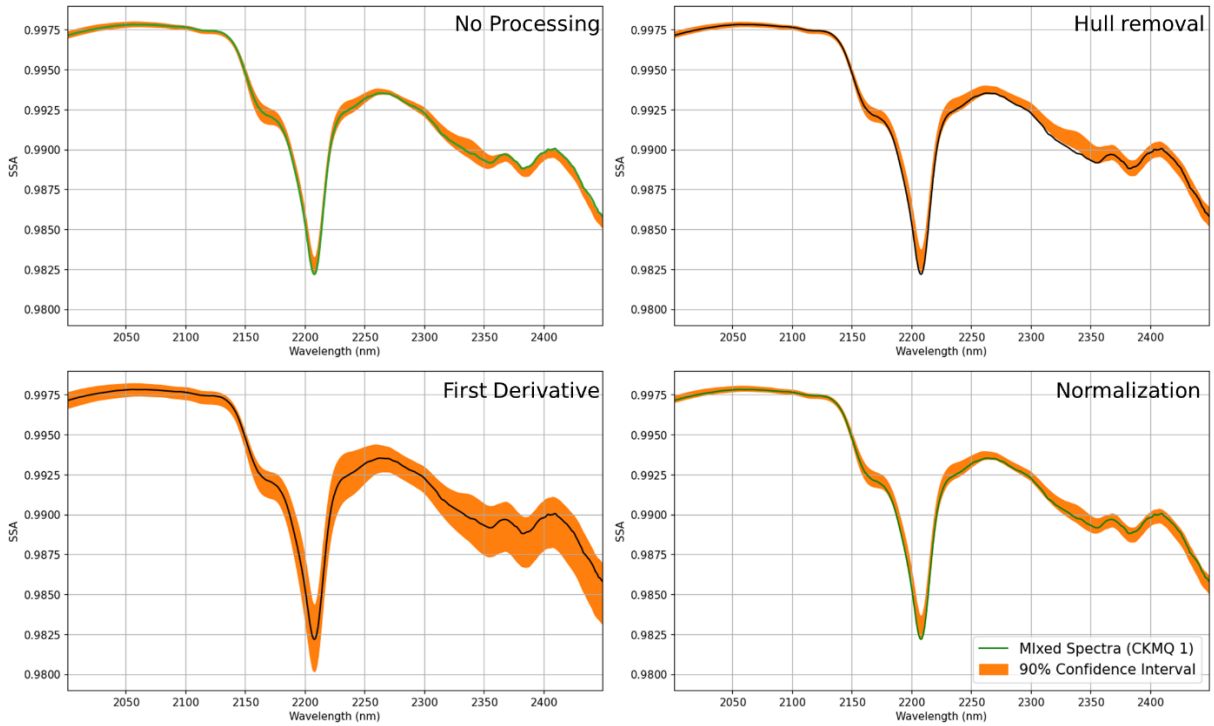


**Figure 23.** Comparison between the modelled spectra and the actual spectra of sample CKMQ 1 of different processing method. All of the processed spectra are transformed back to the original SSA for a fair comparison.

### 4.3. Core Sample Spectral Unmixing

Building upon the insights from previous experiments with the powder mixtures, where the H1 mixture model with normalization proved most effective, we applied this approach to perform spectral unmixing on the hyperspectral image of the core sample. The process began with extracting endmember spectra from the hyperspectral image, followed by applying both BSU and FCLS algorithms for unmixing.

Two approaches to spectral unmixing were conducted. The first approach, referred to as *average-pixel spectral unmixing*, involves averaging the spectra from every pixel before performing spectral unmixing on the resulting averaged spectrum using both FCLS and BSU to estimate the bulk mineralogy of the entire rock. While this approach does not provide detailed spatial information on mineral abundance, it is significantly faster because it reduces the entire image into a single spectrum. This makes it particularly

suitable for preliminary assessments of the spectral unmixing algorithm or when the primary objective is to determine the bulk mineral composition of the entire rock.

The second approach is *pixel-wise spectral unmixing*, where each spectrum in every single pixel is independently unmixed. This method provides fractional abundance information of minerals for each pixel, offering a detailed spatial distribution of mineral abundance across the rock surface. Thus, it yields richer data for analysing the mineral distribution within the rock surface.

For accuracy assessment, the prediction error is computed by comparing the unmixing result with QEMSCAN data. The QEMSCAN data used in this study only represent the bulk mineralogy of the whole rock. In average pixel unmixing, the abundance results can be directly compared with QEMSCAN data since both methods provide estimates of the bulk mineralogy of the rock sample. In pixel-wise spectral unmixing, the abundance results from each individual pixel are first averaged to derive the bulk mineralogy of the entire rock. This averaged result is then used to compute the prediction error, ensuring an accurate assessment of the overall mineral composition when compared with QEMSCAN data.

#### 4.3.1. Endmember Extraction

Endmember extraction using N-FINDR algorithm was performed after transforming the hyperspectral image spectra into SSA using H1 mixture model and then normalize the spectra. The results of the endmember extraction are presented in Figure 24.

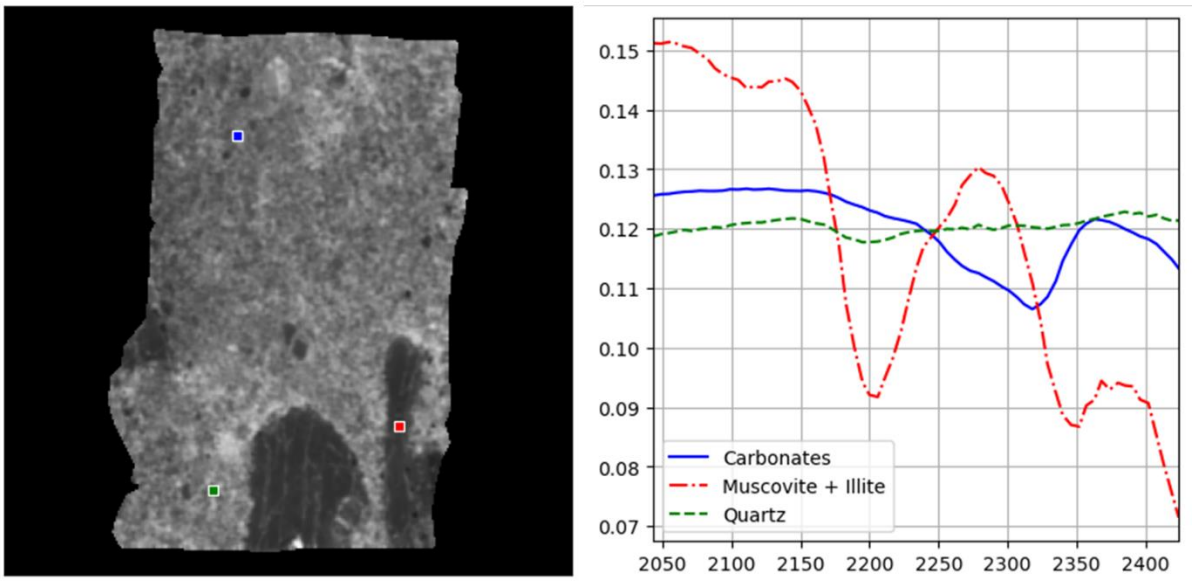


**Figure 24.** Endmember extraction result with N-FINDR for core sample. The small squares on the image represent the purest pixel positions.

#### 4.3.2. Average-Pixel Spectral Unmixing

In this approach we tested how the unmixing performs on a single average spectrum of the entire image. This approach may be considered when the interest is limited to obtain the bulk mineralogy abundance of the whole rock sample. This method significantly reduces the computation time for both FCLS and BSU, as it only operates on a single spectrum. Therefore, we will also use this data to tune for the optimal step size which will also be used for the pixel-wise spectral unmixing. The average spectrum of the whole image is shown in Figure 25 along with the endmember spectra for comparison.

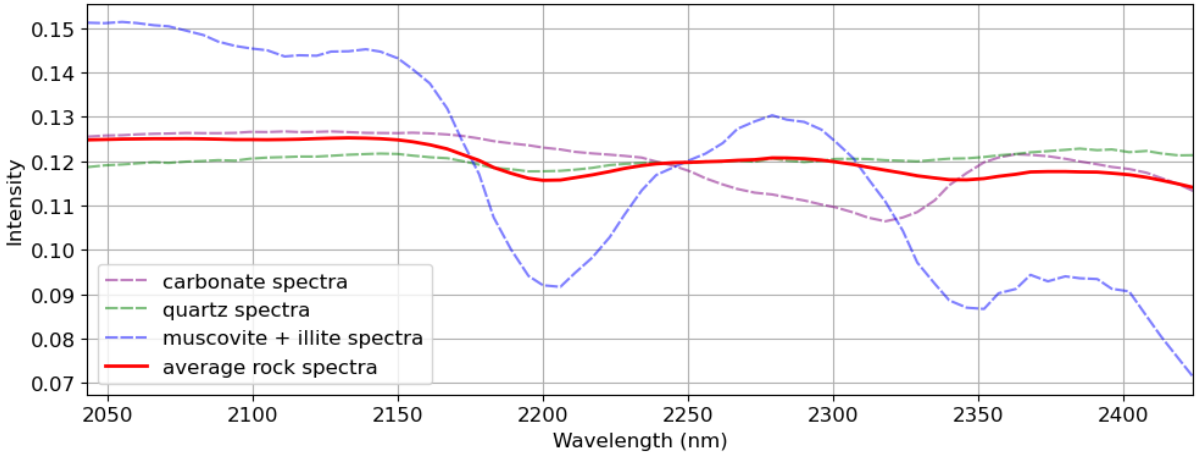


**Figure 25.** Average rock spectra and endmember spectra of the core sample.

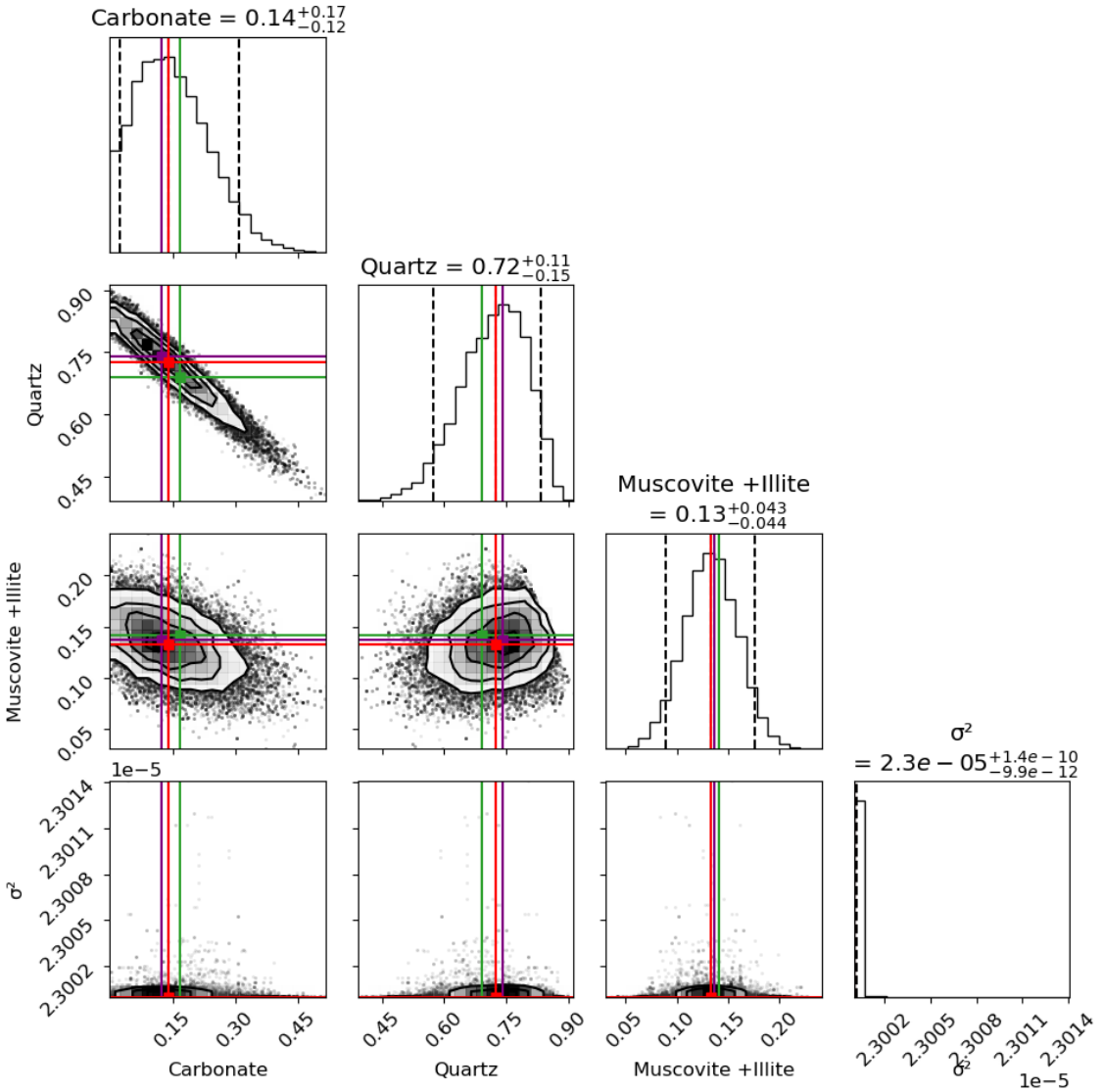


**Figure 26.** Corner plot for the posterior distribution of the rock sample average spectrum. The red line represents the expected value of BSU result (median) with the stripped lines in histograms represent its 90% confidence interval, green line represents the actual values, and purple line represent FCLS results for comparison.

Using the same assumption of 6% uncertainty as in the powder mixtures, we obtain $\varphi = 2.3 \times 10^{-5}$ for the present sample. Since in the next step we will conduct the pixel-wise unmixing which require much computation time, here we consider reducing the number of iterations into $50{,}000$ iterations. We set the step size of $t_1 = 100$ and $t_2 = 0.5$ with a burn-in period set to $5{,}000$. We obtained acceptance ratios of $54.81\%$ for $\mathbf{a}$, and $46.29\%$ for $\sigma^2$. The posterior distribution result is visualized in Figure 26. Since in the rock sample we are dealing with three mineral groups, we can visualize the full posterior distribution of the abundance of the mineral abundance in a ternary diagram (Figure 27).

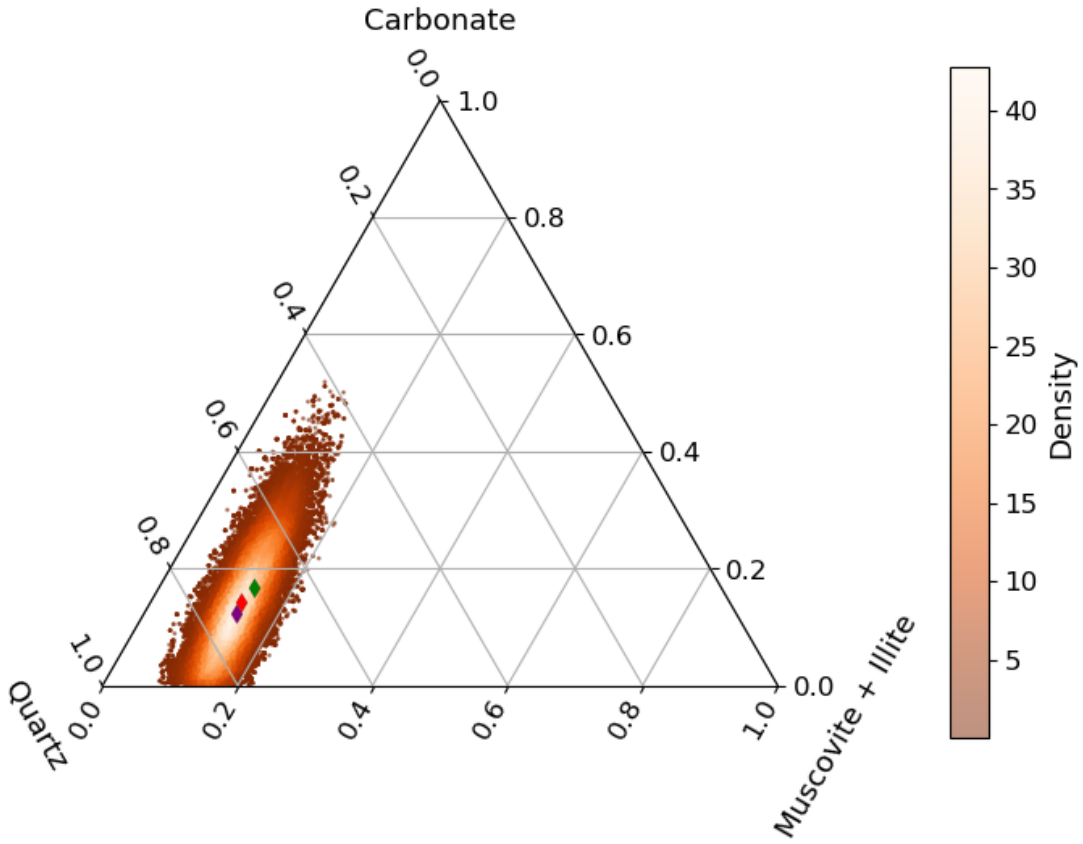


**Figure 27.** Posterior distribution of the mineral abundances. Red markers represent the expected values (median) of BSU result, purple markers represent the FLCS result, and green marker the abundance values obtained from QEMSCAN which considered as the actual values.

Here, we observe much better results compared to the powder mixture spectral unmixing in Section 4.2.2, where all the actual values lie within the 90% confidence interval of the estimates. This will be discussed further in Section 5.2.2. Overall, we obtained a prediction error of $2.51\%$ for BSU, compared to $3.88\%$ for FCLS.

#### 4.3.3. Pixel-Wise Spectral Unmixing

As briefly mentioned in Section 4.1, the computing time required to perform BSU is significantly greater than that needed for FCLS. This is especially true when considering hyperspectral unmixing on an image dataset, which in this case contains $90{,}000$ pixels. Careful consideration is needed to reduce computing time. For this, we make use of the tuned valued from the average spectrum spectral unmixing in the previous chapter and obtained acceptance ratios of $53.78\%$ for $\boldsymbol{a}$, and $19.28\%$ for $\sigma^2$.

The results of BSU are depicted in Figure 28, where alongside the mineral abundance estimates, confidence interval images are also provided. In BSU, the variance $\sigma^2$ is modelled, and the corresponding results are presented in Figure 29.

For comparison, the result of FCLS spectral unmixing are presented in Figure 30. In terms of prediction accuracy compared to QEMSCAN data, FCLS and BSU show very similar results, with a prediction error of 3.691% for FCLS and 1.865% for BSU. Comparison between the mineral abundance results is summarized in Table 8.

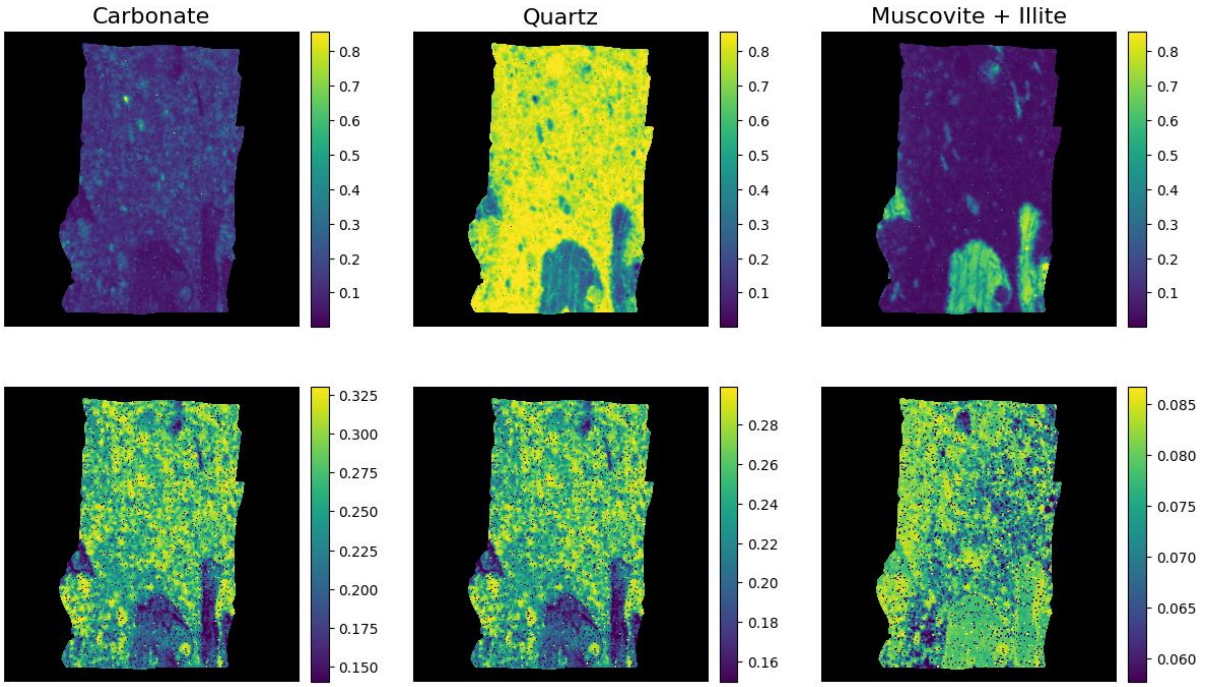


**Figure 28.** BSU result of the core sample. Top row shows the abundances of each endmember mineral, bottom row shows the confidence intervals.

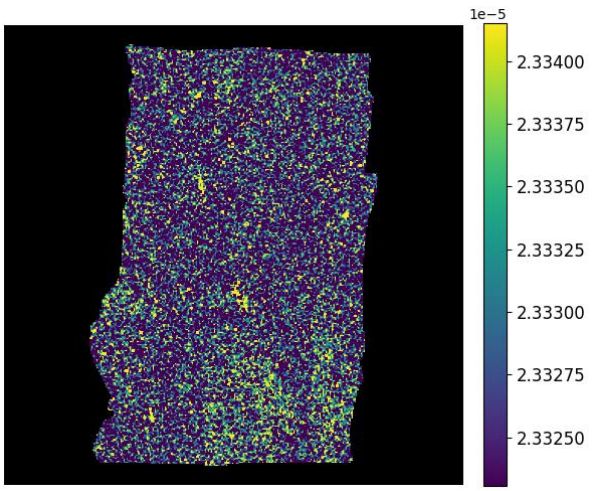


**Figure 29.** The median (P50) of $\sigma^2$ of for every pixel in the core sample

**Table 8.** Comparison on mineral abundance results of QEMSCAN data, FCLS spectral unmixing, and BSU.

| **Method** | **Minerals (%)** | | | ***Prediction Error (%)*** |
|---|---|---|---|---|
| | *Carbonate* | *Quartz* | *Muscovite + Illite* | |
| *QEMSCAN* | 16.772 | 69.086 | 14.140 | - |
| *FCLS* | 12.524 | 73.838 | 13.637 | 3.691 |
| *BSU* | 14.702 | 71.503 | 13.581 | 1.865 |

Using the same ITC Geospatial Computing Platform (Girgin, 2021), the computation time for FCLS is 83 seconds using a single thread. In contrast, the computation for our BSU implementation is significantly more demanding and takes 6.8 hours using 16 threads.

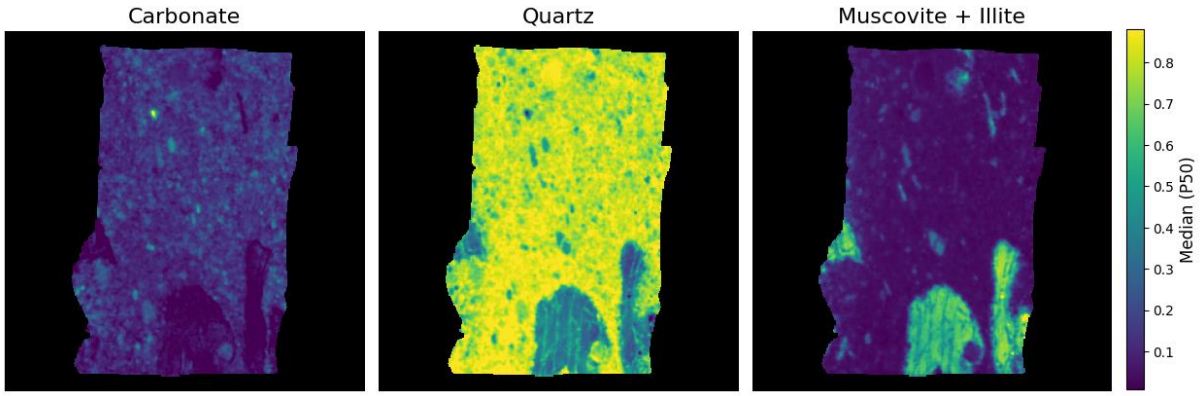


**Figure 30.** FCLS spectral unmixing results of the core sample.

# 5. DISCUSSION

## 5.1. Methods Evaluation

### 5.1.1. Mixture Model

The mixture model based on the Hapke Model outperformed LMM for the powdered mineral mixtures tested in this study. This outcome was expected, since the non-linear behaviour of intimate mixtures is well-documented in prior research (Harris & M. Grindrod, 2018; Howari et al., 2018; Lapotre et al., 2017; Nash & Conel, 1974). The H1 and H2 implementation of the Hapke Model, which assumes isotropic and anisotropic single scattering respectively, produced comparable SSA spectra, as depicted in Figure 16. The spectral reconstruction results were also comparable with the reconstruction errors of $1.80\%$ for H1 and $1.81\%$ for H2.

Figure 31 illustrates the H1 and H2 functions at the specified viewing angle used in this research ($i = 45°; e = 0°$). Both functions produce nearly identical results, particularly for high albedo minerals, which are predominant in this study. Figure 17 demonstrate that the reflectance value of the pure minerals was already very high, especially for quartz and calcite.

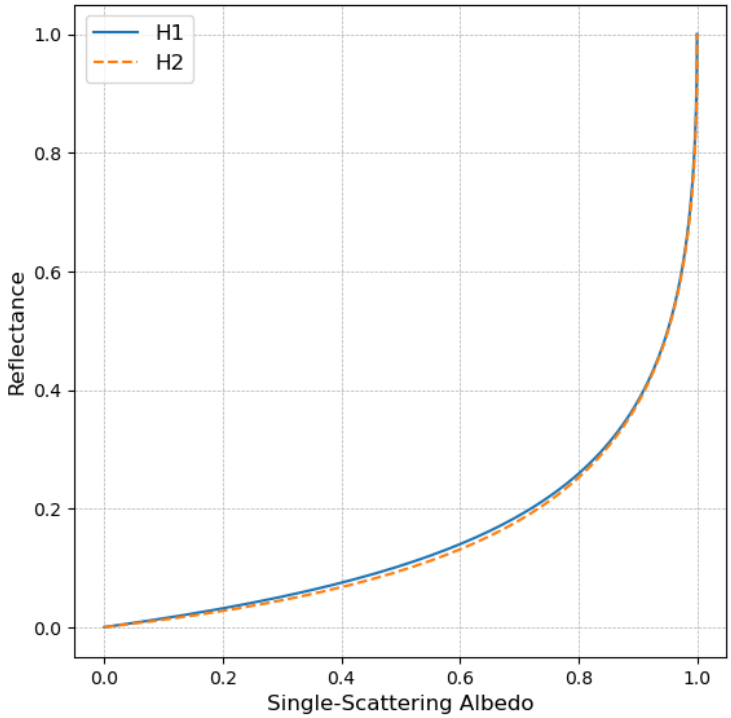


**Figure 31.** Relative bidirectional reflectance as a function of SSA for H1 and H2 mixture model.

The main difference between H1 and H2 (as discussed in Section 3.1.2) lies in the constant $b$ and $c$ of phase function $P(g)$ in Eq. (6) which describe the scattering behaviour of the particles. In H1, assuming isotropic scattering, $b = c = 0$ hence P(g)=1, while in H2, assuming anisotropic scattering, $b = -0.4$, and $c = 0.25$ which is derived experimentally for mafic minerals by Mustard & Pieters (1989). Additionally, H1 uses a less precise approximation of the Chandrasekhar function (Eq. (7)) for simplicity and analytical solvability, while H2 employs a more precise approximation (Eq. (8)). Despite these differences, the results of both models are similar, as shown in Figure 31.

It is important to clarify that although H1 performed slightly better than H2, this does not necessarily mean that the scattering behaviour of the powder mixtures is isotropic. As shown in the spectral reconstruction of H1, an error of up to 4.88% can still be observed (Table 4). This indicates that the scattering is not truly isotropic; rather, the simplifications used in H2 do not fully capture the true anisotropic scattering behaviour. To further improve the model, a more rigorous treatment of the Hapke Model is needed. For example, $b$ and $c$ could be derived experimentally in the laboratory by measuring the samples at different viewing geometries to solve for SSA, $b$, and $c$ simultaneously for this specific sample, as done by (Mustard & Pieters, 1989). Additionally, including $b$ and $c$ as model parameters in BSU could also be considered.

To determine the influence of a particular mineral on the model error, correlation coefficients between the reconstruction error of each mixture model and the abundance of each mineral were calculated, as shown in Table 9. Quartz and calcite abundance show a high positive correlation with reconstruction error from LMM. At the moment, we do not have a sound explanation for this observation.

Muscovite abundance shows the highest positive correlation with reconstruction error in both H1 and H2 cases, with a notably higher correlation in H1. This high correlation is likely due to muscovite particles in the mixture violating the isotropic assumption of the model, even more so compared to other mineral in the mixtures. According to Hapke (2012), scattering from large, irregular particles tends to be more isotropic compared to smooth particles. Muscovite, with its sheet-like crystal structure, is likely to have higher surface area of smooth surfaces compared to the more prismatic calcite and quartz crystal. There is no significant correlation of reconstruction error with kaolinite abundance for H1. While kaolinite crystal is also generally platy in shape, it often forms an aggregate of particles with arbitrary shapes. And the interaction between light and the surface essentially occurs at the particle level, not necessarily the crystal level.

**Table 9.** Correlation coefficient between reconstruction error of each mixture models with mineral abundances.

| | **Correlation Coefficient** | | | |
|---|---|---|---|---|
| ***Mixture Model*** | ***Calcite abundance*** | ***Quartz abundance*** | ***Muscovite abundance*** | ***Kaolinite abundance*** |
| *LMM* | 0.53 | 0.64 | -0.54 | -0.76 |
| *H1 (isotropic)* | -0.17 | 0.17 | 0.61 | -0.01 |
| *H2 (anisotropic)* | -0.07 | 0.00 | 0.39 | 0.07 |

It is difficult to determine which model performs better between H1 and H2. Although H1 has a slightly smaller overall reconstruction error, the difference is insignificant. The correlation analysis suggests that H2 can explain the scattering behaviour of muscovite better, albeit still imperfectly, and performs comparably for other minerals. Additionally, the test was conducted on pure minerals with very high albedo, making it challenging to clearly observe the differences between the two mixture models. Despite these factors, we decided to proceed with H1 mixture model for the remainder of this research. The significantly faster implementation of H1 is a crucial factor in this decision, as computation time becomes increasingly important when dealing with image data later in this study.

## 5.2. Spectral Unmixing

### 5.2.1. Uncertainties

It is crucial to first discuss the various types of uncertainties inherent in the spectral unmixing process. We categorized these uncertainties into three main groups: measurement-related uncertainties, modelling-related uncertainties, and nature-related uncertainties.

Measurement-related uncertainties typically involve two primary aspects. First, there is ambient noise and other instrument-related uncertainties. Second, there are uncertainties related to experimental variability, such as sampling preparations. For instance, Figure 32 below illustrates the measurement data of a single powder mixture sample (Sample CM 1), showing ten spectra taken from the same powder sample but at slightly different measurement points. Instrument noise is noticeable at longer wavelengths of the spectra($\sim 2350\ nm$ to $2450\ nm$). Additionally, the slight variability in albedo among the spectra may be attributed to experimental factors such as uneven thickness of the powder mixture, varying grain size distribution of the minerals, and other factors related to sample preparation. The spectra used for subsequent analysis are typically the mean of these 10 measurements. While averaging reduces variability in the data, it does not necessarily eliminate the underlying uncertainties associated with the data itself.

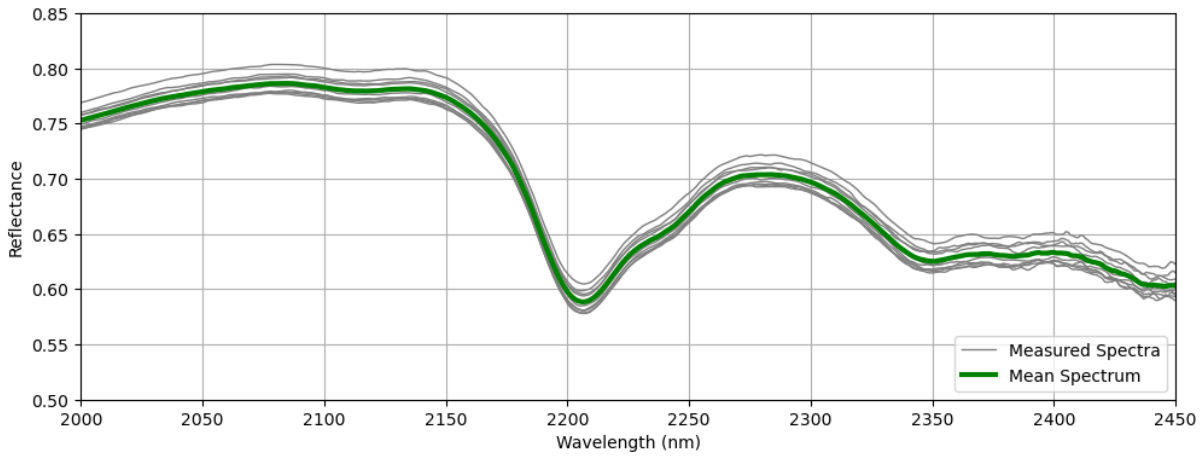


**Figure 32.** ten measurement points of sample CM 1 and its mean spectrum.

Modelling-related uncertainties refer to those associated with the mixing model and endmember extraction processes. No mixing model can perfectly replicate the actual spectral mixing process. In the case of the Hapke Model (H1 and H2) used in this research, simplifications and assumptions are made that contribute to uncertainties in the final results. As detailed in Section 3.1.2, these assumptions include neglecting backscattering, using analytical approximations of the Chandrasekhar function for multiple scattering effects, which reported to deviate up to 6% from actual values (Mustard & Pieters, 1989), and assuming specific scattering behaviours of particles (either isotropic or anisotropic). These assumptions collectively contribute to the overall uncertainty of the mixing model.

The uncertainties associated with the model are partly illustrated in Figure 18, which shows the reconstruction error between modelled spectra and actual observed spectra. This error quantifies how well the model's assumptions and simplifications align with real-world spectral data, highlighting the inherent uncertainties in the modelling approach.

There are also uncertainties related to endmember extraction. Extracted endmembers may not be 100% pure, affecting the accuracy of the unmixing results. For example, in Figure 24, the quartz spectra exhibit a

weak feature around 2200 nm, suggesting that the extracted quartz endmember is not entirely pure, which can influence the overall accuracy.

Finally, uncertainties related to the nature of the rocks and minerals being observed also play a crucial role. Not every mineral exhibit exactly the same spectra. Variations in muscovite within different rock fragments in the core sample, for instance, may result in slight spectral differences due to variations in grain size and chemical composition. This variability among spectra of the same mineral species is known as *intraclass spectral variability* and can significantly impact the outcomes of spectral unmixing.

In this research, all these uncertainties are assumed to be independent and identically distributed, as discussed in Section 3.5.2, and are represented by the overall variance ($\sigma^2$). We have not yet explicitly considered the contribution of each type of uncertainty to our prior probability. Instead, we consider a conservative estimate of modelling error with H1 up to $6\%$ as reported by (Mustard & Pieters, 1989). We translate this $6\%$ error as the lower limit for the prior of our variance by using the hyperparameter $\varphi$ as explained in Section 3.5.3. This means that the initial assessment of the uncertainty that is conducted in this research is still rudimentary and may be improved.

BSU aims to model $\sigma^2$ as part of the inference problem and automatically performs a global uncertainty propagation into the final prediction of mineral abundance. Consequently, BSU produces mineral abundance estimates in the form of probability distributions, typically represented by their expected values (median) and 90% confidence intervals ($5^{th}$ and $95^{th}$ percentiles). These distributions provide a clearer understanding of the global uncertainty associated with each estimated mineral abundance, incorporating variability from measurement, methodological, and natural sources.

#### 5.2.2. Computer-Generated Mixture and Powder Mixture Experiment

We began the experiment with BSU using computer-generated mixtures to simulate ideal conditions. This initial stage is crucial for verifying the behaviour of the MCMC algorithm (see Section 3.5), as implementing MCMC can be cumbersome. There are many steps in the process that are vulnerable to implementation errors that can be hard to detect in a more complex setup. Under these ideal conditions, we showed that BSU performs well, with results closely matching the actual values. Moreover, BSU slightly outperforms FCLS in terms of median error, although the difference is not considerable.

Note that for the computer-generated test, we used the LMM to generate the mixtures. In principle Eq. (1) which describes LMM and Eq. (2) which describes H1 and H2 have exactly the same forms and only differs in the domain of the spectra. Therefore, for the purpose of testing the performance of BSU with computer-generated mixture, the choice of any of the three mixing model is arbitrary since any option will produce similar results.

The BSU algorithm implemented in this study was able to estimate not only the mineral abundance, but also the $\sigma^2$(i.e. variance of the added gaussian mixture) which is something that FCLS spectral unmixing cannot provide. It is important to note that in computer-generated mixtures, the various sources of uncertainties described in previous section does not exist. The only uncertainty is the added Gaussian noise which make the unmixing problem to be relatively simple. On the real powder mixture however, other source of uncertainty such as noise, experimental variability, and mixing model uncertainty exist which complicated the problem.

In this research we are approaching the problem to model the uncertainty in a relatively simplistic way. First, we represent the uncertainty in the likelihood function with a single variance ($\sigma^2$) value (see Section

3.5.2). Second, we represent our state of ignorance by choosing a weakly informative prior of Half-Cauchy distribution (see Section 3.5.3). Half-Cauchy is a long-tailed distribution with the highest probability in smaller value and lower probability for the higher value. Choosing this prior is equivalent with stating that we do not know much about the possible $\sigma^2$ value, but it must be positive, and it is likely to be a small value. This means that we are largely rely on the observation (input mixed spectra and the pure endmembers spectra) to find $\sigma^2$ which can best describe our observation.

This strategy, while effective in a simple case of computer-generated mixtures, is less effective in real powder mixtures with more complex uncertainties, as shown in Section 4.2.2, especially for muscovite and kaolinite. As explained by the correlation observed in Table 9, the presence of muscovite seems to be responsible for higher errors in the mixture modelling. As shown in the corner plot of the powder mixture in Figure 19, muscovite and kaolinite have a strong negative correlation. Thus, errors in muscovite estimation also impact kaolinite accuracy and vice versa.

Hapke's model brings a complex uncertainty which are sensitive to the albedo, and its influence is different for every endmember. It is clear that a single variance ($\sigma^2$) value cannot adequately capture these diverse uncertainties. Hence our main suggestion is to use a full covariance matrix in likelihood function the likelihood function Eq. (13) instead of a single variance. A covariance matrix captures a more complex representation of uncertainties, allowing the algorithm to model for different levels of uncertainties and the relationships between them. While this approach increases computation time, it is known to provide more realistic model outputs (Gregory, 2005). In contrast, using a single variance value for all parameters, though computationally simpler, can be unrealistic and/or mask the true nature of the different uncertainty source.

Another approach is to reconsider how to best formulate the mixture model. Hapke's model includes many unknown variables, which are simplified through assumptions in this research. For instance, variables such as $b$ and $c$ constants in the phase function of Eq. (6) could also be inferred as part of the hierarchical MCMC model. This would be the most natural way to incorporate the uncertainty of the surface scattering behaviour into the final unmixing result. Other research, such as that of Lapotre et al. (2017), also utilizes different forms of the Hapke Model that include particle size as a variable and consider it as a model parameter in the MCMC formulation. Note that this type of approach requires solving the Hapke Model (which requires optimization) inside the MCMC iteration and might significantly increase computation time.

Above all, understanding the inherent uncertainties in spectral unmixing, as detailed in Section 5.2.1, is crucial for developing improved modelling strategies. This knowledge might help to add more information into the prior by adjusting the hyperparameter $\varphi$, for example (see Section 3.5.3 Eq. (15)) which described the lower limit of the possible $\sigma^2$ value, or even changing the entire prior to a distribution that best describes our updated state of knowledge. Indeed, incorporating prior knowledge to the model is one of the main advantages of Bayesian approach and it still underutilized in this research, since we only used weakly informative priors.

We have attributed the errors in BSU estimates to the uncertainties related to the mixture model, and how BSU, when relying only on data, cannot fully capture uncertainties related to the mixture model. We also have discussed possible ways to address this issue. However, it is also important to note that FCLS performed much worse on the powdered mixtures compared to BSU. Since the increase in prediction error is much higher for FCLS than for BSU, the mixture model problem might not be solely responsible for the errors in FCLS spectral unmixing.

A significant portion of the error in FCLS results appears to come from calcite and quartz, where FCLS severely overestimates their abundance, especially when these minerals are not present in the mixture (Figure 21). The spectra of calcite and quartz are highly similar, making it harder for FCLS to differentiate between them solely based on spectral signatures. Because FCLS aims to minimize the absolute error between the observed spectra and the linear combination of endmember spectra, it tends to fit the observations closely, even if this means assigning some abundance to minerals that are not actually present. This phenomenon is known as overfitting. On the other hand, BSU methods, which explicitly model the uncertainty, are generally more effective in handling such scenarios.

To mitigate the overfitting issue in FCLS, one potential approach is to introduce a sparsity term into the unmixing formulation. This sparsity term penalizes the assignment of non-zero abundances to components that are not necessary to explain the observed spectra. By encouraging solutions with fewer active components, such as minerals with non-zero abundances, sparsity regularization helps to improve the accuracy of unmixing results and reduce the tendency of FCLS to overestimate abundances.

#### 5.2.3. Spectral Processing Effects

As shown in Figure 29, even controlled laboratory-made powder samples exhibit variability in the albedo of the spectra. This variability generally increases in natural surfaces, such as rock samples, and can significantly impact the accuracy of spectral unmixing. Therefore, it is desirable to mitigate or reduce this variability before conducting spectral unmixing with spectral processing methods such as hull removal, first derivative, and normalization.

Under perfect conditions, the real spectra, their first-derivative spectra, and normalized spectra should yield exactly the same result for spectral reconstruction. While for hull removal spectra, slight deviations are expected since hull removal essentially breaks the linearity assumption. In reality, due to the aforementioned variability, these spectral processing methods may improve the result of spectral reconstruction, as observed in our experiment (Table 5).

On the other hand, we also observed that the convex hull of the spectra carries relevant information for spectral unmixing. This is evident from our experiment with computer-generated mixtures, where extreme Gaussian noise was added to the spectra to the point where the absorption features were no longer clear (Figure 12, right). Despite this, both FCLS and BSU were still able to produce good solutions. The main reason for this success is that the shape of the convex hull remains visible in the presence of extreme Gaussian noise, providing a strong constraint on the possible solutions and guiding the algorithms to accurate results even under significant noise conditions.

First derivative and hull removal, while reducing variability in the spectra, also remove the convex hull, which reduces the amount of information carried by the data. Normalization is the only processing method that can reduce the variability of the albedo while preserving the original shape of the spectra. This might be the reason why normalization yielded the best results in terms of prediction error for spectral unmixing (Table 7). It is important to note that there are many different approaches to normalization, but the one that achieves this effectively is normalization by Euclidean distance, as explained in Section 3.2.

As visible in Figure 23, the first derivative amplifies the uncertainty, resulting in much wider confidence intervals for the modelled spectra. This is because the first derivative amplifies the noise of the spectra, as also visible in the transformed endmember spectra in Figure 22, especially at higher wavelengths. To

overcome this, we suggest that instead of calculating the first derivative directly from the spectra, a smoothing method should be applied first. Methods such as the Savitzky-Golay First Derivative (Rinnan et al., 2009) should be preferred.

#### 5.2.4. Core Sample

Applying the N-FINDR algorithm to the entire image resulted in the selection of edge pixels as pure quartz pixels. Edge pixels are often unreliable due to surface irregularities or background contamination. To mitigate this issue, we applied N-FINDR to a buffered subset of the image, excluding edge pixels.

The common approach in conducting spectral unmixing on hyperspectral images is pixel-wise unmixing, where each pixel is unmixed independently. For BSU, this results in a large dataset, with a single posterior distribution for every pixel. This presents a challenge in visualizing the posterior distributions; for a 300 by 300-pixel image, we would have 90,000 different posterior distributions. An alternative approach is average-pixel spectral unmixing, where we first average the spectra of all the pixels, and then unmix this single averaged spectrum. Since we assume linearity (after transforming the data to SSA), this approach is valid. In this research, we performed both approaches: pixel-wise spectral unmixing for detailed analysis and average-pixel spectral unmixing for an overview of the full posterior distribution.

Interestingly, compared to the powder mixture samples, the spectral unmixing results for the rock sample are much better. We suspect the reason is related to muscovite. The rock sample contains only a small amount of muscovite (~3%), with illite being the dominant mineral in the muscovite+illite group (Table 2). Additionally, by grouping muscovite and illite together, we avoid the apparent trade-off between the two minerals as observed in the powder mixture samples.

These outcomes indicate that the methodology developed for powdered mixtures is applicable and generalizes effectively to the core samples tested in this study. However, the applicability of this approach may still vary depending on the grain sizes and texture of the rock sample. Therefore, generalizing these findings to other rock samples should be approached cautiously, as it could potentially lead to inaccurate estimates of mineral abundance.

For pixel-wise spectral unmixing, BSU yielded very good results in terms of prediction error, which is less than 2%, making it suitable for most practical applications. This result shows that our proposed methods, despite their simplifications, can still provide very good accuracy followed by a reliable uncertainty estimate.

We have yet to fully explore the full results of the pixel-wise BSU. As a preliminary inspection, we find it interesting that the pixels with the highest variance (i.e., global uncertainty) coincide with rock fragments among the sandstone. We suspect this is due to either higher endmember variability of the minerals in the rock fragments or the presence of more accessory minerals in the rock fragments.

In Figure 33, we selected three standout pixels from three small fragments in the sandstone to inspect their spectra. While it is difficult to determine the cause just by looking at the spectra, we might suspect that endmember variability is the reason. For example, the red spectrum in Figure 33 shows the deepest Al-OH feature shift to a lower wavelength compared to the selected endmember. Further investigation is needed to provide a stronger explanation for this observation.

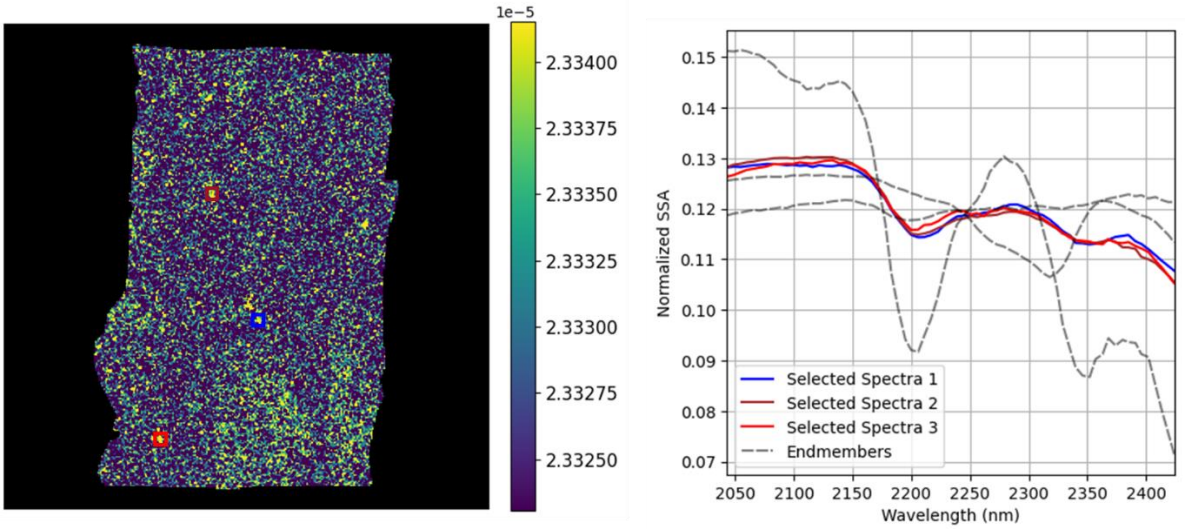


**Figure 33.** Variance image of rock sample (left) and the selected spectra (right) of fragments with high variances.

### 5.3. Relevant Findings & Practical Implications

In this section, we summarize key findings from our study that might have some practical relevance for the application of spectral unmixing to rock samples hyperspectral images. We found that the simplified implementation of Hapke's Model, denoted as H1 in this research, significantly enhances the accuracy of spectral unmixing compared to LMM, while still maintaining computational efficiency.

Since we find that convex hull provides a useful information for spectral unmixing, we do not recommend the use of first derivative and hull removal unless there are compelling reasons to do so. Instead, we recommend the use of normalization since it gives minimal changes to the original spectra.

To further clarify our argument, we conducted additional tests of spectral unmixing on the powder mineral samples using LMM and H1 models with and without normalization. The results are summarized in Table 10.

**Table 10.** Comparison of spectral unmixing average prediction error between normalized and unnormalized spectra with LMM and H1 mixture model.

| **Unmixing Methods** | **LMM** | | **H1** | |
|---|---|---|---|---|
| | *No Processing* | *Normalization* | *No Processing* | *Normalization* |
| FCLS | 15.37% | 14.14% | 9.39% | 10.53% |
| BSU | 15.39% | 15.20% | 6.26% | 5.81% |

During our unmixing trials on the rock samples, we found that the choice of endmember spectra is crucial to the accuracy of the unmixing. Since N-FINDR assumes linearity in the data, it produces much better results when the input is SSA derived from the Hapke Model (we tested for isotropic model H1 in this case). When we tested N-FINDR with reflectance spectra, the results for the endmember spectra were unrealistic. N-FINDR can also be sensitive to noise and albedo variability, hence we recommend normalizing the data before applying the algorithm.

In our assessment of spectral unmixing methods, we found that BSU generally outperforms FCLS in terms of prediction error. Most importantly, BSU predictions come with their associated uncertainties. For example, if we ask about the bulk mineralogy of the sandstone tested in this research, BSU provides a range of possible values, offering more information for decision-making compared to FCLS, which only provides a best estimate.

However, considering computational efficiency and ease of implementation, FCLS remains recommended for fast, off-the-shelf spectral unmixing. For more in-depth analyses, BSU offers a much richer set of results, providing more diagnostic insights into the problem and a more powerful platform for a comprehensive assessment of uncertainties (e.g. including uncertainties in the spectral libraries, correlations in the data and model parameters, model non-linearities).

BSU also offers the option to include prior information about the rock sample. For a geologist, having a reasonable understanding of the rock to be analysed is common. This information can be incorporated into BSU by modifying the prior probability for abundance, allowing for more informed and accurate unmixing results.

# 6. LIMITATIONS AND FUTURE RECOMENDATIONS

There are many uncertainties related to the spectral unmixing process including instrument noise, experimental setup variations, mixture model inaccuracies, challenges in extracting accurate endmembers, and the natural endmember variability. In this study, we use a relatively simple method to estimate the uncertainty and relied mostly on the observation to model them using the BSU algorithm. However, our findings suggest that this approach may not provide an optimal uncertainty model, which represents a primary limitation of our research.

We suggest dedicating more effort to understanding and improving current knowledge of each uncertainty involved in the spectral unmixing process and how these uncertainties propagate to the final result. This deeper understanding will allow to formulate better approaches for appropriately modelling uncertainty related to the spectral unmixing which include in incorporating a better prior probability for the BSU.

Building upon the BSU algorithm developed in this study, we suggest future research to improve by replacing the scalar variance to a covariance matrix in the likelihood formulation (Eq. (13)). A covariance matrix captures a more complex representation of uncertainties, allowing the algorithm to model for different levels of uncertainty and the relationships between them, which is essential for capturing the uncertainties arising from mixing model inaccuracies unique to each endmember.

Furthermore, integrating additional Hapke parameters, such as constants $b$ and $c$ of the phase function, or grain size into the MCMC sampling process could provide a more comprehensive uncertainty model and reduce prediction error. This step makes the uncertainty modelling related to the mixture model more explicit by directly models parameters that influence scattering behaviour of particles.

While it is crucial to model uncertainties accurately, the goal of spectral unmixing is to achieve more precise and reliable results. Given the sensitivity of these outcomes to the quality of endmember spectra, future research may invest more efforts in advancing techniques for extracting and validating endmembers.

It is important to also acknowledge that QEMSCAN results, while valuable, are subject to their own uncertainties and inaccuracies. Nevertheless, exploring spectral unmixing results using full-image QEMSCAN data still could offer further insight and more comprehensive spectral unmixing result evaluation compared to the bulk mineralogy data QEMSCAN used in this research.

Finally, a limitation of BSU is its high computational cost. In this study, we implemented our own version of the MCMC algorithm for BSU. Even though a substantial amount of effort was made to optimize the computation time, our implementation remains relatively rudimentary, given that refining computational efficiency was not our primary focus. Therefore, we recommend future research to adopt or develop an optimized MCMC sampler for more computational efficiency. Variational Inference, Invertible Neural Networks (a machine learning technique), Approximate Bayes Computation and more sophisticated algorithmic implementations of BSU are all sound options to improve the efficiency of the proposed approach (Brooks et al., 2011; X. Zhang & Curtis, 2021). We recommend exploring these alternatives in the future.

# 7. CONCLUSION

In this research, we developed and evaluated a hyperspectral unmixing strategy for sandstone core samples and assessed its associated uncertainties. We began by experimenting with computer-generated mixtures and mineral powder mixtures to build our knowledge, which we then applied to the actual rock sample.

We found that the proposed BSU approach effectively predicted both the abundance and uncertainty in computer-generated mixtures (RQ 1.a). The results of both FCLS and BSU were comparable and in good agreement with the actual values of the computer-generated mixtures, with no significant difference in prediction error (RQ 1.b). We also find that both FLCS and BSU are robust against random gaussian noise However, BSU provided much richer information compared to FCLS by estimating the uncertainty of each parameter.

Hapke models significantly outperformed LMM in modelling the powder mixtures of calcite, quartz, muscovite, and kaolinite. Despite this, Hapke models H1 and H2 were still not able to perfectly model the data, with average reconstruction error of 1.8% and 1.81%, respectively. This insignificant difference makes it difficult to conclusively determine which assumption of the Hapke model works better for the powder mixtures (RQ 2.a). Nevertheless, H1 was chosen for the next step due to its computational advantage over H2.

For powder mixtures, our implementation of BSU was less effective compared to its performance in computer-generated mixtures. The BSU implementation in this research was unable to provide an optimal uncertainty model for the powdered mineral mixture, especially for muscovite and kaolinite, where the true values often fell outside the 90% confidence interval (RQ 2.b). However, in terms of prediction error, BSU achieved 6.26%, which is much better compared to FCLS spectral unmixing at 9.73% (RQ 2.c).

Normalization provided the best improvement for BSU results by reducing the average prediction error (RQ 2.d). We believe that the shape of the convex hull contains valuable information for spectral unmixing. Therefore, we do not recommend using spectral processing methods that remove this information, such as first derivative and hull removal.

Based on insights from these initial experiments, we decided to apply BSU with the H1 mixture model and normalization processing step to the core sample. In the pixel-wise spectral unmixing case, the prediction error for BSU is 1.865% and for FCLS is 3.691%. This result shows that our approach can generalize well into the rock sample used in this research (RQ 3.a).

In terms of prediction error, BSU generally produced better results compared to FCLS spectral unmixing. The difference was small in the computer-generated mixtures and but quite significant in the powder mixtures and rock samples. Additionally, BSU provided more detailed information in the results. With the current formulation, we were unable to obtain an optimal estimate of the uncertainty for the powder mixture samples, but we often much better result for the rock sample. We suspect this is due to the high muscovite content in the powder mixture which complicates the uncertainty related to the mixture model. Finally, BSU demands significantly higher computational resources. Although this may not be a serious problem with modern computers and more advance computation techniques, it is still orders of magnitude slower compared to FCLS. (RQ 3.b.)

This research highlights the potential of using Bayesian methods for spectral unmixing of core samples. Our approach shows promising results and we have identified several areas for improvement and practical insights related to spectral unmixing based on our findings. We hope that his research may be helpful to guide future research to improve reliability of spectral unmixing on rock samples by developing more refined MCMC and Hapke Model implementations.

# LIST OF REFERENCES


Al-Kharra'a, H. S., Wolf, K.-H. A. A., AlQuraishi, A. A., Mahmoud, M. A., Deshenenkov, I., AlDuhailan, M. A., Alarifi, S. A., AlQahtani, N. B., Kwak, H. T., & Zitha, P. L. J. (2023). Impact of clay mineralogy on the petrophysical properties of tight sandstones. *Geoenergy Science and Engineering*, *227*, 211883. https://doi.org/10.1016/j.geoen.2023.211883

Asadzadeh, S., & de Souza Filho, C. R. (2016). A review on spectral processing methods for geological remote sensing. *International Journal of Applied Earth Observation and Geoinformation*, *47*, 69–90. https://doi.org/10.1016/j.jag.2015.12.004

Aster, R. C., Borchers, B., & Thurber, C. H. (2013). Parameter Estimation and Inverse Problems. In *Parameter Estimation and Inverse Problems, Second Edition*. Elsevier. https://doi.org/10.1016/C2009-0-61134-X

Bakker, W. H. (2024). *wimhbakker/hyppy: HypPy3 (hyppy-v3)* (v. 3). Zenodo. https://doi.org/10.5281/zenodo.11204368

Bioucas-Dias, J. M., Plaza, A., Dobigeon, N., Parente, M., Du, Q., Gader, P., & Chanussot, J. (2012). Hyperspectral Unmixing Overview: Geometrical, Statistical, and Sparse Regression-Based Approaches. *IEEE Journal of Selected Topics in Applied Earth Observations and Remote Sensing*, *5*(2), 354–379. https://doi.org/10.1109/JSTARS.2012.2194696

Brooks, S., Gelman, A., Jones, G., & Meng, X.-L. (2011). Handbook of Markov Chain Monte Carlo. In *Handbook of Markov Chain Monte Carlo*. Chapman and Hall/CRC. https://doi.org/10.1201/b10905

Clark, R. N., King, T. V. V., Klejwa, M., Swayze, G. A., & Vergo, N. (1990). High spectral resolution reflectance spectroscopy of minerals. *Journal of Geophysical Research: Solid Earth*, *95*(B8), 12653–12680. https://doi.org/10.1029/JB095iB08p12653

Clark, R. N., & Roush, T. L. (1984). Reflectance spectroscopy: Quantitative analysis techniques for remote sensing applications. *Journal of Geophysical Research: Solid Earth*, *89*(B7), 6329–6340. https://doi.org/10.1029/JB089iB07p06329

Clark, R. N., Swayze, G. A., Livo, K. E., Kokaly, R. F., Sutley, S. J., Dalton, J. B., McDougal, R. R., & Gent, C. A. (2003). Imaging spectroscopy: Earth and planetary remote sensing with the USGS Tetracorder and expert systems. *Journal of Geophysical Research: Planets*, *108*(E12), 5131. https://doi.org/10.1029/2002JE001847

Cui, Y., Jones, S. J., Saville, C., Stricker, S., Wang, G., Tang, L., Fan, X., & Chen, J. (2017). The role played by carbonate cementation in controlling reservoir quality of the Triassic Skagerrak Formation, Norway. *Marine and Petroleum Geology*, *85*, 316–331. https://doi.org/10.1016/j.marpetgeo.2017.05.020

Dobigeon, N., Tourneret, J.-Y., & Chang, C.-I. (2008). Semi-Supervised Linear Spectral Unmixing Using a Hierarchical Bayesian Model for Hyperspectral Imagery. *IEEE Transactions on Signal Processing*, *56*(7), 2684–2695. https://doi.org/10.1109/TSP.2008.917851

Ducasse, E., Adeline, K., Briottet, X., Hohmann, A., Bourguignon, A., & Grandjean, G. (2020). Montmorillonite Estimation in Clay–Quartz–Calcite Samples from Laboratory SWIR Imaging Spectroscopy: A Comparative Study of Spectral Preprocessings and Unmixing Methods. *Remote Sensing*, *12*(11), 1723. https://doi.org/10.3390/rs12111723

Figliuzzi, B., Velasco-Forero, S., Bilodeau, M., & Angulo, J. (2016). A Bayesian Approach to Linear Unmixing in the Presence of Highly Mixed Spectra. In *Lecture Notes in Computer Science (including subseries Lecture Notes in Artificial Intelligence and Lecture Notes in Bioinformatics): Vol. 10016 LNCS* (pp. 263–274). Springer Verlag. https://doi.org/10.1007/978-3-319-48680-2_24

Freegarde, T. (2012). *Introduction to the Physics of Waves*. Cambridge University Press. https://doi.org/10.1017/CBO9781139048149

Gelman, A. (2006). Prior distributions for variance parameters in hierarchical models (comment on article by Browne and Draper). *Bayesian Analysis*, *1*(3), 515–533. https://doi.org/10.1214/06-BA117A

Gelman, A., Carlin, J. B., Stern, H. S., Dunson, D. B., Vehtari, A., & Rubin, D. B. (2013). *Bayesian Data Analysis*. Chapman and Hall/CRC. https://doi.org/10.1201/b16018

Girgin, S. (2021). *Using FOSS to develop and operate a geospatial computing platform*. Zenodo. https://doi.org/10.5281/zenodo.6025282

Gregory, P. (2005). Bayesian Logical Data Analysis for the Physical Sciences. In *Bayesian Logical Data Analysis for the Physical Sciences: A Comparative Approach with Mathematica Support*. Cambridge University Press. https://doi.org/10.1017/CBO9780511791277

Hapke, B. (1981). Bidirectional reflectance spectroscopy: 1. Theory. *Journal of Geophysical Research: Solid Earth*, *86*(B4), 3039–3054. https://doi.org/10.1029/JB086iB04p03039

Hapke, B. (2012). *Theory of Reflectance and Emittance Spectroscopy*. Cambridge University Press. https://doi.org/10.1017/CBO9781139025683

Harris, J. K., & M. Grindrod, P. (2018). Hapke mixture modeling applied to <scp>VNIR</scp> spectra of mafic mineral mixtures and shergottites: Implications for quantitative analysis of satellite data. *Meteoritics & Planetary Science*, *53*(6), 1179–1206. https://doi.org/10.1111/maps.13065

Hastings, W. K. (1970). Monte Carlo Sampling Methods Using Markov Chains and Their Applications. *Biometrika*, *57*(1), 97. https://doi.org/10.2307/2334940

Heinz, D., Chang, C.-I., & Althouse, M. L. G. (2003). Fully constrained least-squares based linear unmixing [hyperspectral image classification]. *IEEE 1999 International Geoscience and Remote Sensing Symposium. IGARSS'99 (Cat. No.99CH36293)*, *2*, 1401–1403. https://doi.org/10.1109/IGARSS.1999.774644

Heylen, R., Parente, M., & Gader, P. (2014). A Review of Nonlinear Hyperspectral Unmixing Methods. *IEEE Journal of Selected Topics in Applied Earth Observations and Remote Sensing*, *7*(6), 1844–1868. https://doi.org/10.1109/JSTARS.2014.2320576

Howari, F. M., Acbas, G., Nazzal, Y., & AlAydaroos, F. (2018). Hapke-based computational method to enable unmixing of hyperspectral data of common salts. *Chemistry Central Journal*, *12*(1), 90. https://doi.org/10.1186/s13065-018-0460-z

Hunt, G. R. (1977). Spectral Signatures of Particulate Minerals In The Visible And Near Infrared. *GEOPHYSICS*, *42*(3), 501–513. https://doi.org/10.1190/1.1440721

Keshava, N., & Mustard, J. F. (2002). Spectral unmixing. *IEEE Signal Processing Magazine*, *19*(1), 44–57. https://doi.org/10.1109/79.974727

Kokaly, R. F., Clark, R. N., Swayze, G. A., Livo, K. E., Hoefen, T. M., Pearson, N. C., Wise, R. A., Benzel, W., Lowers, H. A., Driscoll, R. L., & Klein, A. J. (2017). USGS Spectral Library Version 7. *Data Series*. https://doi.org/https://doi.org/10.3133/ds1035

Lapotre, M. G. A., Ehlmann, B. L., & Minson, S. E. (2017). A probabilistic approach to remote compositional analysis of planetary surfaces. *Journal of Geophysical Research: Planets*, *122*(5), 983–1009. https://doi.org/10.1002/2016JE005248

Laukamp, C., Rodger, A., LeGras, M., Lampinen, H., Lau, I. C., Pejcic, B., Stromberg, J., Francis, N., & Ramanaidou, E. (2021). Mineral Physicochemistry Underlying Feature-Based Extraction of Mineral Abundance and Composition from Shortwave, Mid and Thermal Infrared Reflectance Spectra. *Minerals*, *11*(4), 347. https://doi.org/10.3390/min11040347

Liu, D., Li, L., & Sun, Y. (2015). An improved radiative transfer model for estimating mineral abundance of immature and mature lunar soils. *Icarus*, *253*, 40–50. https://doi.org/10.1016/j.icarus.2015.02.013

Liu, W., Hecker, C., van Ruitenbeek, F. J. A., van Eijndthoven, W., & Cheng, Q. (2023). Identifying and Quantifying Carbonate Minerals in Quartz–Illite–Muscovite-Dominated Reservoir Rocks With SWIR and LWIR Spectroscopies. *IEEE Transactions on Geoscience and Remote Sensing*, *61*, 1–13. https://doi.org/10.1109/TGRS.2023.3298902

Lucey, P. G. (1998). Model near-infrared optical constants of olivine and pyroxene as a function of iron content. *Journal of Geophysical Research: Planets*, *103*(E1), 1703–1713. https://doi.org/10.1029/97JE03145

Metropolis, N., Rosenbluth, A. W., Rosenbluth, M. N., Teller, A. H., & Teller, E. (1953). Equation of State Calculations by Fast Computing Machines. *The Journal of Chemical Physics*, *21*(6), 1087–1092. https://doi.org/10.1063/1.1699114

Mindat. (2024). *Mindat.org - Mines, Minerals and More*. https://www.mindat.org/

Mustard, J. F., & Pieters, C. M. (1989). Photometric phase functions of common geologic minerals and applications to quantitative analysis of mineral mixture reflectance spectra. *Journal of Geophysical Research: Solid Earth*, *94*(B10), 13619–13634. https://doi.org/10.1029/JB094iB10p13619

Nash, D. B., & Conel, J. E. (1974). Spectral reflectance systematics for mixtures of powdered hypersthene, labradorite, and ilmenite. *Journal of Geophysical Research*, *79*(11), 1615–1621. https://doi.org/10.1029/JB079i011p01615

Ng, K. W., Tian, G., & Tang, M. (2011). *Dirichlet and Related Distributions*. Wiley. https://doi.org/10.1002/9781119995784

Pilorget, C., & Fernando, J. (2021). Quantifying the minerals abundances on planetary surfaces using VIS–NIR spectroscopy, what uncertainties should we expect? General results and application to the case of phyllosilicates and carbonates on Mars. *Icarus*, *365*, 114498. https://doi.org/10.1016/j.icarus.2021.114498

Pontual, S., Merry, N., & Gamson, P. (2008). *GMEX spectral analysis guides for mineral exploration*. https://scholar.google.com/scholar_lookup?title=G-MEXSpectral%20Analysis%20Guides%20for%20Mineral%20ExplorationPractical%20Applications%20Handbook&publication_year=2008&author=S.%20Pontual&author=N.%20Merry&author=P.%20Gamson

Rinnan, Åsmund, Berg, F. van den, & Engelsen, S. B. (2009). Review of the most common pre-processing techniques for near-infrared spectra. *TrAC Trends in Analytical Chemistry*, *28*(10), 1201–1222. https://doi.org/10.1016/j.trac.2009.07.007

Robert, C. P., & Casella, George. (2010). *Introducing Monte Carlo methods with R*. Springer.

Robertson, K. M., Milliken, R. E., & Li, S. (2016). Estimating mineral abundances of clay and gypsum mixtures using radiative transfer models applied to visible-near infrared reflectance spectra. *Icarus*, *277*, 171–186. https://doi.org/10.1016/J.ICARUS.2016.04.034

SGS. (2013). *QEMSCAN OPERATIONAL MODES*. www.sgs.com/mining

Sklute, E. C., Glotch, T. D., Piatek, J. L., Woerner, W. R., Martone, A. A., & Kraner, M. L. (2015). Optical constants of synthetic potassium, sodium, and hydronium jarosite. *American Mineralogist*, *100*(5–6), 1110–1122. https://doi.org/10.2138/am-2015-4824

Therein, C. (2018). *Endmembers Extraction Algorithms (EEA) — pysptools 0.15.0 documentation*. https://pysptools.sourceforge.io/eea.html

Van Der Meer, F. (2000). Spectral curve shape matching with a continuum removed CCSM algorithm. *International Journal of Remote Sensing*, *21*(16), 3179–3185. https://doi.org/10.1080/01431160050145063

Winter, M. E. (1999). <title>N-FINDR: an algorithm for fast autonomous spectral end-member determination in hyperspectral data</title> In M. R. Descour & S. S. Shen (Eds.), *SPIE* (Vol. 3753, pp. 266–275). SPIE. https://doi.org/10.1117/12.366289

Zhang, J., Rivard, B., & Sánchez-Azofeifa, A. (2005). Spectral unmixing of normalized reflectance data for the deconvolution of lichen and rock mixtures. *Remote Sensing of Environment*, *95*(1), 57–66. https://doi.org/10.1016/j.rse.2004.11.019

Zhang, X., & Curtis, A. (2021). Bayesian Geophysical Inversion Using Invertible Neural Networks. *Journal of Geophysical Research: Solid Earth*, *126*(7), e2021JB022320. https://doi.org/10.1029/2021JB022320

Zhao, H., & Zhao, X. (2019). Nonlinear unmixing of minerals based on the log and continuum removal model. *European Journal of Remote Sensing*, *52*(1), 277–293. https://doi.org/10.1080/22797254.2019.1601999

# APPENDIX

## Appendix 1. Measurement Results

*1.a. Spectra measurement variance of every sample*

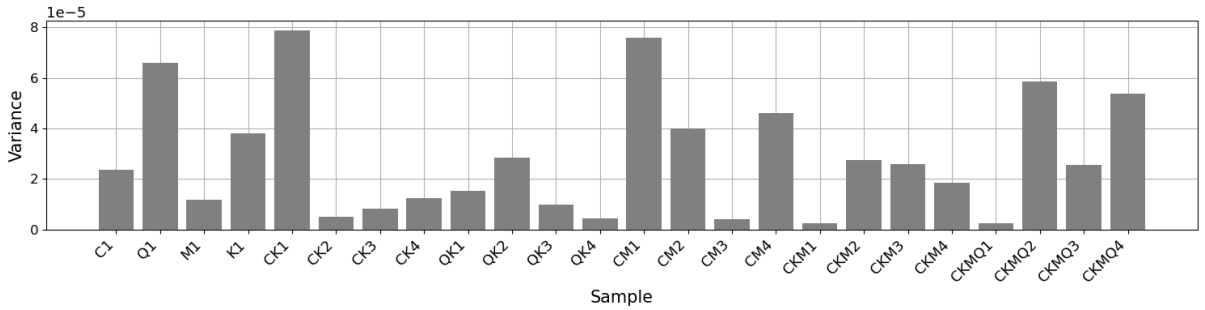


*1.b. Spectra measurement of CK sample series*

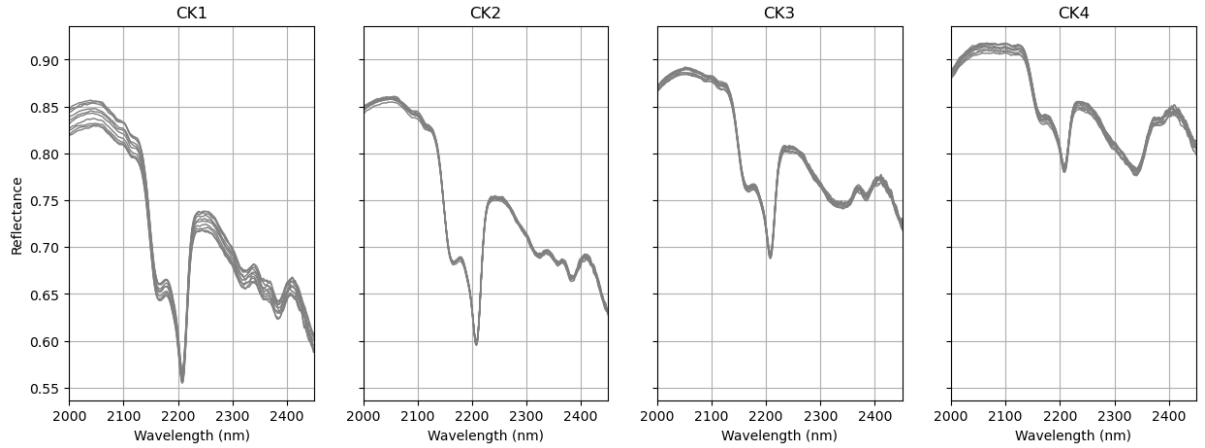


*1.c. Spectra measurement of QK sample series*

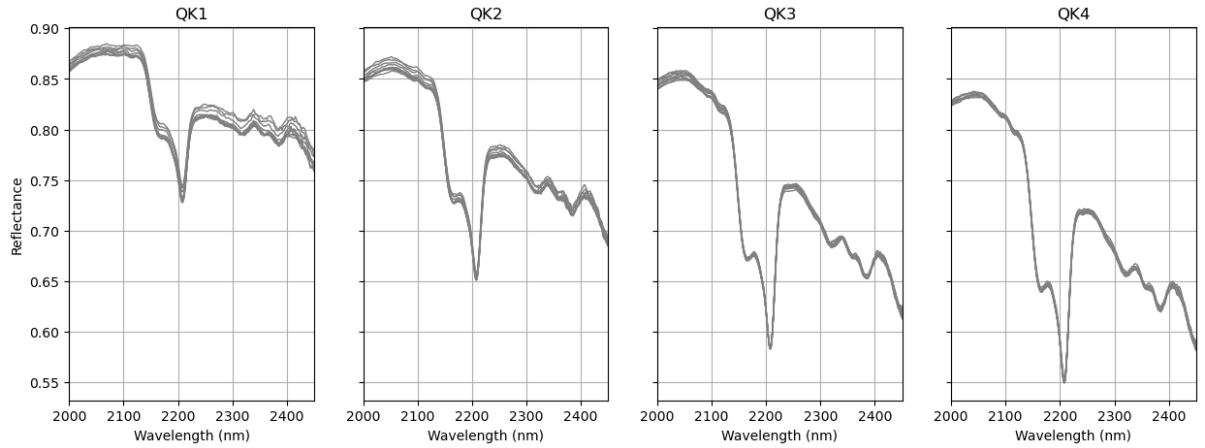

*1.d. Spectra measurement of CM sample series*

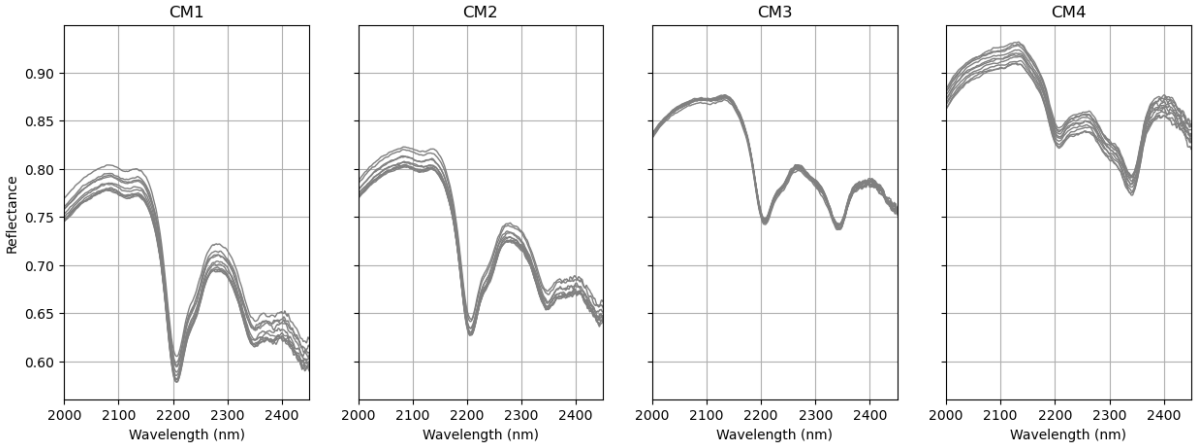


*1.e. Spectra measurement of CKM sample series*

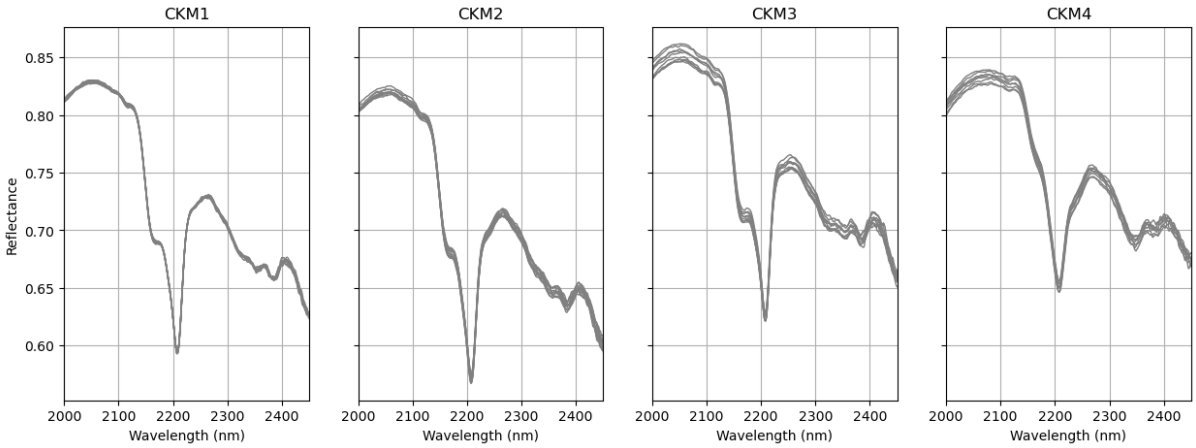


*1.f. Spectra measurement of CKMQ sample series*

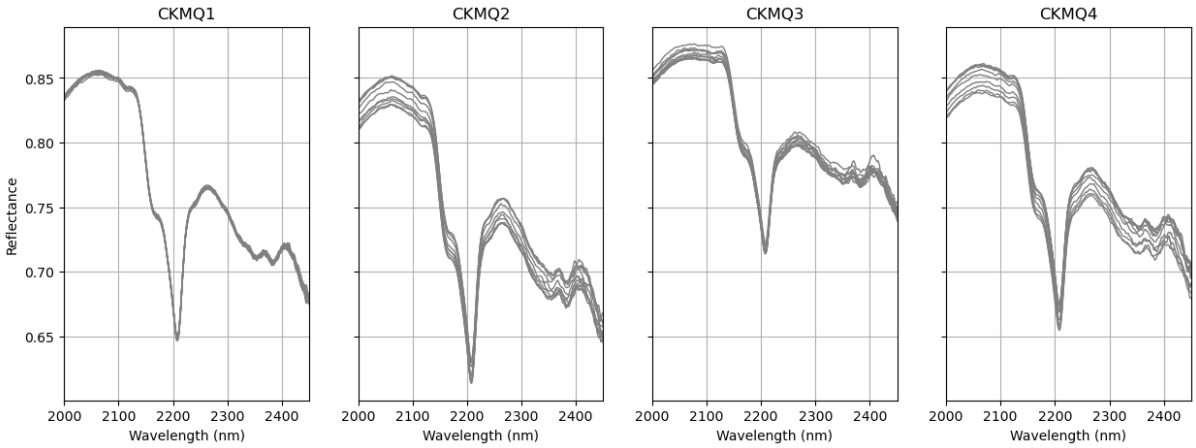

*1.g. Spectra measurement of endmembers*

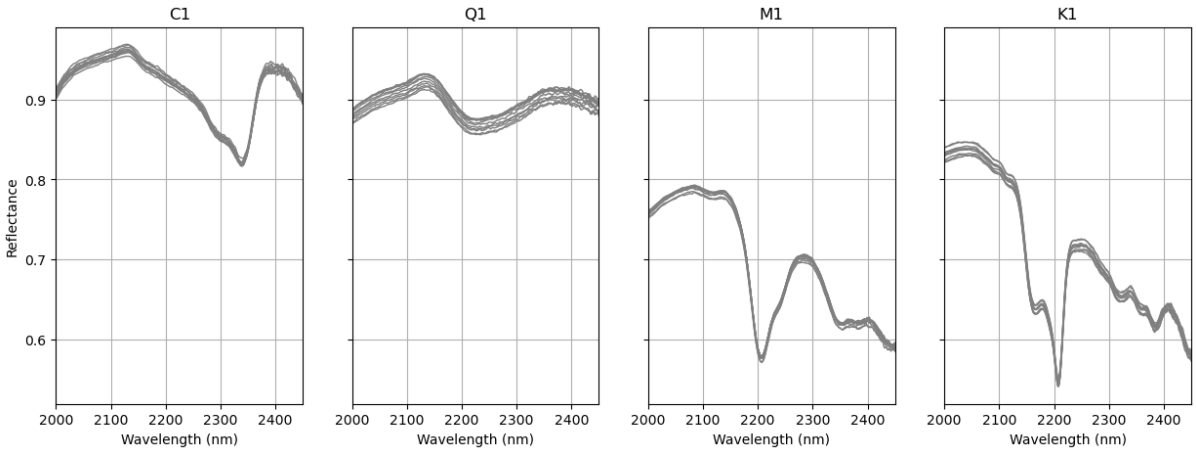


## APPENDIX 2. Spectral Reconstruction

*2.a. LMM Spectral Reconstruction*

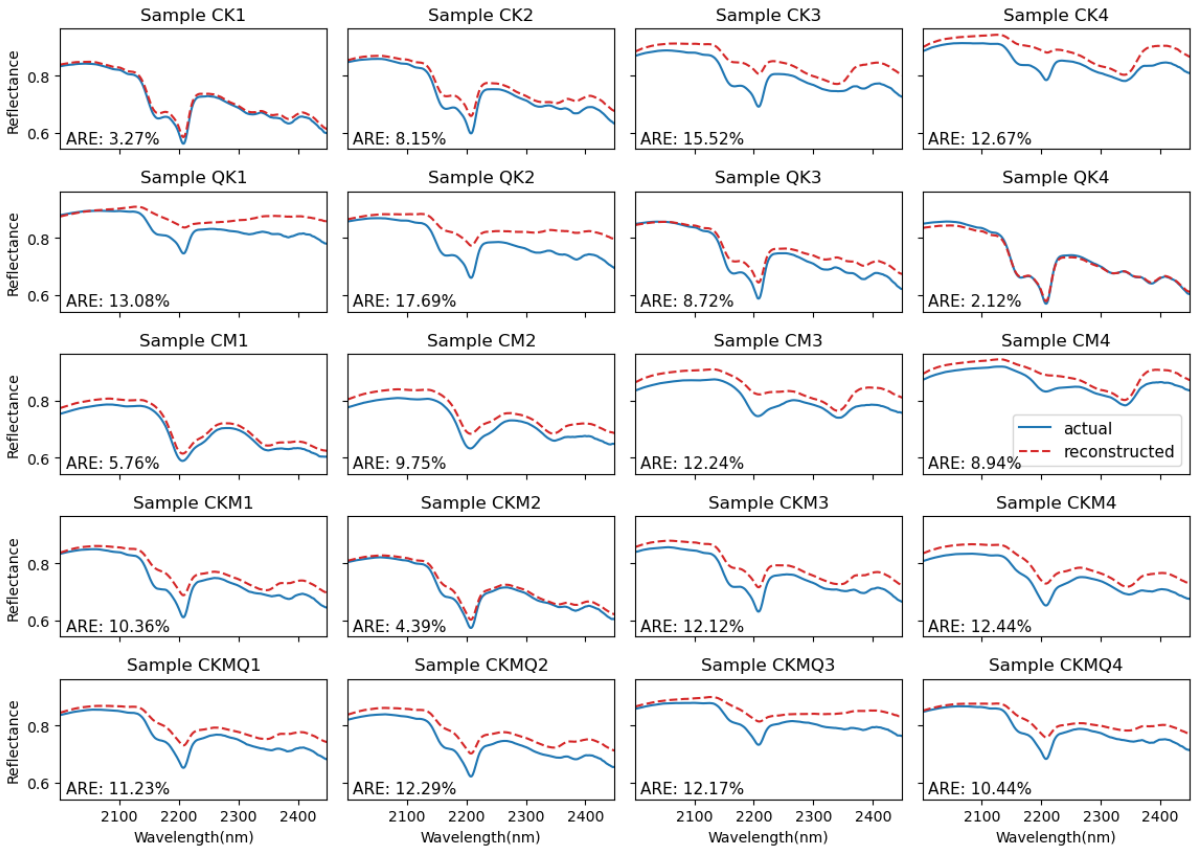

*2.b. H1 Spectral Reconstruction*

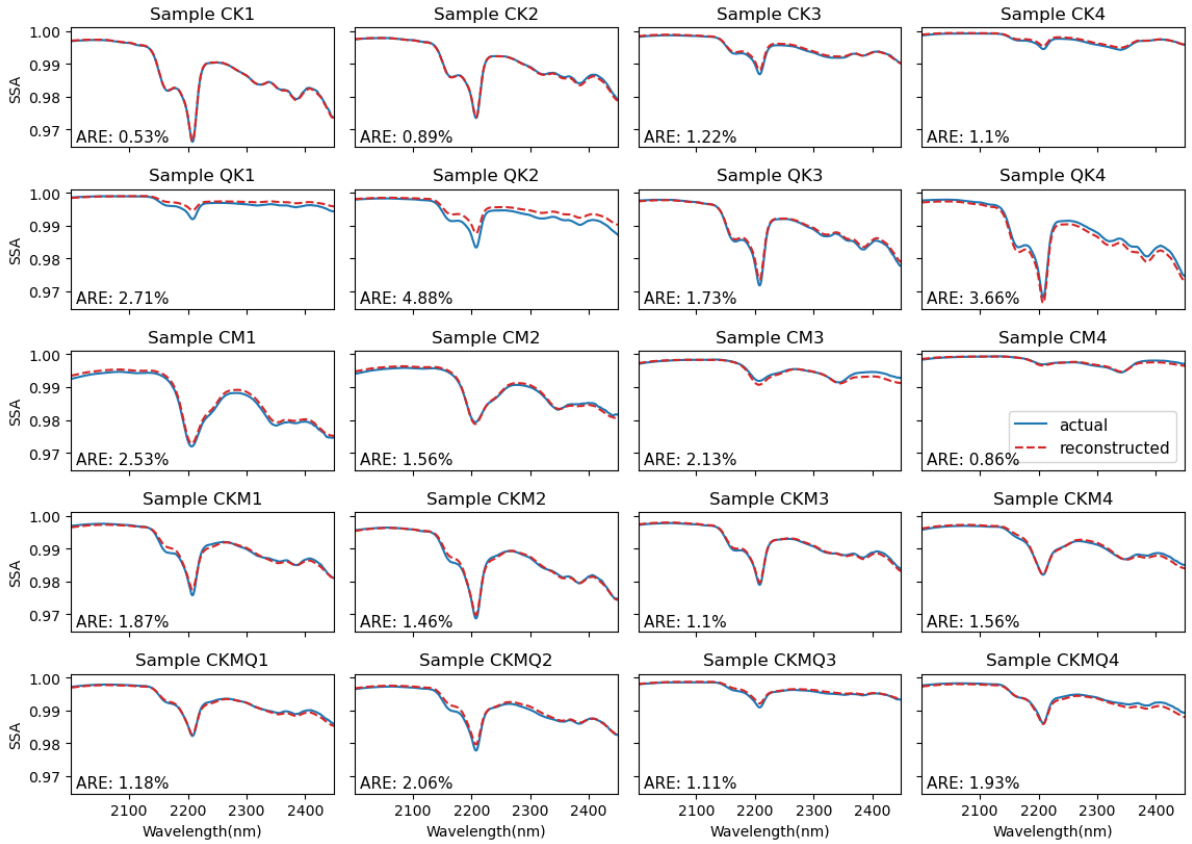


*2.c. H2 Spectral Reconstruction*

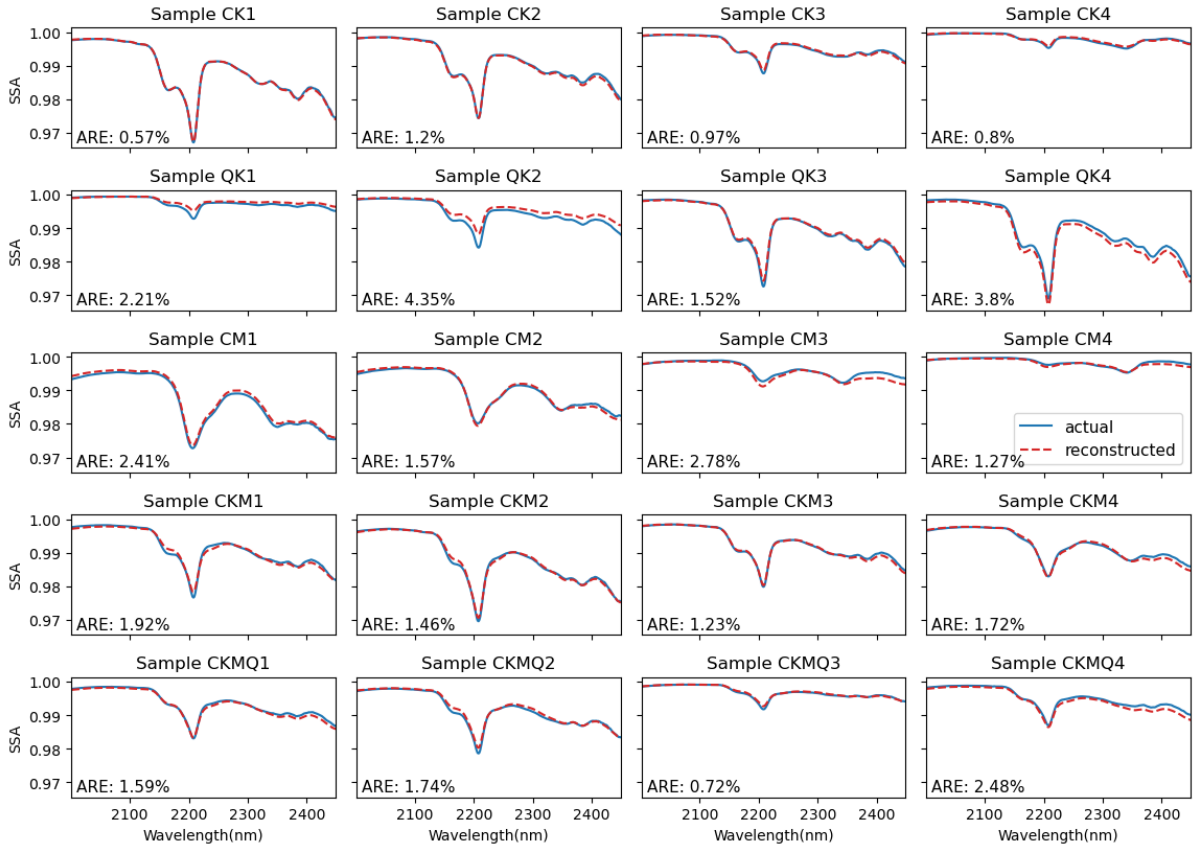

*2.d. Spectral Reconstruction with hull removal, first derivative, and normalization*

| Sample | LMM | | | | H1 | | | | H2 | | | |
|---|---|---|---|---|---|---|---|---|---|---|---|---|
| | No Processing | Normalize | Hull Removal | First Derivative | No Processing | Normalize | Hull Removal | First Derivative | No Processing | Normalize | Hull Removal | First Derivative |
| **CK1** | 3.27 | 1.20 | 1.70 | 1.50 | 0.53 | 0.58 | 0.59 | 0.92 | 0.57 | 0.59 | 0.33 | 0.93 |
| **CK2** | 8.15 | 3.73 | 4.70 | 3.11 | 0.89 | 0.81 | 0.86 | 0.63 | 1.20 | 0.86 | 0.31 | 0.68 |
| **CK3** | 15.52 | 6.81 | 8.52 | 5.44 | 1.22 | 0.91 | 1.01 | 0.48 | 0.97 | 1.01 | 1.70 | 0.52 |
| **CK4** | 12.67 | 5.47 | 7.04 | 4.65 | 1.10 | 0.66 | 0.78 | 0.32 | 0.80 | 0.78 | 1.42 | 0.37 |
| **QK1** | 13.08 | 7.74 | 7.21 | 5.35 | 2.71 | 1.85 | 1.62 | 0.99 | 2.21 | 1.62 | 1.82 | 0.96 |
| **QK2** | 17.69 | 8.94 | 8.12 | 5.73 | 4.88 | 2.82 | 2.70 | 1.51 | 4.35 | 2.70 | 2.91 | 1.52 |
| **QK3** | 8.72 | 5.22 | 4.44 | 3.19 | 1.73 | 1.34 | 1.31 | 0.99 | 1.52 | 1.31 | 1.37 | 1.02 |
| **QK4** | 2.12 | 1.46 | 1.37 | 1.52 | 3.66 | 1.38 | 1.46 | 0.81 | 3.80 | 1.46 | 1.14 | 0.85 |
| **CM1** | 5.76 | 0.70 | 1.86 | 1.09 | 2.53 | 0.49 | 0.55 | 0.89 | 2.41 | 0.55 | 0.41 | 0.92 |
| **CM2** | 9.75 | 1.95 | 4.15 | 1.79 | 1.56 | 1.63 | 1.65 | 0.81 | 1.57 | 1.65 | 1.07 | 0.83 |
| **CM3** | 12.24 | 3.59 | 5.59 | 2.92 | 2.13 | 1.93 | 2.09 | 0.54 | 2.78 | 2.09 | 2.03 | 0.63 |
| **CM4** | 8.94 | 2.65 | 3.83 | 2.35 | 0.86 | 0.91 | 1.09 | 0.29 | 1.27 | 1.09 | 1.43 | 0.40 |
| **CKM1** | 10.36 | 5.53 | 6.69 | 4.29 | 1.87 | 1.98 | 1.95 | 1.52 | 1.92 | 1.95 | 2.22 | 1.53 |
| **CKM2** | 4.39 | 2.51 | 3.46 | 2.24 | 1.46 | 1.55 | 1.54 | 1.28 | 1.46 | 1.54 | 1.69 | 1.29 |
| **CKM3** | 12.12 | 4.75 | 6.25 | 3.94 | 1.10 | 1.19 | 1.23 | 0.62 | 1.23 | 1.23 | 0.99 | 0.64 |
| **CKM4** | 12.44 | 3.58 | 5.54 | 2.79 | 1.56 | 1.71 | 1.76 | 0.66 | 1.72 | 1.76 | 1.09 | 0.70 |
| **CKMQ1** | 11.23 | 5.12 | 5.56 | 3.74 | 1.18 | 1.07 | 1.12 | 0.75 | 1.59 | 1.12 | 0.91 | 0.78 |
| **CKMQ2** | 12.29 | 4.67 | 5.64 | 3.50 | 2.06 | 1.46 | 1.44 | 1.02 | 1.74 | 1.44 | 1.53 | 1.04 |
| **CKMQ3** | 12.17 | 5.72 | 5.52 | 4.02 | 1.11 | 0.77 | 0.67 | 0.58 | 0.72 | 0.67 | 1.02 | 0.59 |
| **CKMQ4** | 10.44 | 5.06 | 5.39 | 3.81 | 1.93 | 1.27 | 1.38 | 0.55 | 2.48 | 1.38 | 0.76 | 0.59 |
| **Average** | 10.17 | 4.32 | 5.13 | 3.35 | 1.80 | 1.32 | 1.34 | 0.81 | 1.81 | 1.34 | 1.31 | 0.84 |

# Appendix 3. Powder Mixture Unmixing

*3.a. FCLS Result with H1 mixture model*

| Sample | Abundance | | | |
|---|---|---|---|---|
| | Calcite | Quartz | Muscovite | Kaolinite |
| **CK1** | 0.053 | 0.053 | 0.047 | 0.847 |
| **CK2** | 0.172 | 0.140 | 0.037 | 0.650 |
| **CK3** | 0.578 | 0.095 | 0.046 | 0.281 |
| **CK4** | 0.755 | 0.116 | 0.052 | 0.077 |
| **QK1** | 0.127 | 0.708 | 0.051 | 0.114 |
| **QK2** | 0.053 | 0.539 | 0.035 | 0.372 |
| **QK3** | 0.125 | 0.140 | 0.038 | 0.697 |
| **QK4** | 0.087 | 0.089 | 0.035 | 0.789 |
| **CM1** | 0.034 | 0.034 | 0.881 | 0.051 |
| **CM2** | 0.183 | 0.128 | 0.642 | 0.046 |
| **CM3** | 0.552 | 0.190 | 0.150 | 0.109 |
| **CM4** | 0.788 | 0.122 | 0.049 | 0.040 |
| **CKM1** | 0.177 | 0.172 | 0.176 | 0.475 |
| **CKM2** | 0.054 | 0.054 | 0.323 | 0.568 |
| **CKM3** | 0.230 | 0.212 | 0.122 | 0.435 |
| **CKM4** | 0.246 | 0.211 | 0.361 | 0.182 |
| **CKMQ1** | 0.264 | 0.256 | 0.182 | 0.299 |
| **CKMQ2** | 0.192 | 0.188 | 0.226 | 0.393 |
| **CKMQ3** | 0.229 | 0.550 | 0.106 | 0.115 |
| **CKMQ4** | 0.256 | 0.384 | 0.158 | 0.203 |

*3.b. Hull Removal BSU Result with H1 mixture model*

| Sample | Calcite | | | Quartz | | | Muscovite | | | Kaolinite | | | Prediction |
|---|---|---|---|---|---|---|---|---|---|---|---|---|---|
| | *Actual* | *P50* | *P95-P5* | *Actual* | *P50* | *P95-P5* | *Actual* | *P50* | *P95-P5* | *Actual* | *P50* | *P95-P5* | **Error** |
| *CK1* | 0.10 | 0.05 | 0.09 | 0.00 | 0.04 | 0.09 | 0.00 | 0.01 | 0.04 | 0.90 | 0.89 | 0.05 | **3.33** |
| *CK2* | 0.30 | 0.21 | 0.19 | 0.00 | 0.09 | 0.19 | 0.00 | 0.01 | 0.03 | 0.70 | 0.69 | 0.05 | **6.30** |
| *CK3* | 0.69 | 0.62 | 0.11 | 0.00 | 0.03 | 0.11 | 0.00 | 0.02 | 0.05 | 0.31 | 0.32 | 0.05 | **4.04** |
| *CK4* | 0.89 | 0.83 | 0.09 | 0.00 | 0.02 | 0.08 | 0.00 | 0.03 | 0.05 | 0.11 | 0.12 | 0.05 | **3.25** |
| *QK1* | 0.00 | 0.05 | 0.15 | 0.90 | 0.77 | 0.16 | 0.00 | 0.01 | 0.04 | 0.10 | 0.17 | 0.05 | **7.56** |
| *QK2* | 0.00 | 0.03 | 0.10 | 0.70 | 0.56 | 0.11 | 0.00 | 0.01 | 0.04 | 0.30 | 0.40 | 0.05 | **8.54** |
| *QK3* | 0.00 | 0.03 | 0.09 | 0.30 | 0.23 | 0.11 | 0.00 | 0.01 | 0.03 | 0.70 | 0.73 | 0.04 | **4.35** |
| *QK4* | 0.00 | 0.04 | 0.11 | 0.10 | 0.10 | 0.12 | 0.00 | 0.01 | 0.04 | 0.90 | 0.84 | 0.05 | **3.55** |
| *CM1* | 0.11 | 0.06 | 0.10 | 0.00 | 0.05 | 0.10 | 0.89 | 0.89 | 0.04 | 0.00 | 0.00 | 0.00 | **3.79** |
| *CM2* | 0.31 | 0.22 | 0.26 | 0.00 | 0.15 | 0.27 | 0.69 | 0.61 | 0.05 | 0.00 | 0.01 | 0.04 | **9.81** |
| *CM3* | 0.71 | 0.73 | 0.13 | 0.00 | 0.03 | 0.12 | 0.29 | 0.22 | 0.05 | 0.00 | 0.01 | 0.03 | **3.93** |
| *CM4* | 0.90 | 0.89 | 0.09 | 0.00 | 0.02 | 0.08 | 0.10 | 0.07 | 0.05 | 0.00 | 0.01 | 0.03 | **1.88** |
| *CKM1* | 0.35 | 0.18 | 0.26 | 0.00 | 0.18 | 0.27 | 0.29 | 0.15 | 0.07 | 0.36 | 0.50 | 0.06 | **15.70** |
| *CKM2* | 0.11 | 0.04 | 0.11 | 0.00 | 0.10 | 0.12 | 0.42 | 0.30 | 0.07 | 0.46 | 0.56 | 0.06 | **10.27** |
| *CKM3* | 0.44 | 0.37 | 0.18 | 0.00 | 0.08 | 0.18 | 0.11 | 0.07 | 0.07 | 0.45 | 0.48 | 0.06 | **5.88** |
| *CKM4* | 0.45 | 0.34 | 0.25 | 0.00 | 0.17 | 0.26 | 0.43 | 0.33 | 0.07 | 0.12 | 0.16 | 0.06 | **11.61** |
| *CKMQ1* | 0.25 | 0.15 | 0.25 | 0.26 | 0.39 | 0.25 | 0.24 | 0.16 | 0.07 | 0.26 | 0.30 | 0.06 | **9.44** |
| *CKMQ2* | 0.30 | 0.15 | 0.25 | 0.11 | 0.27 | 0.26 | 0.28 | 0.19 | 0.07 | 0.31 | 0.39 | 0.06 | **12.63** |
| *CKMQ3* | 0.10 | 0.09 | 0.19 | 0.70 | 0.69 | 0.20 | 0.09 | 0.07 | 0.07 | 0.11 | 0.14 | 0.06 | **2.28** |
| *CKMQ4* | 0.20 | 0.11 | 0.21 | 0.40 | 0.53 | 0.22 | 0.19 | 0.12 | 0.07 | 0.20 | 0.24 | 0.06 | **8.79** |
| ***Average*** | **0.31** | **0.26** | **0.16** | **0.17** | **0.23** | **0.16** | **0.20** | **0.17** | **0.05** | **0.31** | **0.35** | **0.05** | **6.85** |

*3.c. First Derivative BSU Result with H1 mixture model*

| Sample | Calcite | | | Quartz | | | Muscovite | | | Kaolinite | | | Prediction |
|---|---|---|---|---|---|---|---|---|---|---|---|---|---|
| | *Actual* | *P50* | *P95-P5* | *Actual* | *P50* | *P95-P5* | *Actual* | *P50* | *P95-P5* | *Actual* | *P50* | *P95-P5* | **Error** |
| *CK1* | 0.10 | 0.04 | 0.09 | 0.00 | 0.04 | 0.10 | 0.00 | 0.03 | 0.08 | 0.90 | 0.88 | 0.08 | **4.00** |
| *CK2* | 0.30 | 0.15 | 0.25 | 0.00 | 0.11 | 0.24 | 0.00 | 0.03 | 0.10 | 0.70 | 0.69 | 0.09 | **9.33** |
| *CK3* | 0.69 | 0.45 | 0.45 | 0.00 | 0.19 | 0.44 | 0.00 | 0.04 | 0.10 | 0.31 | 0.32 | 0.09 | **15.39** |
| *CK4* | 0.89 | 0.67 | 0.50 | 0.00 | 0.18 | 0.49 | 0.00 | 0.04 | 0.11 | 0.11 | 0.11 | 0.09 | **14.00** |
| *QK1* | 0.00 | 0.23 | 0.55 | 0.90 | 0.55 | 0.56 | 0.00 | 0.04 | 0.10 | 0.10 | 0.17 | 0.09 | **20.98** |
| *QK2* | 0.00 | 0.17 | 0.42 | 0.70 | 0.37 | 0.43 | 0.00 | 0.04 | 0.10 | 0.30 | 0.41 | 0.09 | **19.22** |
| *QK3* | 0.00 | 0.10 | 0.21 | 0.30 | 0.11 | 0.21 | 0.00 | 0.03 | 0.10 | 0.70 | 0.74 | 0.09 | **11.24** |
| *QK4* | 0.00 | 0.05 | 0.11 | 0.10 | 0.05 | 0.11 | 0.00 | 0.03 | 0.09 | 0.90 | 0.85 | 0.09 | **4.33** |
| *CM1* | 0.11 | 0.06 | 0.14 | 0.00 | 0.06 | 0.14 | 0.89 | 0.85 | 0.15 | 0.00 | 0.02 | 0.06 | **4.29** |
| *CM2* | 0.31 | 0.25 | 0.34 | 0.00 | 0.12 | 0.32 | 0.69 | 0.61 | 0.15 | 0.00 | 0.02 | 0.05 | **7.80** |
| *CM3* | 0.71 | 0.62 | 0.50 | 0.00 | 0.15 | 0.48 | 0.29 | 0.21 | 0.15 | 0.00 | 0.02 | 0.06 | **9.73** |
| *CM4* | 0.90 | 0.76 | 0.52 | 0.00 | 0.16 | 0.51 | 0.10 | 0.05 | 0.11 | 0.00 | 0.02 | 0.05 | **11.28** |
| *CKM1* | 0.35 | 0.19 | 0.30 | 0.00 | 0.13 | 0.29 | 0.29 | 0.17 | 0.17 | 0.36 | 0.50 | 0.10 | **14.12** |
| *CKM2* | 0.11 | 0.06 | 0.14 | 0.00 | 0.06 | 0.13 | 0.42 | 0.31 | 0.17 | 0.46 | 0.57 | 0.10 | **8.59** |
| *CKM3* | 0.44 | 0.26 | 0.38 | 0.00 | 0.18 | 0.37 | 0.11 | 0.08 | 0.15 | 0.45 | 0.48 | 0.10 | **12.91** |
| *CKM4* | 0.45 | 0.33 | 0.41 | 0.00 | 0.16 | 0.40 | 0.43 | 0.35 | 0.17 | 0.12 | 0.16 | 0.10 | **10.97** |
| *CKMQ1* | 0.25 | 0.27 | 0.44 | 0.26 | 0.23 | 0.45 | 0.24 | 0.18 | 0.18 | 0.26 | 0.31 | 0.10 | **4.50** |
| *CKMQ2* | 0.30 | 0.23 | 0.34 | 0.11 | 0.16 | 0.33 | 0.28 | 0.22 | 0.17 | 0.31 | 0.40 | 0.10 | **7.05** |
| *CKMQ3* | 0.10 | 0.25 | 0.62 | 0.70 | 0.51 | 0.62 | 0.09 | 0.09 | 0.15 | 0.11 | 0.15 | 0.10 | **12.32** |
| *CKMQ4* | 0.20 | 0.30 | 0.51 | 0.40 | 0.32 | 0.52 | 0.19 | 0.14 | 0.18 | 0.20 | 0.24 | 0.10 | **7.19** |
| ***Average*** | **0.31** | **0.27** | **0.36** | **0.17** | **0.19** | **0.36** | **0.20** | **0.18** | **0.13** | **0.31** | **0.35** | **0.09** | **10.46** |

*3d. Normalization BSU Result with H1 mixture model*

| Sample | Calcite | | | Quartz | | | Muscovite | | | Kaolinite | | | Prediction |
|---|---|---|---|---|---|---|---|---|---|---|---|---|---|
| | *Actual* | *P50* | *P95-P5* | *Actual* | *P50* | *P95-P5* | *Actual* | *P50* | *P95-P5* | *Actual* | *P50* | *P95-P5* | **Error** |
| *CK1* | 0.10 | 0.06 | 0.10 | 0.00 | 0.05 | 0.10 | 0.00 | 0.01 | 0.04 | 0.90 | 0.88 | 0.05 | **3.60** |
| *CK2* | 0.30 | 0.21 | 0.23 | 0.00 | 0.10 | 0.22 | 0.00 | 0.01 | 0.04 | 0.70 | 0.68 | 0.05 | **7.14** |
| *CK3* | 0.69 | 0.60 | 0.22 | 0.00 | 0.08 | 0.21 | 0.00 | 0.01 | 0.04 | 0.31 | 0.30 | 0.05 | **5.96** |
| *CK4* | 0.89 | 0.83 | 0.17 | 0.00 | 0.05 | 0.16 | 0.00 | 0.02 | 0.04 | 0.11 | 0.10 | 0.05 | **4.02** |
| *QK1* | 0.00 | 0.06 | 0.18 | 0.90 | 0.77 | 0.18 | 0.00 | 0.01 | 0.04 | 0.10 | 0.16 | 0.05 | **7.65** |
| *QK2* | 0.00 | 0.05 | 0.17 | 0.70 | 0.54 | 0.17 | 0.00 | 0.01 | 0.04 | 0.30 | 0.39 | 0.05 | **9.42** |
| *QK3* | 0.00 | 0.06 | 0.18 | 0.30 | 0.19 | 0.18 | 0.00 | 0.02 | 0.04 | 0.70 | 0.73 | 0.05 | **6.74** |
| *QK4* | 0.00 | 0.05 | 0.13 | 0.10 | 0.10 | 0.13 | 0.00 | 0.01 | 0.04 | 0.90 | 0.84 | 0.05 | **4.05** |
| *CM1* | 0.11 | 0.07 | 0.10 | 0.00 | 0.04 | 0.09 | 0.89 | 0.88 | 0.05 | 0.00 | 0.01 | 0.04 | **3.02** |
| *CM2* | 0.31 | 0.32 | 0.15 | 0.00 | 0.04 | 0.14 | 0.69 | 0.62 | 0.05 | 0.00 | 0.01 | 0.04 | **4.14** |
| *CM3* | 0.71 | 0.73 | 0.16 | 0.00 | 0.05 | 0.15 | 0.29 | 0.21 | 0.05 | 0.00 | 0.01 | 0.04 | **4.85** |
| *CM4* | 0.90 | 0.89 | 0.14 | 0.00 | 0.04 | 0.14 | 0.10 | 0.06 | 0.05 | 0.00 | 0.01 | 0.04 | **3.10** |
| *CKM1* | 0.35 | 0.26 | 0.25 | 0.00 | 0.09 | 0.25 | 0.29 | 0.15 | 0.08 | 0.36 | 0.49 | 0.07 | **11.66** |
| *CKM2* | 0.11 | 0.12 | 0.04 | 0.00 | 0.00 | 0.00 | 0.42 | 0.31 | 0.07 | 0.46 | 0.57 | 0.07 | **7.61** |
| *CKM3* | 0.44 | 0.37 | 0.23 | 0.00 | 0.10 | 0.23 | 0.11 | 0.06 | 0.07 | 0.45 | 0.47 | 0.07 | **6.73** |
| *CKM4* | 0.45 | 0.45 | 0.18 | 0.00 | 0.04 | 0.17 | 0.43 | 0.34 | 0.08 | 0.12 | 0.16 | 0.07 | **5.27** |
| *CKMQ1* | 0.25 | 0.26 | 0.34 | 0.26 | 0.26 | 0.34 | 0.24 | 0.17 | 0.08 | 0.26 | 0.30 | 0.07 | **4.07** |
| *CKMQ2* | 0.30 | 0.31 | 0.26 | 0.11 | 0.09 | 0.25 | 0.28 | 0.20 | 0.08 | 0.31 | 0.39 | 0.07 | **5.84** |
| *CKMQ3* | 0.10 | 0.13 | 0.26 | 0.70 | 0.68 | 0.26 | 0.09 | 0.00 | 0.00 | 0.11 | 0.20 | 0.04 | **6.83** |
| *CKMQ4* | 0.20 | 0.19 | 0.31 | 0.40 | 0.45 | 0.31 | 0.19 | 0.12 | 0.08 | 0.20 | 0.23 | 0.07 | **4.48** |
| ***Average*** | **0.31** | **0.30** | **0.19** | **0.17** | **0.19** | **0.18** | **0.20** | **0.16** | **0.05** | **0.31** | **0.35** | **0.05** | **5.81** |